IS-T-811

PRECIPITATION KINETICS OF A CONTINUOUS PRECIPITATOR, WITH APPLICATION TO THE PRECIPITATION OF AMMONIUM POLYURANATE

Richard Conrad Hoyt

MASTER

Ph.D. Thesis Submitted to Iowa State University

Ames Laboratory, DOE
Iowa State University
Ames, Iowa 50011

Date Transmitted: April 1978

PREPARED FOR THE U.S. DEPARTMENT OF ENERGY
UNDER CONTRACT NO. W-7405-eng-82

DISCLAIMER

NOTICE

Available from: National Technical Information Service
U. S. Department of Commerce
P.O. Box 1553
Springfield, VA 22161

Price: Microfiche $3.00
Paper Copy ~~$6.75~~ $7.50

Precipitation kinetics of a continuous precipitator, with application to the precipitation of ammonium polyuranate

by

Richard Conrad Hoyt

An Abstract of

A Dissertation Submitted to the

Graduate Faculty in Partial Fulfillment of

The Requirements for the Degree of

DOCTOR OF PHILOSOPHY

Approved:

_____

In Charge of Major Work

_____

For the Major Department

_____

For the Graduate College

Iowa State University
Ames, Iowa

1978

Precipitation kinetics of a continuous precipitator, with application to the precipitation of ammonium polyuranate

Richard Conrad Hoyt

Under the supervision of Lawrence E. Burkhart
From the Department of Chemical Engineering and Nuclear Engineering
Iowa State University

A mathematical model describing the kinetics of continuous precipitation has been developed. This model accounts for crystal nucleation, crystal growth, primary coagulation, and secondary coagulation, with the coagulation processes being represented with average nucleation rates and effective growth rates. The kinetic model includes emperical relationships for the nucleation rates such that the population density distributions, average particle sizes, dominant particle sizes, and suspension density fractions of the crystallites, primary agglomerates, and secondary agglomerates leaving the continuous precipitator can be determined.

This kinetic model has been successfully applied to the continuous precipitation of ammonium polyuranate, which has been found to consist of three types of particles; (1) elementary crystals, (2) clusters or primary coagulated particles, and (3) agglomerates or secondary coagulated particles. The ammonium polyuranate crystallites have been shown to be thin, submicron, hexagonal platelets, the size of which depends upon the precipitation conditions. The clusters had an upper size limit of about 7 μm in diameter and contained numerous small voids (<.3 μm) due to

the packing of the crystallites. The agglomerates had an upper size limit of about 40 μm in diameter and contained large voids (~1 μm) which resulted from loose packing of both clusters and crystallites.

The precipitation conditions have been shown to affect the nucleation rates, growth rates, and structures of the primary and secondary coagulated particles. The kinetic parameters governing the particle size and structure of the precipitate have been shown to be dependent upon the ammonium to uranium reacting feed mole ratio rather than the precipitation pH.

The results of this work have shown that the particle size distribution and particle structure of the ammonium polyuranate precipitate can be controlled through proper regulation of the precipitation conditions. The ratio of clusters to agglomerates can be best controlled through the uranium concnetration, and the cohesiveness or internal bonding strength of the particles can be controlled with the ammonium to uranium reacting feed mole ratio. These two conditions, in conjunction with the residence time, will determine the nucleation rates, growth rates, and size distributions of the particles leaving the continuous precipitator. With proper control of these physical particle characteristics, the use of pore formers, ball-milling, and powder blending can probably be eliminated from the nuclear fuel fabrication process. This would substantially reduce the cost of the fuel fabrication process and therefore decrease the cost of the overall nuclear fuel cycle.

Precipitation kinetics of a continuous precipitator, with application to the precipitation of ammonium polyuranate

by

Richard Conrad Hoyt

A Dissertation Submitted to the
Graduate Faculty in Partial Fulfillment of
The Requirements for the Degree of
DOCTOR OF PHILOSOPHY

Department: Chemical Engineering and Nuclear Engineering
Major: Nuclear Engineering

Approved:

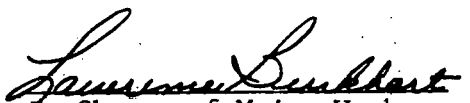
In Charge of Major Work

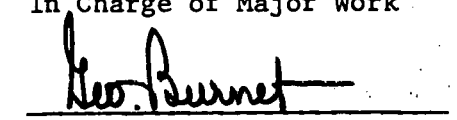
For the Major Department

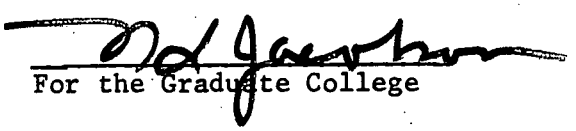
For the Graduate College

Iowa State University
Ames, Iowa

1978

TABLE OF CONTENTS

NOMENCLATURE[1]

A	surface area per unit volume of suspension, L^2/L^3
A'	surface area, L^2
B^o	nucleation rate per unit volume of suspension, $\#/(L \cdot L^3)$
$\overline{B}^o$	average nucleation rate per unit volume of suspension, $\#/(L \cdot L^3)$
C	solute concentration, M/L^3
C_e	solute equilibrium concentration, M/L^3
C_s	solute saturation concentration, M/L^3
D	diffusion coefficient, L/t
G	growth rate, L/t
G_a	average agglomerate growth rate resulting from cluster coagulation, L/t
G_a'	average agglomerate growth rate resulting from coagulation of crystallites with agglomerates, L/t
G_c	average cluster growth rate resulting from coagulation of crystallites into clusters, L/t
G_e	effective growth rate, L/t
i	growth rate kinetic order of nucleation
j	suspension density kinetic order of nucleation
k	coagulation constant, $1/t$
k_a	size-independent surface area shape factor
k_c	average coagulation constant of crystallites into clusters, $1/t$
k_N	nucleation constant
k_r	surface reaction rate constant

[1] Units are represented as; M = mass, L = length, t = time, # = number, T = temperature

k'	nucleation constant
k'_x	average coagulation constant of crystallites into clusters, 1/t
k''_x	average coagulation constant of crystallites with clusters, 1/t
L	particle size (volume-equivalent-diameter), L
$\overline{L}$	average particle size, L
m_p	mass of particles, M
m	mass of particles per unit volume of suspension, M/L^3
M	suspension density per unit volume of suspension, M/L^3
M_F	suspension density fraction
n	particle population density, $\#/(L \cdot L^3)$
$\overline{n}$	average population density in size range ΔL, $\#/(L \cdot L^3)$
N	total number of particles per unit volume of suspension, $\#/L^3$
N_A	Avagadro's number, #/mole
P	solute production rate per unit volume of suspension, $M/(L^3 \cdot t)$
Q	total feed flow rate, L^3/t
r	particle radius, L
R	gas constant, $(L^3 \cdot P)/(T \cdot mole)$
S	degree of supersaturation, M/L^3
t	time, t
T	absolute temperature, T
$T_{1/2}$	half-time of coagulation, t
v	sample volume used in Coulter counter analysis, L^3
V	suspension holdup volume in precipitator, L^3
w	mass fraction of particles per unit volume of suspension
W	total mass fraction per unit volume of suspension

X	laminar film thickness, L

Greek symbols

ε	dielectric constant
μ	electrophoretic velocity, L/t
ν	kinematic viscosity, L^2/t
ρ	particle density, M/L^3
τ	residence time, t

Superscripts

o	particles of nucleate size

Subscripts

a	agglomerates
c	clusters
d	dominant size
m	minimum size
o	initial conditions
T	crystallites + clusters + agglomerates
x	crystallites
1	conditions that exist for the particles at the lower edge of the size range ΔL
2	conditions that exist for the particles at the higher edge of the size range ΔL

INTRODUCTION

The generation of electricity by nuclear power reactors has been expanding to help fulfill current energy demands as some fossil fuel reserves are being drastically reduced. With this expansion, the desire and need for a dependable, easily controllable, and economical nuclear fuel fabrication process has emerged.

The fuel for nuclear reactors must be able to exist within a very hostile environment which places great demands on its chemical and physical properties. The reactor fuel must be stable under high thermal stress, high radiation fluxes, have a high thermal conductivity, be able to retain fission products, and have an in-core lifetime consistent with a high burnup.

Presently, most light water reactors are using UO_2 fuel pellets even though they are brittle and have a low thermal conductivity. This is because these disadvantages are offset by the advantages of having a high melting point, being chemically stable with reactor coolants and cladding materials at high temperatures, having an isotropic structure which is stable under irradiation at temperatures approaching its melting point, and having a crystal structure which can accommodate significant quantities of solid and gaseous fission products (52,96).

These physical properties are governed by the density, grain size, pore volume distribution, pore size distribution, and shape of the UO_2 pellet (42,73,83). Although the optimum structure has not yet

been firmly established, it has been found that light water reactor pellets should be cylindrical with a length to diameter ratio of 1 to 1.5, have a diameter of approximately 1.25 cm and be centerless-ground to $\pm$0.005 mm for accurate control of fuel-sheath distance and radial swelling. Both ends should be dish shaped with end chamfers and some minimum shoulder width to allow for swelling, to prevent ridging, and to avoid excess chipping during loading. The oxygen to uranium ratio should be near stoichiometric composition for increased thermal conductivity and retention of fission gas. The pellet should have high density of 92 to 95% theoretical, a uniform porosity to avoid any density distribution, a large grain size of about 10 μm, and a pore size distribution such that the majority of pores are 10 μm and larger in order to prevent irradiation induced densification (15,19,22,40,42,52,64,73,83,95,96,99). Many of these properties are determined by the microstructure of the pellet.

The importance of shape and microstructure is clearly evident from in-core performance tests of oxide fuels. If this performance is poor, then the overall fuel cycle becomes more costly because of increased fuel inventory requirements, fuel element failures, increased and unscheduled reactor down times, and lower maximum allowed power limits. Past experience has shown that restructuring of the pellet, fission product behavior, irradiation-induced densification, fuel-cladding interaction, fuel element dimensional stability, and internal hydriding of zircaloy-clad fuel rods can all be related to the UO_2 pellet's shape and microstructure (67,94,108).

Upon initial heating of the fuel, a high thermal gradient is established with the highest temperature being at the centerline of the fuel pellets. In a few hours, the fuel will be restructured as a result of void migration. The high temperature gradient causes the pores near the central portion of the pellet to migrate towards the pellet's centerline through an evaporation-condensation mechanism. This results in a central void surrounded by large columnar grains (19,34). The void migration rates are highly temperature dependent and cause the outer radius of this annular region to be sharply defined. After the formation of the structure, the temperatures and thermal gradients in this region become considerably lower because of the increased thermal conductivity which, in turn, lowers future void migration rates. The amount and size distribution of the fabricated porosity will, therefore, affect the amount of its initial restructuring.

An inventory of gaseous and solid fission products will build up inside the UO_2 matrix as fission takes place. The oxygen to metal ratio will gradually increase, the fuel pellet will swell, and the chemical composition will be constantly changing. Redistribution of the fission products will result in the formation of gas bubbles, inclusion phases, and solid solutions within the UO_2 matrix (16,45,50,65). This redistribution has been shown to be affected by radiation, which enhances diffusion processes at low temperatures and controls the process of gas bubble nucleation and growth by resolution mechanisms (46). A dynamic equilibrium will

exist between the gas bubbles, which remain very small and are under very high pressures, and the gas which is dissolved in the fuel matrix. Some of these bubbles will migrate toward grain boundaries where they accumulate and may interlink, forming a connecting path to the exterior of the pellet and then escape into the gas plenum. Gas bubbles near the hotter central portion of the pellet will migrate up the temperature gradient and reach the gas plenum through the central void. This transport of gas bubbles through the UO_2 fuel matrix is dependent upon the diffusion coefficient of the fission gas, which has been shown to be a function of both temperature and grain size (66). The average grain size of the UO_2 pellet and the amount of porosity will consequently affect the redistribution of fission products, the amount of fission gas release, and the amount of fuel pellet swelling.

One of the most vivid examples of the effects of pellet microstructure on fuel performance is that of irradiation-induced densification in which the density of the fuel increases at temperatures far below those at which density increases can be induced outside of a reactor. This type of densification, which was first experienced in 1972, resulted in bowed, collapsed, and leaking fuel rods (32). The degree of densification was found to be controlled by the amount of burnup and the microstructure of the fuel, particularly its pore size distribution, total porosity, and grain size (24,49,75,98).

Densification should really be considered in the context of two concurrent processes, pore removal and swelling, with pore removal

being at the beginning of fuel life and fuel swelling becoming dominant at burnups of about 4,000 to 12,000 MWd/T. The mechanism for this irradiation-induced densification is believed to be the result of fission-induced resolution of pores followed by vacancy diffusion to vacancy sinks such as grain boundaries or other pores. This pore resolution is supposedly a result of the thermal effect of a fission fragment, which tends to vaporize all the matter in a cylindrical region approximately 10 μm long and 70 A in diameter. If such a region intersects the surface of a pore, then a large portion of the vaporized matter erupts violently into the pore as a mixture of liquid and vapor, creating a high concentration of vacancies which may diffuse to grain boundaries and cause densification, or may reprecipitate on pores that are not instantaneously homogenized. The latter effect tends to give the larger pores greater stability than smaller ones.

In order to prevent irradiation-induced densification, the microstructure of the UO_2 must be controlled so that the fabricated pellet has a density greater than 94% theoretical, an average grain size greater than 10 μm, and a pore volume distribution such that the pores at median volume have a diameter greater than 1 μm (49,75). However, the complete elimination of porosity is undesirable for high burnup and fission product retention (20,107), and for minimizing both circumferential and axial cladding strain which results from pellet-cladding interaction (1,41).

The density and the amount of open porosity is also important

in regard to the internal hydriding of zircaloy-clad fuel rods, since the main source of hydrogen in fuel rods is due to the surface adsorption of hydrogen (84).

Aside from the need to control microstructure from a performance standpoint, there is an additional need from a fuel fabrication standpoint. Although there is little published data on the physical problems of UO_2 pellet fabrication by the industry, one paper on the experience in a fabrication facility (101) contained information indicating that the economics and efficiency of the fabrication process can be significantly affected by control of the pellet's microstructure. Specifically, this is evident in the quantity of recycled scrap powder from rejected pellets, equipment maintenance, amount of fuel inventory, and amount of plant down time. For example, pellets with invisible, internal cracks often break causing damage to grinding wheels. Maintenance of equipment such as this is not an easy task, especially if mixed-oxide fuel is being fabricated. Equipment failures also cause intermediate product storage problems for other process steps unless the entire fabrication process is shut down.

In addition to the maintenance problems, some of the process steps may affect product uniformity, especially if they are operated manually. Improved automation and control of the fabrication process would not only improve pellet microstructure control and product uniformity, but would also improve the overall efficiency of such a facility.

There is general agreement among the people working in the area of fuel fabrication that the physical properties of the UO_2 pellet depend upon the properties of the uranium oxide powders and upon the pellet fabrication technique. The effects of the variables in the fabrication processes, which include precipitation, calcination, reduction, milling, granulation, pressing, sintering, and grinding, depend not only on the technique used but also on the properties of the powder being treated. As a result of this very complicated interdependency, data published in the literature present a very confusing picture because of the often conflicting opinions on the effects of various fabrication variables.

Most of the work done by others has involved powder characterization by grain size, surface area, and tap-density, with average grain size and particle size being determined in some cases from the surface area. This alone is not enough to characterize the powders, but should be used in conjunction with analysis of particle size distribution, pore volume distribution, particle morphology, and particle structure. Without fully characterizing powders at every step in the process, results of experiments correlating process variables with changes in powder characteristics could be questionable. This is particularly true for surface area measurements which depend not only on particle size, but also on size distribution, morphology, and structure.

Particle descriptions in the literature often present a vague and confusing picture because the definition of what comprises a

"particle" is unclear. Apparently what are really being formed are individual crystallites which are nucleated and grown, clusters of these crystallites which are held rather firmly together, and finally, agglomerates of these clusters which are held loosely together. The crystallites are usually referred to as platelets because of their wafer-like shape, while the clusters and agglomerates are usually referred to as particles. Adequate powder characterization must distinguish between these features and include analysis of size distribution, pore volume distribution, and morphology of each type of particle.

The research work involved in this project was devoted to the study of the continuous precipitation of ammonium polyuranate and had the following objectives: (1) to better characterize the precipitate with respect to particle structure, particle size distribution, and particle morphology, (2) to develop a more scientific basis for determining the operating conditions of the precipitator, (3) to determine how to alter the particle structure of the precipitate, and (4) to develop a mathematical model of the precipitation process.

LITERATURE REVIEW

The production of UO_2 powder has for many years been carried out by reduction of UO_3 or U_3O_8, and most of the early work involved the production of UO_3 by thermal denitration of uranyl nitrate. This thermal denitration was performed in heated kettles which proved to be expensive to operate and maintain because of the high temperatures needed and the corrosive atmosphere generated (72,88). A subsequent process using aqueous uranyl nitrate and a moderate temperature involves the precipitation of uranium as ammonium polyuranate (APU), and has been developed to an industrial scale (19). The APU precipitate yields a more chemically reactive UO_3 powder than does the thermal denitration process (43). The UO_2 powder produced through the APU route has been shown to be more reactive and of higher density than UO_2 prepared by other methods (18,22,25,43,61,86). In some cases, the fuel production was even more economical because the UO_2 powder could be cold-pressed without the addition of a binder (96).

APU can be precipitated from uranyl nitrate solution by any of several methods; (1) addition of ammonium hydroxide, (2) addition of ammonia gas, (3) addition of ammonium carbonate, and (4) addition of urea which upon heating decomposes with the generation of ammonia. The highest density UO_2 is produced from APU which has been precipitated by the addition of ammonia (25), and therefore most of the precipitation studies have involved only methods 1 and 2.

The precipitate is often referred to as ammonium diuranate; however

this compound has never been isolated from solution and the exact composition is still in question (8,17,69,86,113). The large number of compounds and complexes which have been postulated to be formed during the reaction of uranyl nitrate and ammonium hydroxide indicate the complexity and uncertainty in the reactions and mechanisms involved. All of the studies have indicated that equilibrium is established slowly and that the addition rate of the reactants will affect the shape of the pH curve.

The titration curve has been found to have two inflection points, as shown in Figure 1. According to Sutton (103), initially hydrolysis of UO_2^{++} forms $U_2O_5^{++}$ and $U_3O_8^{++}$ ions. As alkali is added, the complexes $U_3O_8(OH)^+$ and $U_3O_8(OH)_2$ are formed at the first inflection point ($OH^-:UO_2^{++}$ mole ratio = 1.66). Further addition of alkali continues the hydrolysis and the second inflection point ($OH^-:UO_2^{++}$ mole ratio = 2.33) results from the formation of $U_3O_8(OH)_3^-$, $U_3O_8(OH)_4^=$, etc.

Palei (82) reported a different scheme which indicated that as the $OH^-:UO_2^{++}$ ratio increases from 0 to 1, $UO_2(OH)^+$ and $UO_2(UO_3)_nOH^+$ are formed. Then as this ratio increases from 1 to a range 1.4 - 1.6, a metastable colloidal solution begins to form in which polymers of $UO_2(UO_3)_nOH^+$ are unstable and pass into colloidal uranyl hydroxide. This colloidal hydroxide gradually decomposes and UO_3-nH_2O is precipitated. As the $OH^-:UO_2^{++}$ mole ratio increases from the range 1.4 - 1.6 to 1.9 - 2.0, uranyl hydroxide ($UO_2(OH)_2$) is precipitated, and further addition of alkali initiates the change of the hydroxide into uranates and polyuranates.

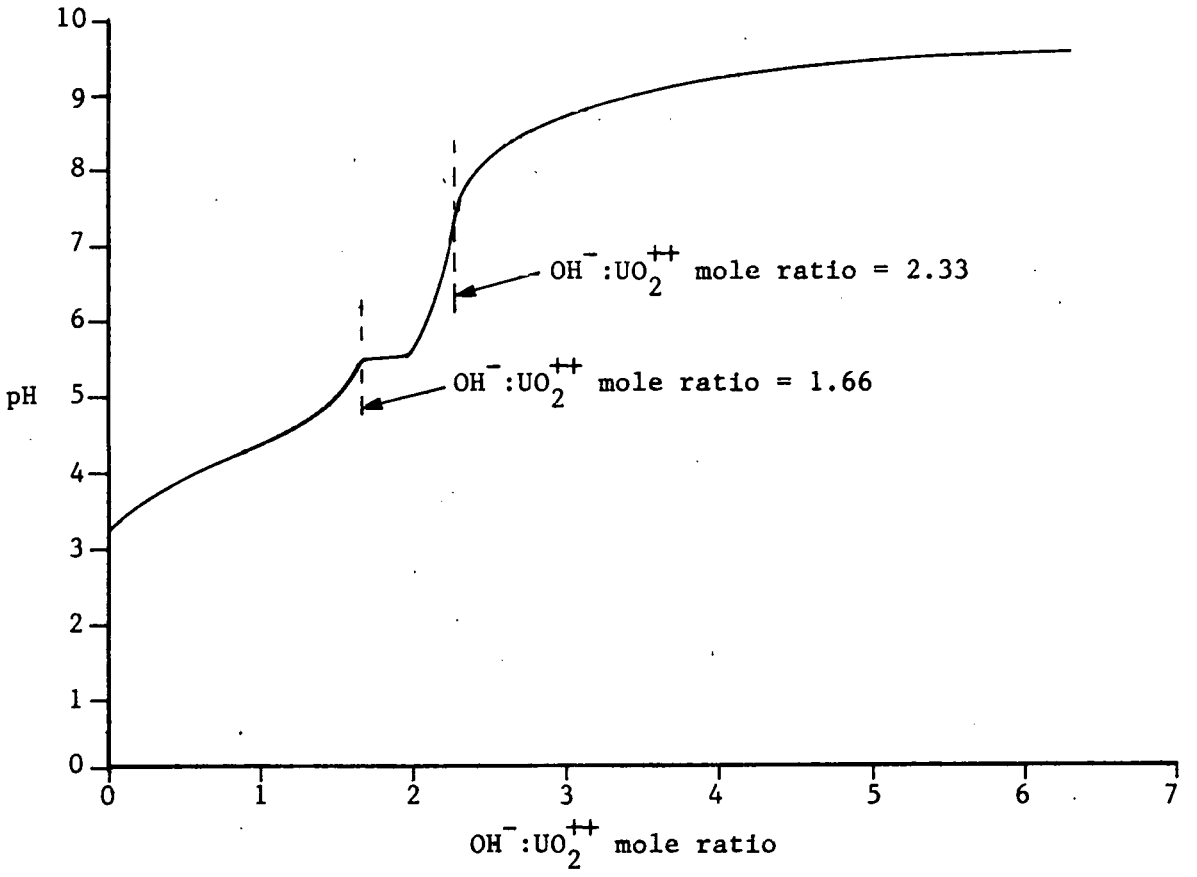

Figure 1. Titration curve showing two inflection points for uranyl nitrate being titrated with ammonium hydroxide

Deptula (38) agreed with Sutton's analysis up to the first inflection point. He then postulated a hydrolysis reaction leading to the formation of $UO_2[(OH)_2UO_2]_4^{++}$ at the first inflection point, and then that an easily hydrolyzable uranate, $[(NH_4)_2O]_3 \cdot [UO_3 \cdot H_2O]_{20} \cdot 13H_2O$, is formed at the second inflection point. He believes, as does Stuart and Whateley (102), that the ammonia is present as the NH_4^+ ion and its presence is the result of cation exchange with H^+ ion, which explains the leveling off of pH as alkali is added. They also believe that the ammonium uranate system is a single phase in which the NH_3:U ratio can be varied continuously.

In contrast to the above results, Cordfunke (26,27,28) and Debets and Loopstra (35) have reported that under equilibrium conditions four compounds may exist:

I $UO_3 \cdot 2H_2O$, pH = 3.5

II $3UO_3 \cdot NH_3 \cdot 5H_2O$, pH = 4-7

III $2UO_3 \cdot NH_3 \cdot 3H_2O$

IV $3UO_3 \cdot 2NH_3 \cdot 4H_2O$ } pH > 7

They indicated that x-ray analysis of these compounds showed the presence of essentially indentical hexagonal or pseudo-hexagonal subcells. All four compounds belong cyrstallographically to the same series and can be represented by the general formula $UO_3 \cdot xNH_3 \cdot (2-x)H_2O$, with compounds I and II being stable in water while compounds III and IV are stable only in concentrated ammonia. The structure consists of layers of the composition $UO_2(O_2)$ with the additional oxygen and nitrogen atoms between these layers. They

believe that the ammonia is not directly linked with the uranium atom, and that it is present as NH_3 rather than NH_4^+.

Because of the wide range of compositions mentioned above, the precipitate to be studied in this work will be referred to as ammonium polyuranate (APU), without any specific composition implied.

Opinions regarding the effects of the various process steps on the physical character of uranium powders and on the microstructure of the final UO_2 pellet are quite varied among the people working in this area. It has been reported that: (1) no correlation exists between the surface area of APU and that of the UO_2 powder (6,27,37,68), (2) no correlation exists between APU precipitation variables and the sintered UO_2 density (4), (3) the chemical reactivity and particle structure of APU has little affect on that of the uranium oxide powders (4,69), and (4) rigid control of the precipitation, when using NH_4OH, is not necessary, and almost no control is necessary when using NH_3 (17). On the other hand, it has also been reported that: (1) APU does yield UO_2 of similar surface area (4), (2) the precipitation conditions do affect the UO_2 sinterability (17,37), (3) the chemical reactivity and particle structure of APU affects the reactivity and structure of uranium oxide powders (15,31,37,40,62,91), (4) the particle structure is determined by the precipitation conditions, which controls the crystallite size, morphology, and agglomerate size of the APU (17,31,37,38,51,52,62,64,86,95), and (5) the chemical changes in uranium powders occur pseudomorphically at low temperatures (5,25,30,31,40,62), and similar morphologies have

been found in APU and UO_2 (5,25,62,68).

The question then arises as to why there are so many differing opinions on UO_2 powder property dependence. To understand these discrepancies in powder property dependence, one must realize that most of the powder correlations have involved only surface area and UO_2 pellet densities. Unfortunately, very few studies have involved consideration of particle structure. The measured surface area for a powder will depend upon the crystallite and agglomerate morphologies and particle size distributions. The effect of process variables on the particle structure will depend upon the structure of the particles and upon how strongly the sub-structures making up the particles are bonded together. If fracture occurs during a process step, the amount of increase in surface area will vary depending upon the internal structure of the particle (111,112). If sintering and grain growth take place, then the final grain structure and porosity will depend upon the nature of the original particles, since crystallites within agglomerates will grow together more rapidly than crystallites next to each other but contained in different agglomerates (10,14,41,62).

When a powder undergoes a change to a new compound, as during calcination and reduction, the change in particle structure will again depend upon the initial particle structure. This change from one compound to another will be accompanied by a corresponding change in the crystalline structure and will result in a volume change of the crystal unit cell, thus producing internal stresses which

may be relieved by pore formation, fracturing, or morphological change. The actual process which occurs may depend upon the bonding strength between crystallites in clusters and upon the bonding strength between clusters in agglomerates.

Two of the most significant process variables which affect the particle structure, grain structure, and surface area of the powder are the calcination and reduction temperatures. These two parameters, in conjunction with particle structure, are the reasons for many of the conflicting correlations involving surface area measurements. Depending upon the duration and temperature of reaction, the particles may fracture under stress into smaller ones or, with prolonged heating or increased temperatures, the particles may increase in size as the stresses anneal out and free sintering takes place (4,5,6,7,30,62,69,109, 111,112). The decomposition of APU into UO_3 occurs between 200 °C and 400 °C, and it has been reported that during this change the APU platelets become cracked and porous, with gaseous substances being emitted (4,111,112). As the temperature is increased to 400 to 500 °C, U_3O_8 is formed and this then undergoes free sintering as the temperature is increased above 600 °C. The UO_2 powder is then formed when the U_3O_8 is reduced in hydrogen at temperatures above 700 °C, with free sintering occurring at 900 °C. If the reaction temperatures are relatively low, but above that at which particle breakup would occur, then the overall particle structure will be retained during both the calcination and reduction steps.

The differences in the densification of UO_2 powders has been

attributed to their differences in homogeneity of microstructure, with the powders having better sinterability the finer the grain size and the more homogeneous the microstructure (31,37,40,62,64,95). After sintering, the UO_2 will contain two types of pores, small round pores (0.1 to 5μm) within former agglomerates, and irregularly shaped pores (5 to 20μm) between former agglomerates (49,64,75).

The uniformity and consistency of the UO_2 powders vary from batch to batch because of the poor control over the particle structure in present fabrication processes. Therefore, it has been common practice (2,9,12,45,51) to increase the homogeneity of the UO_2 powder by breaking up the agglomerates through ball-milling, which is a very energy intensive process. In some cases, binders such as glycol, petroleum wax, camphor, and polyvinyl alcohol are added to help agglomerate the fines and permit handling of the pressed compact (2,9,48). If a certain porosity distribution is desired in order to inhibit in-reactor densification, then sometimes pore formers such as polyolefins or carbowax are used, or a pre-slugging technique is used (49,75). Unfortunately the use of binders and pore formers during the pellet pressing step necessitates the use of a low temperature pre-sintering step to remove the organic material. If the powder structure control of the fuel fabrication process is improved, then it seems possible that ball-milling, binder addition, and pore former addition could be eliminated, saving both time and money.

At relatively low calcination and reduction temperatures, and in the absence of ball-milling and unusually high pressing

pressures, the particle structure of the initial uranium powders will determine the particle structure of the final uranium dioxide powder. This uranium dioxide particle structure will then determine the final pellet density, porosity, and grain structure. Therefore, precipitation is of primary importance since it establishes the initial particle structure upon which all future process steps will take affect. The development of a fabrication process yielding a controllable powder structure must begin with this first powder process step.

The precipitation conditions which have been investigated by other people are summarized in Table 1. It is important to note that very little specific APU particle characterization has been reported, and of those properties which have been reported, most only indicate whether the APU was amorphous and soft or dense and hard, and whether or not it possessed fast settling and filtration rates. It appears that, based upon several of the precipitation studies (5,31,40,62,86), the APU consists of small, thin, elementary platelets (0.025 to 0.5 μm) which are strongly bonded into small clusters (0.5 to 3 μm), and these clusters can then be loosely agglomerated into larger particles (2 to 30 μm). If this is indeed the case, then the desired control of the APU particle structure could be accomplished by controlling the platelet size distribution, the cluster size distribution, the loose agglomerate size distribution, and the homogeneity of the clusters and agglomerates.

Most of the investigations which have been carried out by others

Table 1. APU precipitation conditions which have been investigated by other people

Reference and date	Batch or continuous	Size of vessel (ℓ)	NH_3 or NH_4OH	$[UO_2(NO_3)_2]$ (moles/ℓ)	$[NH_3]$ (wt%)	$UO_2(NO_3)_2$ flow rate	NH_3 or NH_4OH flow rate	Temperature (°C)
43 (1956)	B	8-12	NH_3 & NH_4OH	0.0044-0.7	25.2			23
55 (1956)	B	0.5-2	NH_4OH	0.063-1.34	28			23 66
17 (1958)	B	2-4	NH_4OH	0.42-2.1	3.2-22			25 60
17 (1958)	B	2-8	NH_3	0.21-1.26	100			22 47 80
113 (1958)	C	1	NH_4OH	0.42	10-22	75 & 150-167 ml/min	8-22 ml/min	60
88,89 (1958)	C	0.25-2	NH_4OH	0.25-0.67	28			45-50

pH	Precipitation time (h)	Conditioning time (h)	Washing method	Comments about precipitation results
9.6-10.2			H_2O NH_4OH none	the APU was generally amorphous
4.5-10		1.5-20	settled H_2O NH_4OH	the precipitates were dense, firm, and filtered easily when no conditioning was used; otherwise they were buttery, slimey, and difficult to filter
7-9	0.17-2.32	0.33-48	settled H_2O	in general, higher [U] and higher temperature resulted in higher UO_2 sintered densities, but the APU filtered poorly; precipitation times greater than 1 h resulted in lower UO_2 sintered densities and filtered poorly; at 23 °C, increased pH increased UO_2 sintered density; low [U] and [NH_4OH] at 23 °C yielded APU which filtered well and resulted in high UO_2 sintered densities; conditioning had no significant affect
7	0.33-2.32	0.33-48	settled H_2O	slower precipitation times (0.33-1 h) and lower [U] (0.21-0.8 M) yielded APU which resulted in UO_2 of high sintered density
2.75-8.00	0.17	1 ℓ tank	settled & filtered H_2O	when the conditioning tank was used, NH_3 was sometimes pumped through it to reach a pH>7; they assumed that steady state was reached in 10 min since it took that long for the pH to stabilize; addition of excess NH_3 to reach a high pH did not improve the sinterability of UO_2 - contrary to batch precipitation; precipitation at pH>6.8 consistently yielded APU which resulted in high sinter densities of UO_2, however resonable filtration rates limits the pH to 7-7.5
4.7-7.2	0.33-0.83		none	the settling and filtration rates increased as the pH decreased, however all rates were 10-50 times greater than those of batch precipitations; the APU consisted of uniformly small particles which

Table 1. (continued)

Reference and date	Batch or continuous	Size of vessel (ℓ)	NH_3 or NH_4OH	$[UO_2(NO_3)_2]$ (moles/ℓ)	$[NH_3]$ (wt%)	$UO_2(NO_3)_2$ flow rate	NH_3 or NH_4OH flow rate	Temperature (°C)
88,91 (1958)	C	303	NH_4OH	0.67	28	74 ℓ/h	5.7 ℓ/h	49
70 (1958)	C	1022	NH_4OH	0.67	28	462 ℓ/h	22.7-26.5 ℓ/h	50
90 (1958)	C	303	NH_4OH	0.67	4-28	74 ℓ/h	5.7 ℓ/h	50
92 (1959)	C	8	NH_4OH	0.34-1.26	4-7			38 70

pH	Precip-itation time (h)	Condi-tioning time (h)	Wash-ing method	Comments about precipitation results
				have a higher bulk density and a lower surface area than most APU; for a pH of 5.7, the NH_3/U mole ratio was 0.138
5.7	10-336	0-72	fil-tered H_2O	this was a pilot plant operation of the laboratory work (88,89); conditioning of the APU did not affect filtration; the amount of agitation and placement of the feed entry was of primary importance, feed entry into the vortex prevents pH fluctuation and promotes rapid dilution of NH_4OH which prevents a secondary reaction producing a red-orange product with poor settling and filtration properties; for a pH of 5.7, the NH_3/U mole ratio was 0.172
5.7	days		fil-tered H_2O	this was a semi-works plant of the pilot plant (88,91); this plant produced extremely uniform calcined APU, and filtration was comparable to that of the pilot plant; for a pH of 5.7, the NH_3/U mole ratio was 0.165 (note that 76 ℓ/min of product was removed, of which 72 ℓ/min was recycled from the filter assembly)
5.7			fil-tered	this was a further report on the pilot plant (88,91); results indicated that the use of high speed mixing causing a vortex is not necessary if low $[NH_3]$ is used (4%), this also improved the filtration rates
4.8-6.5	10-20		fil-tered H_2O	steady state was achieved in 6-7 h when the mean retention time was 4 h; the heat of reaction was found to be 13±3 Kcal/(gm-M U); this APU was dried a 100°C and calcined in air at 489°C and analyzed for the % particles < 10 μm - low pH, temperature, and [U]yielded 25-60%, high pH and temperature yielded 90-100% (this calcined product came from APU which was yellow and very hard); the mean retention time for the precipitation was 1 h

Table 1. (continued)

Reference and date	Batch or continuous	Size of vessel (ℓ)	NH_3 or NH_4OH	$[UO_2(NO_3)_2]$ (moles/ℓ)	$[NH_3]$ (wt%)	$UO_2(NO_3)_2$ flow rate	NH_3 or NH_4OH flow rate	Temperature (°C)
18 (1961)	B	1	NH_4OH	0.42-1.26	28	150 ml/ min		23
25 (1961)	B		NH_3& NH_4OH	0.5	100 & 14			90
38 (1962)	B	0.05	NH_4OH	0.1	0.34		equi-libri-um, & 1 ml/ min	20
4 (1962)	B		NH_4OH	0.63	7.8			20-70
40 (1964)	B		NH_4OH	0.004-0.22	28			
37 (1966)	B		NH_4OH	0.1-0.7	0.34-2.4		equi-libri-um, & 0.15 M/ (min-M of U)	20-70

THIS PAGE

WAS INTENTIONALLY

LEFT BLANK

pH	Precipitation time (h)	Conditioning time (h)	Washing method	Comments about precipitation results
7.2			filtered	this was a pilot plant of the process described in (113); the APU from this process yielded UO_2 which was sinterable to a high density
8		1	filtered H_2O	the APU precipitated with NH_4OH had irregular shapes and sizes, however when NH_3 was used, the APU consisted of very fine, minute particles
2-9			filtered H_2O & alcohol	precipitation started at a NH_3/U mole ratio of 1.6; precipitation under equilibrium conditions yielded a coarse grained and easily filterable precipitate, however nonequilibrium conditions resulted in an amorphous and difficult to filter APU
7-12	0.05-1	0.33-0.5	settled H_2O	slower NH_4OH addition rates, higher pH, and lower temperatures yielded faster settling rates of APU
6-7			filtered	very low [U] yielded elementary APU platelets which were very thin and of uniform size (0.1-0.2 μm), these built up small clusters (0.2-0.3 μm), and then secondary agglomeration resulted in homogeneous particles in a relatively uniform size distribution (2-32 μm); at high [U] the APU platelets were larger (0.2-0.5 μm), and secondary agglomeration yielded inhomogeneous particles (2-32 μm) whose size distribution favored the smaller particles
8.5	0.25-8		settled H_2O	the specific surface of APU decreased as [U] increased when precipitated under equilibrium conditions at 20 °C, however at 70 °C the specific surface increased; the density of the APU and of the sintered UO_2 decreased as the [U] increased; precipitation at faster flow rates yielded APU with a higher specific surface, and this specific surface increased as the [U] increased

Table 1. (continued)

Reference and date	Batch or continuous	Size of vessel (ℓ)	NH_3 or NH_4OH	$UO_2(NO_3)_2$ (moles/ℓ)	NH_3 (wt%)	$UO_2(NO_3)_2$ flow rate	NH_3 or NH_4OH flow rate	Temperature (°C)
31 (1967)	B	10	NH_4OH	0.70	28			60
86 (1968)	C	1.9	NH_3	0.63	100	270 ml/ min	6.2 ℓ/ min	45-60
68 (1972)	B	≈6	NH_3	0.5	100		0.25-0.5 M/ min	22-62
62 (1971) 5 (1972)	C	~2 ℓ & ~1.6 ℓ	NH_4OH & NH_3	0.29	28 & 22	total residence time of 8 min - 64 min		50,80
63 (1975)	C	25 ℓ	NH_4OH & NH_3	0.18-0.30	28	1-1.2 ℓ/ min	75-85 ml/ min	50

THIS PAGE

WAS INTENTIONALLY

LEFT BLANK

pH	Precipitation time (h)	Conditioning time (h)	Washing method	Comments about precipitation results
7.5	0.25	0.25	filtered dilute NH_4OH	the APU precipitate consisted of loose agglomerates (1-3 μm) of small platelets
7.2	1.92	14 ℓ tank overflowing onto a filter	filtered H_2O	the continuously agitated conditioning tank evens out small variations in the precipitate and enhances uniformity of the filter cake; the APU consisted of loosely agglomerated crystallites which were very thin and had a maximum size of 0.025-0.5 μm and a mean size of 0.25 μm
5-9.2	0.27		centrifuge	the affect of the free $[HNO_3]$ in the uranyl nitrate solution was also investigated, and the APU was dried in a microwave oven; changing the process variables was found to affect the UO_2 surface area about as much as the reduction temperature could; cross affects were not additive
3.5-8.4		none,	decantation H_2O none	both 1 stage and 2 stage precipitation was investigated, pH was considered the most important variable because it determined agglomerate size and thus filtration rates; precipitation at pH=3.4 yielded 20-24 μm particles, precipitation at pH=7.2 yielded 3 μm particles; close control is necessary when pH=7.2 to avoid pH fluctuations and changes in particle size; stirring rates had little affect as long as complete mixing was present; washing APU had no affect; when pH=3.5 crystallites were 0.02-0.3 μm, when pH=7 all crystallites were < 0.1 μm; the use of NH_3 gas diluted 1:3 with air had little affect on APU precipitate; increasing temperature from 50 °C-80 °C had little affect also
7.2 7.5 8.0		85 ℓ tank	none	

have involved batch precipitation with ammonium hydroxide and in some cases ammonia gas. Results from these studies have indicated that good APU filtration rates are obtained with high pH (4), low uranium and ammonium concentrations (17), slow ammonium hydroxide addition rates (4,38), high temperature (4), no precipitate conditioning prior to filtration (55), and in some cases with low pH and low temperature (17). The use of ammonia gas instead of ammonium hydroxide has also been reported to yield a very fine and difficult to filter precipitate (25).

The precipitation studies which have involved continuous precipitation have not clarified the effects of precipitation variables any better, except to indicate that a more uniform product is formed with continuous precipitation (87,88,89). High filtration rates and settling rates have been obtained with low pH (5,62,88,89), large amounts of agitation (72,86), low ammonium hydroxide concentrations (90,91), and with increased residence time (62). The pH has been reported to affect the agglomerate size (5,62), with 20 to 25 μm particles being formed when pH = 3.5, and 3 μm particles being formed when pH = 7.2. The effects of conditioning the APU after precipitation have not been consistent. In some cases, conditioning has been reported to even out small variations in the precipitate and enhanced uniformity of the filter cake (55,69,86), while in other situations conditioning has been found to have no significant effect (17,88,91).

The precipitation of APU below a pH of 4 to 5 has been reported to be incomplete (38,62,88,113), and slightly incomplete below a

pH of 5.5 to 7.5 (62,88). The solubility of APU has also been reported to be a function of the pH (100), varying from 16 g/ℓ at pH 3.5 to 10^{-14} g/ℓ at pH 9. Therefore, lower values of pH, and presumedly higher temperatures, result in lower degrees of supersaturation and consequently larger crystals (62).

A similar effect has been found with increased uranium concentration, which yielded larger APU platelets (40). One would normally expect this increased uranium concentration to yield higher supersaturations and therefore smaller crystals, however, this effect is offset by the fact that increased uranium concentration lowers the pH and consequently lowers the supersaturation. It also has been shown (40) that the rate-controlling step for the growth of APU platelets is the diffusion rate of the UO_2^{++} ion. Increasing the uranium concentration will then increase the diffusional flux, which increases the platelet growth rate.

The operating conditions which have been preferred for APU precipitation are indicated in Table 2. Most of these conditions include the use of ammonium hydroxide (28 wt% NH_3), uranium concentrations between 0.4M and 0.8M, and a reaction temperature between 40 °C and 65 °C. In some cases (17,68,86), ammonia gas has been used instead of ammonium hydroxide because it is easier to handle. Batch precipitations have also been used in some cases because they can be easier to operate on a small scale, are attractive if centrifuging the APU is being considered, and may ease worries over criticallity and accountability (46).

Table 2. Preferred APU precipitation conditions

Reference and date	Batch or continuous	Size or vessel (ℓ)	NH_3 or NH_4OH	$[UO_2(NO_3)_2]$ (moles/ℓ)	$[NH_3]$ (wt%)	$UO_2(NO_3)_2$ flow rate	NH_3 or NH_4OH flow rate	Temperature (°C)
55 (1956)	B		NH_4OH	0.67	28			65.5
17 (1958)	B		NH_4OH	0.42-0.84	22			60
17 (1958)	B		NH_3	0.21-0.8	100			22-80
113 (1958)	C	1	NH_4OH	0.42	10-22	75-165 ml/min		60
89 (1958)	C		NH_4OH	0.67	28			45-50
87,88 91 (1958)	C		NH_4OH	0.67	28			50
90 (1958)	C		NH_4OH	0.67	4-7			38 50
18 (1961)	C	1	NH_4OH	0.42-1.26	28	150 ml/min		23

THIS PAGE

WAS INTENTIONALLY

LEFT BLANK

pH	Precipitation time (h)	Conditioning time (h)	Washing method	Why these conditions were chosen
9.8		none		these conditions produce an easily filterable APU; at [U] above 0.67 M, it was difficult to maintain a homogeneous slurry during filtration, indicating the possibility of slurry transfer difficulties
9-9.3	<1			these conditions produce APU which yields UO_2 of high sintered density
7	0.33-0.83			these conditions produce APU which filters well and yields UO_2 of a high sintered density
7-7.5				these conditions will produce APU which is filterable and can be reduced to a highly sinterable UO_2 powder
5.7				these conditions produce APU with better settling and filtrating properties than APU produced through batch precipitation
5.7				these conditions, along with high speed mixing to produce a vortex for feed entry, were necessary to produce APU with good settling and filtrating properties in the pilot and semi-work plants of the laboratory process (89)
4.8-6.5				results from the pilot plant (88,91) indicated that the use of a low $[NH_4OH]$ eliminated the need of a vortex for feed entry, and the APU still had good settling and filtrating properties
7.2				in this pilot plant of the laboratory process (113), critically was a geometry limitation; this process consistently yielded APU which could produce UO_2 powder which could be sintered to a high density; it was also suggested that spray washing of the APU on the filter belt be investigated

Table 2. (continued)

Reference and date	Batch or continuous	Size of vessel (ℓ)	NH_3 or NH_4OH	$[UO_2(NO_3)_2]$ (moles/ℓ)	$[NH_3]$ (wt%)	$UO_2(NO_3)_2$ flow rate	NH_3 or NH_4OH flow rate	Temperature (°C)
38 (1962)	B		NH_4OH	0.1	3.4			20
4 (1962)	B		NH_4OH	0.63	28			20
40 (1964)	B		NH_4OH	0.004	28			
37 (1966)	B		NH_4OH	0.5	0.34		0.15 M/(min-M of U)	20 70
86 (1968)	C	1.9	NH_3	0.5	100	270 ml/min	6.2 ℓ/min	45-50
68 (1972)	B	≈6	NH_3	0.5	100		0.5 M/min	30-60
62 (1971) 5 (1972)	C	2	NH_4OH	0.29	22-28			50
63 (1975)	C	25	NH_4OH		28			50

pH	Precipitation time (h)	Conditioning time (h)	Washing method	Why these conditions were chosen
				precipitation under these conditions with the NH_4OH flow rate such that equilibrium is allowed to be established produces a coarse grained and easily filterable APU
8-9				precipitation under these conditions and slow addition rates of NH_4OH yields APU with good settling and filtrating properties
6-7				precipitation under these conditions produces a more homogeneous APU particle which yields a UO_2 powder which favors rapid grain growth and densification during sintering
8.5				these conditions yield APU with a high specific surface and density; the particles are homogeneous and have a fine grain structure, which results in a more sinterable UO_2 powder
7.2		14.3 ℓ tank		these conditions produce a uranate which results in a sinterable UO_2 powder
8-8.5			none	in addition to these conditions, the free $[HNO_3]$ is 0.3 N or less, and the APU is centrifuged and dried in a microwave oven; this produces APU which has better handleability because it breaks up easier and is more free flowing
7.2		none	none	these conditions produced APU which filtered reasonably, contained no large agglomerates, and produced sinterable UO_2; 1 or 2 stage precipitation could be used
7.2-8.0		8.5 ℓ tank	none	these conditions can produce APU which filters reasonably well and results in a high density UO_2 pellet with a uniform microstructure

The preferred pH for continuous precipitation is between 4.8 and 7.2, while the final pH for batch precipitation is preferred between 7 and 9.8. The primary reasons that these conditions were chosen were to achieve fast APU settling and filtration rates and to produce a UO_2 pellet of high density and with a homogeneous grain structure. It is proposed in this work, however, that the precipitation conditions be based solely upon some desired APU particle structure rather than good settling and filtration rates. This particle structure can then be controlled in subsequent calcination and reduction steps to yield some desired UO_2 particle structure. If such precipitation conditions result in filtration difficulties, then the APU can still be separated from the liquid by centrifuging.

It seems that in order to achieve a consistently uniform product, continuous precipitation should be used in conjunction with ammonium hydroxide and vigorous agitation (70,88,89,90,91). This would avoid local pH fluctuation and provide a more controllable precipitation process. It appears that the APU particle structure should be controlled primarily through the pH, since it has the greatest influence on the cluster and agglomerate size, as indicated by the settling and filtration rates (44,88,89) and by scanning electron micrographs (62). Temperature can be used to affect cluster and agglomerate size to a lesser extent (4,92), and the uranium concentration can be used to affect both the homogeneity and size of the clusters and agglomerates (37,40,62). The size of the APU platelets, as mentioned previously, can be controlled through the

pH, temperature, and uranium concentration.

It is difficult to determine at the present time what the ideal APU particles should be like. It has been reported that, to achieve a high density UO_2 pellet having a fine, homogeneous grain structure, the APU should consist of loosely agglomerated particles of around 3 μm in diameter (5,62,63). However, to prevent inreactor densification the UO_2 pellet should have a large fraction of voids greater than 1 μm and large grains of around 10 μm in diameter (49,75); and this can be accomplished by using strongly agglomerated APU particles of around 10 μm in diameter (62). Perhaps the ideal APU precipitate will actually consist of some optimum ratio and size distribution of these two types of particles. It also appears that the possibility exists for the elimination of ball-milling, the use of binders, and the use of pore formers, if the appropriate APU particle structure and particle size distribution can be obtained from the precipitator in a controllable manner.

KINETICS OF PRECIPITATION

Precipitation may be considered a special case of crystallization, where not only a phase change is taking place but also a chemical reaction. In many cases the precipitate is sparingly soluble and the large production rate involved generates an unusually high level of supersaturation. As will be shown later, this high level of supersaturation favors high nucleation rates rather than crystal growth, yielding many submicron crystallites. In addition to these characteristics, the chemical reaction will usually necessitate the presence of other ions which, in conjunction with the large number of crystallites present, may cause various degrees of coagulation.

Crystallization, on the other hand, usually involves the phase change of a fairly soluble solute from a relatively pure concentrated solution at levels of supersaturation lower than normally encountered during precipitation. This type of situation favors crystal growth rather than nucleation, and yields crystals much larger than submicron. Therefore, one may generalize that crystallization will involve relatively slow processes and yield relatively large crystals, whereas precipitation will involve more rapid processes and yield very small crystallites which may coagulate into larger particles. It should also be noted that precipitation does not always yield a crystalline product, but may yield amorphous and even gel-like products (105).

The theory of particle size distributions from a continuous

mixed-suspension, mixed-product-removal (MSMPR) precipitator to be presented in this section is based upon the theory of crystal size distributions from MSMPR crystallizers, which have been thoroughly examined by Randolph and Larson (87). The general development of the kinetic model of continuous precipitation will follow the assumption that three processes may take place simultaneously: (1) crystal nucleation and growth, (2) primary coagulation, and (3) secondary coagulation. All three of these processes have been reported in the literature to occur during precipitation. The combining of them into a continuous precipitation model with interpretation of the coagulation processes by average coagulation growth rates, as developed in this work, has not been previously reported. To help with the development of this model, it will be necessary to distinguish between three types of particles: (1) crystallites, (2) clusters or primary coagulated particles, and (3) agglomerates or secondary coagulated particles.

Nucleation

The formation of a crystal in a homogeneous fluid requires that an energy barrier be scaled. The total excess free energy between a solute particle and the solute in solution is the sum of the surface excess free energy and the volume excess free energy. The excess free energy tends to be minimized, and this is accomplished through crystal growth or dissolution. The energy necessary to form a new crystal is called the critical free energy, which is a maximum on

a free energy diagram. If the number of molecules which come together in solution is less than the number required to reach the critical free energy, then the cluster will redissolve. This molecular interaction is proportional to the supersaturation, which is the measurable quantity that gives rise to nucleation and growth of crystals.

Crystal formation can result from homogeneous nucleation, heterogeneous nucleation, secondary nucleation, and attrition. Homogeneous nucleation is the formation of crystals as a result of only supersaturation. Heterogeneous nucleation is the formation of new crystals from the presence of submicroscopic, insoluble, foreign matter, and occurs at lower levels of supersaturation than is required for homogeneous nucleation. At still lower levels of supersaturation secondary nucleation takes place, which is the formation of new crystals induced by the interaction of suspended solute crystals. And finally, attrition is the mechnical degradation of crystals whose pieces become growing crystals. Of these types of nucleation, heterogeneous and secondary nucleation are generally the most important for industrial crystallizers, however homogeneous nucleation will also be shown to be important in precipitators.

Nielsen (79) notes that the fundamental expressions for the rate of homogeneous nucleation is given by

$$B = C \exp(-\Delta G_{crit}/kT) \qquad (1)$$

where C is a constant, k is Boltzman's constant, T is the absolute temperature, and ΔG_{crit} is the critical free energy. Randolph and Larson (87) have indicated

that Equation (1) can be approximated by the well-known Miers nucleation model which accounts for the observed fact that at low levels of supersaturation, nucleation is not present. This model is based on the concept of a metastable region whose concentration, C_m, is greater than the saturation concentration, C_s. They also reported that in most inorganic systems it appears that C_m is very close to C_s, and that considerable success has been achieved by an empirical formula which assumes C_m is equal to C_s,

$$B^o = k^i(C-C_m)^i \approx k'(C-C_s)^i \tag{2}$$

or $$B^o = k's^i \tag{3}$$

where C is the solute concentration, k' is a constant, and s is defined as the supersaturation, $C-C_s$.

In some instances secondary nucleation is important, and therefore Equation (3) is not adequate as a representation of the nucleation rate. In situations of this type, the dependence of the frequency and energy of crystal-crystal contact and crystal-agitator contact is accounted for by multiplying Equation (2) by the suspension density, M, raised to some power.

$$B = k' M^j s^i \tag{4}$$

Crystal Growth

Crystal growth from solution requires two successive steps, a diffusional transport step to the crystal surface and a surface reaction step in which the molecule is oriented into the crystal lattice. The growth rate is said to be diffusion-controlled if the

growth rate is limited by the rate of diffusion through a laminar film as is usually the case in nonagitated systems. However, in some agitated systems the growth rate will reach a maximum as the agitation increases, which is consistent with the concept of diffusion-controlled growth at low relative solution velocities and surface reaction controlled growth at high relative velocities.

Most experimental evidence (87) for crystal growth shows an approximate first order relationship with supersaturation. A mass growth rate equation which has met with success and includes diffusional effects and surface reaction effects is

$$\frac{dm}{dt} = \frac{DA'}{X + (D/k_r)} (C-C_s) \tag{5}$$

where D is the diffusion coefficient, X is the film thickness, A' is the surface area of the crystal, and k_r is the surface reaction rate constant.

If the growing particles can be represented by some characteristic dimension, then one can apply size-invariant surface area and volumetric shape factors, k_a and k_v respectively. The product of the square of the characteristic dimension with the surface area shape factor determines the particle's surface area, and the produce of the cube of the characteristic dimension with the volumetric shape factor gives the particle's volume. Introducing these shape factors into Equation (5) yields

$$k_v \rho \frac{d(L^3)}{dt} = \frac{Dk_a L^2}{X + (D/k_r)} s \tag{6}$$

where ρ is the density of the crystal and s is the supersaturation. This equation can also be written as

$$\frac{dL}{dt} \equiv G = k^* s \tag{7}$$

where G is defined as the size-independent growth rate and k^* is a constant with the value $Dk_a/k_v 3\rho[X+(D/k_r)]$.

Coagulation

The particles of an aqueous suspension may gain, lose, or share electrons by forming hydrogen or dipolar bonds with water or ions from the liquid medium. This preferential ion absorption gives rise to a diffuse double layer of ions which produces an electrostatic potential gradient about each particle causing them to repel each other (79,81,105). It is this phenomenon, particularly that portion of the electrostatic potential called the zeta potential, which is responsible for the stability of many colloid suspensions (81).

The present picture of the diffuse double layer and the resulting potential gradient about a particle (in this case an electronegative particle) is shown in Figure 2. Note that a tightly fixed layer of positive ions, called the Stern layer, surrounds the particle and that the potential gradient across it is steep. Outside of the Stern layer is the Gouy layer which is composed of a variable-density, diffuse cloud of charges, predominantly positive near the particle and equally positive and negative at some distance from the particle. It is the potential gradient across this Gouy layer which is referred to as the zeta potential; and it is this potential

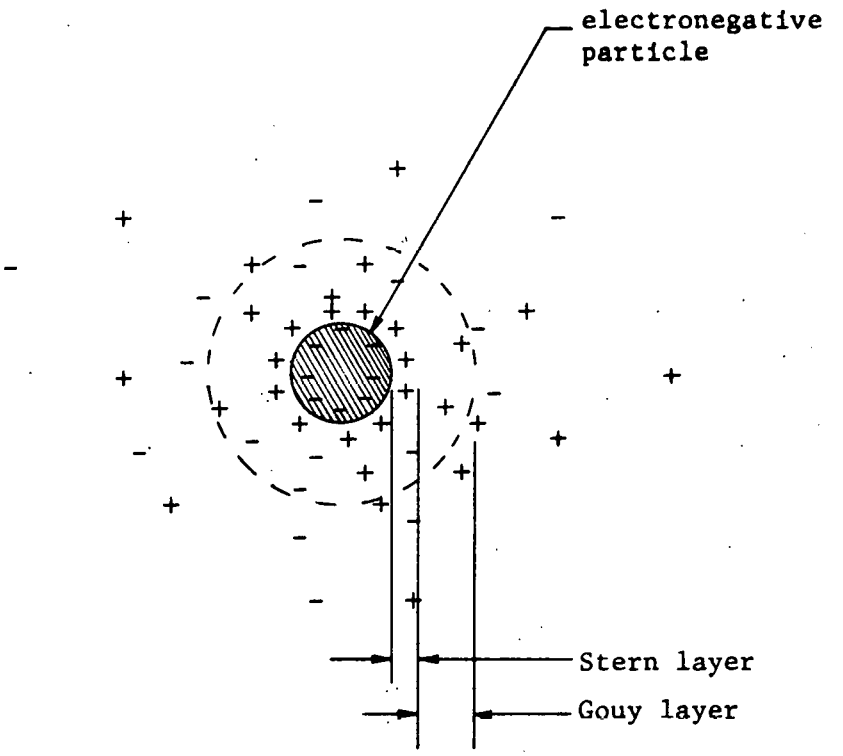

Figure 2. Diffuse double layer of ions about a particle (81).

which causes particles to move toward the pole of opposite charge when placed in an electric field. In terms of other quantities, the zeta potential is given as

$$\text{Zeta potential} = \mu_e(4\pi\nu/\varepsilon) \tag{8}$$

where μ_e is the experimentally determined electrophoretic velocity, ν is the kinematic viscosity of the medium, and ε is the dielectric constant.

The thickness of these ion layers varies inversely with the concentration and valence of nonspecific electrolytes and so coagulation can be promoted by increasing the electrolyte concentration, which decreases the zeta potential, and permits the particles to approach one another sufficiently close for van der Waals forces to become effective. The ion valence is also very important, with a bivalent ion being 50 to 60 times more effective than a monovalent one, and a trivalent ion being 700 to 1000 times as effective (81).

Coagulation can also be induced by reagents such as surfactants, colloids, and polymers. Surfactants are water-soluble compounds that change interfacial conditions by adhering to the surface of the particles. This gives the particles a hydrophobic layer causing them to reject water and to associate with one another.

The addition of colloids having a charge opposite to that of the particles in suspension may also cause coagulation. This is the effect of overall zeta potential reduction and is usually used as a preconditioning step rather than a final one (81).

Finally, coagulation can be induced by the addition of

polyelectrolytes to a colloidal suspension and then altering the pH of the solution (81). It is thought that as the pH of the solution is changed more and more portions of the molecule dissociate from points on the polymer chain, leaving like charges which cause the chain to uncoil. Reversing the process causes the long-chained molecules to draw back together, thereby inducing coagulation. This is apparently the result of portions of the molecule re-associating and thus eliminating the points of like charge.

Very little work has been done in the area of continuous coagulation. Most studies have been concerned with batch coagulation of aerosols using particle diffusion theory and, in some cases, turbulent flow (36,56,59,60,76,85). Some of the results from coagulation studies have shown that coagulation of an initially heterogeneous particle size distribution proceeds at a faster rate (59,60) and results in a denser particle structure (56) than would be obtained from an initially homogeneous particle size distribution. The coagulation rate also appears to depend more on particle concentration than on agitation (36,60,81), although increasing the amount of agitation will increase the coagulation rate up to the point where particle breakup begins.

Most of the theory of coagulation is based upon : (1) Fick's diffusion equation representing the rate controlling process, (2) the assumption that every collision between particles leads to permanent contact, (3) that all particles are of identical size, (4) that the volume of the dispersed phase is negligibly small, and (5) that a

stationary concentration gradient exists near the particles (44,79,81,105). The rate of particulate removal is then given by

$$\frac{dN}{dt} = -4\pi rDN^2 \tag{9}$$

where N is the total number of particles present, r is the radius of the particles, and D is the diffusion coefficient (81). In its integrated form, Equation (9) is,

$$N(t) = \frac{N_o}{1 + 4\pi rDN_o t} \tag{10}$$

where N_o is the initial number of particles present at t=0.

The diffusion coefficient is defined as

$$D = \frac{RT}{6\pi\nu rN_A} \tag{11}$$

where R is the gas constant, T is the absolute temperature, and N_A is Avogadro's number. Applying this definition to Equation (10) yields

$$N(t) = \frac{N_o}{1 + kN_o t} \tag{12}$$

where the coagulation constant, k, has the value $2RT/3\nu N_A$. This equation is sometimes written in the form,

$$N(t) = \frac{N_o}{1 + t/T_{\frac{1}{2}}} \tag{13}$$

where $T_{\frac{1}{2}}$ is defined as the coagulation half-time and has the value of $1/kN_o$.

The coagulation rate given by Equation (9) shows that the particle number density is very critical in determining the coagulation rate. In fact, it has been reported (105) that from theoretical considerations of both number density and surface charge the rate of coagulation approaches zero when the number density is less than

10^6 particles/ml, even if the surface charge is zero. It is for this reason that uninduced coagulation is usually not present unless the high nucleation rate characteristic of homogeneous nucleation is present.

The relationship of the precipitate morphology to the supersaturation and interfacial energy has been reported by Walton (105) and is shown in Table 3. Without the addition of specific coagulation aids or retardants, the morphology of the precipitate will depend upon the chemical reaction under consideration. As previously mentioned, it will be assumed that both primary and secondary coagulation may occur, and therefore both will be included in the particle size distribution model of a continuous MSMPR precipitator. Even though the coagulating particles are not of uniform size, it will be assumed that it is possible to represent the coagulation rates with average coagulation constants. This is a reasonable assumption since the primary effect of nonuniform particles is an increase in the coagulation rate over that for uniform particles. It will also be assumed that the particles can be described by one characteristic dimension which will be taken as the volume-equivalent-diameter. This is the diameter that a spherical, solid, particle would have if its volume equalled that of the particle under consideration.

The application of population balances to a continuous MSMPR precipitator will involve the following assumptions:

1) no particles in the feed solutions

Table 3. Dependence of precipitate morphology upon the supersaturation and interfacial energy (105)

Initial supersaturation ratio	Interfacial energy	Nucleation	Growth	Morphology
1-2	High	None	None	-
	Low	Heterogeneous	Slow-predom. screw disloc.	Discrete, well-formed crystals, no agglomeration
2-5	High	Heterogeneous	Slow-predom. surface nucl.	Discrete, well-formed crystals, no agglomeration
	Low	Heterogeneous	Dentritic	Poorly formed or dendritic crystals, no agglomeration
10-50	High	Heterogeneous	Dendritic	Poorly formed or dendritic crystals, no agglomeration
	Low	Homogeneous	-	Stability dependent, agglomeration evident
> 1000	High	Homogeneous	-	Stability dependent, agglomeration evident
	Low	Homogeneous	-	Colloidal

2) perfect mixing

3) no product withdrawal classification

4) negligible particle breakage and attrition

5) uniform shape factors

6) constant suspension holdup volume

The population density for any type of particle can be defined as

$$\lim_{\Delta L \to 0} \frac{\Delta N'}{\Delta L} = \frac{dN'}{dL} \equiv n(L) \tag{14}$$

where N' is the number of particles in the size range ΔL, (L_1 to L_2), per unit volume of suspension. The total number of particles of any one type in this size range is then given by

$$\Delta N' = \int_{L_1}^{L_2} n(L)dL \tag{15}$$

and the total number of particles of any one type in all size ranges is then given by

$$N_T' = \int_0^{\infty} n(L)dL \tag{16}$$

Crystallite Population Balance

If one considers a constant suspension volume V and a time interval Δt, then the dynamic crystallite population balance (accumulation = input - output) for an arbitrary size range L_1 to L_2 is,

accumulation = (crystallites growing into size range ΔL) -

(crystallites in size range ΔL flowing out of reactor) -

(crystallites growing out of size range ΔL) - (crystallites in size range ΔL which coagulate into clusters) - (crystallites in size range ΔL which coagulate with agglomerates).

This can be written as

$$V \Delta n_x \Delta L = (n_{1,x} G_{1,x} \Delta t\, V) - (Q \bar{n}_x \Delta t\, \Delta L) - (n_{2,x} G_{2,x} \Delta t\, V) - (\bar{n}_x k'_x \Delta t\, \Delta L\, V) - (\bar{n}_x k''_x \Delta t\, \Delta L\, V) \tag{17}$$

where $\bar{n}_x$ is the average crystallite population density in the size range ΔL, G is the growth rate, Q is the total feed flow rate or output flow rate, k'_x is the average coagulation constant for crystallites coagulating into clusters, and k''_x is the average coagulation constant for crystallites coagulating with agglomerates.

Equation (17) can be rearranged and divided by $V\, \Delta t\, \Delta L$.

$$\frac{\Delta n_x}{\Delta t} + \frac{1}{\tau} \bar{n}_x + (n_{2,x} G_{2,x} - n_{1,x} G_{1,x})/\Delta L + (k'_x + k''_x)\bar{n}_x = 0 \tag{18}$$

where τ is defined as the residence time of the process, V/Q. Allowing ΔL and Δt to approach zero yields,

$$\frac{\partial n_x}{\partial t} + \frac{\partial (G_x n_x)}{\partial L} + \left(\frac{1}{\tau} + k'_x + k''_x\right) n_x = 0 \tag{19}$$

Now if one assumes that McCabe's ΔL law is valid ($G \neq f(L)$), then

$$\frac{\partial n_x}{\partial t} + G_x \left(\frac{\partial n_x}{\partial L}\right) + \left(\frac{1}{\tau} + k'_x + k''_x\right) n_x = 0 \tag{20}$$

Equation (20) represents the dynamic crystallite population balance for the continuous MSMPR precipitator. If steady state is assumed, this reduces to

$$G_x \left(\frac{dn_x}{dL}\right) + \left(\frac{1}{\tau} + k'_x + k''_x\right) n_x = 0 \tag{21}$$

This equation has a steady state solution given by

$$n_x = n_x^o \exp\ (-L/G_{e,x}\tau) \tag{22}$$

where n_x^o is defined as the nucleate population density of embryo-size crystals, and $G_{e,x}$ is the effective crystallite growth rate defined as

$$G_{e,x} \equiv \frac{G_x}{1 + \tau(k_x' + k_x'')} \tag{23}$$

Cluster Population Balance

A dynamic population balance for the clusters can be derived in a similar manner as that for the crystallites, by assuming that the cluster growth due to coagulation can be represented by an average growth rate, G_c, defined as

$$G_c \equiv k_x' \bar{L}_x \tag{24}$$

where $\bar{L}_x$ is the average crystallite size. The cluster population balance (accumulation - input - output) is then given as,

accumulation = (clusters growing into size range ΔL by coagulation of crystallites) + (clusters growing into size range ΔL by crystal growth) - (clusters in size range ΔL flowing out of reactor) - (clusters growing out of size range ΔL by coagulation with crystallites) - (clusters growing out of size range ΔL by crystal growth) - (clusters leaving size range ΔL by coagulation with clusters into agglomerates).

This dynamic balance can also be written as

$$V \Delta n_c \Delta L = (n_{1,c} G_{1,c} \Delta t V) + (n_{1,c} G_{1,x} \Delta t V) - (Q \bar{n}_c \Delta t \Delta L) - (n_{2,c} G_{2,c} \Delta t V) - (n_{2,c} G_{2,x} \Delta t V) - (\bar{n}_c k_c \Delta t \Delta L V) \quad (25)$$

where k_c is the average coagulation constant of clusters into agglomerates. It can be shown that, if G_c and G_x are assumed to be size independent, then in the limit as Δt and ΔL approach zero, Equation (25) reduces to

$$\frac{\partial n_c}{\partial t} + (G_c + G_x) \frac{\partial n_c}{\partial L} + \left(\frac{1}{\tau} + k_c\right) n_c = 0 \quad (26)$$

Equation (26) represents the cluster dynamic population, and at steady state reduces to

$$(G_c + G_x) \frac{dn_c}{dL} + \left(\frac{1}{\tau} + k_c\right) n_c = 0 \quad (27)$$

The steady state solution is

$$n_c = n_c^o \exp(-L/\tau G_{e,c}) \quad (28)$$

where n_c^o is the extrapolated cluster nucleate population density and $G_{e,c}$ is the cluster effective growth rate defined as

$$G_{e,c} \equiv \frac{G_c + G_x}{1 + \tau k_c} \quad (29)$$

Agglomerate Population Balance

If one assumes that; (1) the agglomerate growth rate as a result of the coagulation of clusters can be described as an average coagulation growth rate, G_a, defined as

$$G_a \equiv k_c \bar{L}_c \quad (30)$$

where $\bar{L}_c$ is the average cluster size, and (2) that the agglomerate

growth rate as a result of the coagulation of crystallites with agglomerates can be described as an average coagulation growth rate, G_a', defined as,

$$G_a' \equiv k_x'' \bar{L}_x \tag{31}$$

then a dynamic agglomerate population balance (accumulation = input - output) can be written.

accumulation = (agglomerates growing into size range ΔL as a result of coagulation of clusters) + (agglomerates growing into size range ΔL as a result of coagulation of crystallites with agglomerates) + (agglomerates growing into size range ΔL through crystal growth) - (agglomerates growing out of size range ΔL by coagulation with clusters) - (agglomerates growing out of size range ΔL by coagulation with crystallites) - (agglomerates in size range ΔL flowing out of reactor) - (agglomerates growing out of size range ΔL by crystal growth).

This can also be expressed by

$$V \Delta n_a \Delta L = (n_{1,a} G_{1,a} \Delta t\, V) + (n_{1,a} G_{1,a}' \Delta t\, V) + (n_{1,a} G_{1,x} \Delta t\, V) - (n_{2,a} G_{2,a} \Delta t\, V) - (n_{2,a} G_{2,a}' \Delta t\, V) - (Q \bar{n}_a \Delta t\, \Delta L) - (n_{2,a} G_{2,x} \Delta t\, V) \tag{32}$$

Equation (32) can be rearranged, divided by $V\, \Delta t\, \Delta L$, and, in the limit as Δt and ΔL approach zero, shown to yield

$$\frac{\partial n_a}{\partial t} + \frac{\partial (n_a G_a)}{\partial L} + \frac{\partial (n_a G_a')}{\partial L} + \frac{\partial (n_a G_x)}{\partial L} + \frac{1}{\tau} n_a = 0 \tag{33}$$

If G_a, G_a', and G_x are assumed to be size-independent, then Equation (33) can be written as

$$\frac{\partial n_a}{\partial t} + (G_a + G_a' + G_x) \frac{\partial n_a}{\partial L} + \frac{1}{\tau} n_a = 0 \tag{34}$$

Under steady state operating conditions the dynamic agglomerate population balance, as expressed by Equation (34), reduces to

$$(G_a + G_a' + G_x) \frac{dn_a}{dL} + \frac{1}{\tau} n_a = 0 \tag{35}$$

The steady state solution to Equation (35) is

$$n_a = n_a^o \exp(-L/\tau G_{e,a}) \tag{36}$$

where n_a^o is the extrapolated agglomerate nucleate population density, and $G_{e,a}$ is the effective agglomerate growth rate defined as

$$G_{e,a} \equiv G_a + G_a' + G_x \tag{37}$$

The steady state solutions describing the population density distributions of the clusters and agglomerates (Equations (28) and (36) assume that the population densities are continuous in the size range 0 to ∞, however in reality the average minimum size of the clusters and agglomerates will not be zero. The average minimum cluster size, $\bar{L}_{m,c}$, will depend upon the average crystallite size as given by

$$\bar{L}_{m,c} = 2\bar{L}_x \tag{38}$$

where $\bar{L}_x$ is the average crystallite size calculated by

$$\bar{L}_x = \frac{\int_0^\infty L n_x^o \exp(-L/\tau G_{e,x}) dL}{\int_0^\infty n_x^o \exp(-L/\tau G_{e,x}) dL} = G_{e,x}\tau \tag{39}$$

The average minimum size of the agglomerates will depend upon the

average minimum size of the clusters, the average minimum size of the crystallites, and upon the coagulation ratio of the crystallites with agglomerates and clusters to agglomerates.

$$\bar{L}_{m,a} = 2\bar{L}_c + (k''_x/k_c)\bar{L}_x \tag{40}$$

The average nucleate population density, $\bar{n}^o$, for the clusters and agglomerates can be calculated by evaluating Equation (28) and (36) at their respective average minimum particle size,

$$\bar{n}^o_c = n^o_c \exp(-\bar{L}_{m,c}/\tau G_{e,c}) \tag{41}$$

$$\bar{n}^o_a = n^o_a \exp(-\bar{L}_{m,a}/\tau G_{e,a}) \tag{42}$$

Overall Population Balance

The total particle population distribution, $n_T(L)$, leaving the steady state MSMPR precipitator is the sum of that of the crystallites, clusters, and agglomerates as given by

$$n_T(L) = n_x(L) + n_c(L) + n_a(L) \tag{43}$$

or

$$n_T(L) = n^o_x \exp(-L/\tau G_{e,x}) + n^o_c \exp(-L/\tau G_{e,c}) + n^o_a \exp(-L/\tau G_{e,a}) \tag{44}$$

where it is understood that the clusters do not exist at a size below $\bar{L}_{m,c}$, and that the agglomerates do not exist at a size below $\bar{L}_{m,a}$.

Equation (44) indicates that if the total particle population distribution from a continuous MSMPR precipitator operating at steady state is plotted on a semi-log paper as a function of particle size, then a curve representing the sum of three exponentials will be obtained. If the growth rates are significantly different from

one another, then this curve can be resolved into three straight lines in a manner similar to that for multicomponent radioactive decay analysis. Each line will represent one of the particle distributions with an intercept equal to log n^o and a slope equal to $-1/2.303G\tau$.

The total number of particles present per unit volume of suspension, N_T, is the sum, over all particle sizes, of the crystallites, clusters, and agglomerates.

$$N_T = N_x + N_c + N_a \tag{45}$$

where N_x, N_c, and N_a represent the total number densities of crystallites, clusters, and agglomerates, respectively.

$$N_x = \int_0^\infty n_x^o \exp(-L/\tau G_{e,x})\, dL = n_x^o \tau G_{e,x} \tag{46}$$

$$N_c = \int_{\bar{L}_{m,c}}^\infty n_c^o \exp(-L/\tau G_{e,c})\, dL = \bar{n}_c^o \tau G_{e,c} \tag{47}$$

$$N_a = \int_{\bar{L}_{m,a}}^\infty n_a^o \exp(-L/\tau G_{e,a})\, dL = \bar{n}_a^o \tau G_{e,a} \tag{48}$$

In addition to knowing the steady state population density distribution of the crystallites, clusters, and agglomerates, one would also like to know, (1) their respective average particle size, (2) their respective dominant particle size (that particle size associated with the largest weight fraction), and (3) their respective fraction of the total suspension density.

The average particle size of the crystallites was determined

previously and is given by Equation (39). The average particle size of the clusters, $\bar{L}_c$, is,

$$\bar{L}_c = \frac{\int_{\bar{L}_{m,c}}^{\infty} Ln_c^o \exp(-L/\tau G_{e,c})dL}{\int_{\bar{L}_{m,c}}^{\infty} n_c^o \exp(-L/\tau G_{e,c})dL} \tag{49}$$

or

$$\bar{L}_c = \tau G_{e,c} + \bar{L}_{m,c} \tag{50}$$

The average particle size of the agglomerates is given by

$$\bar{L}_a = \frac{\int_{\bar{L}_{m,a}}^{\infty} Ln_a^o \exp(-L/\tau G_{e,a})dL}{\int_{\bar{L}_{m,a}}^{\infty} n_a^o \exp(-L/\tau G_{e,a})dL} \tag{51}$$

and reduces to

$$\bar{L}_a = \tau G_{e,a} + \bar{L}_{m,a} \tag{52}$$

The suspension density, M, for any given type of particle can be calculated as

$$M = k_v \rho \int_{(0 \text{ or } \bar{L}_m)}^{\infty} L^3 n^o \exp(-L/\tau G_e)dL \tag{53}$$

where k_v is the size-independent volumetric shape factor and ρ is the density. Application of Equation (53) to the population density distributions of the crystallites, clusters, and agglomerates yields

$$M_x = 6\rho_x k_{v,x} n_x^o (G_{e,x}\tau)^4 \tag{54}$$

$$M_c = \rho_c k_{v,c} \overline{n^o_c} \left[\overline{L}_{m,c} G_{e,c} \tau + 3\overline{L}_{m,c} (G_{e,c}\tau)^2 + 6\overline{L}_{m,c} (G_{e,c}\tau)^3 + 6(G_{e,c}\tau)^4 \right] \quad (55)$$

$$M_a = \rho_a k_{v,a} \overline{n^o_a} \left[\overline{L}_{m,a} G_{e,a} \tau + 3\overline{L}_{m,a} (G_{e,a}\tau)^2 + 6\overline{L}_{m,a} (G_{e,c}\tau)^3 + 6(G_{e,c}\tau)^4 \right] \quad (56)$$

where M_x, M_c, and M_a are the crystallite, cluster, and agglomerate suspension densities respectively. The total suspension density is then given by

$$M_T = M_x + M_c + M_a \quad (57)$$

The suspension density fractions for the different types of particle can be calculated as

$$M_{F,x} = \frac{M_x}{M_T} \quad (58)$$

$$M_{F,c} = \frac{M_c}{M_T} \quad (59)$$

$$M_{F,a} = \frac{M_a}{M_T} \quad (60)$$

where $M_{F,x}$, $M_{F,c}$, and $M_{F,a}$ are the respective crystallite, cluster and agglomerate suspension density fractions.

The dominant particle size is that particle size which is associated with the peak in the mass fraction distribution. It can be obtained by developing the expression for the mass fraction distribution, differentiating with respect to particle size, and then setting resulting expression equal to zero.

The mass of each particle, m_p, is given by

$$m_p = \rho k_v L^3 \quad (61)$$

The mass per unit volume of suspension of all particles of size L is then given as

$$M(L) = \rho k_v L^3 n(L) \tag{62}$$

The mass fraction of all particles of size L is represented by the ratio of m(L) to the suspension density, M, and is given by

$$W(L) = \frac{m(L)}{M} \tag{63}$$

where W(L) is defined as the mass fraction.

The particle size distribution from a continuous MSMPR precipitator has been shown to consist of three types of particles, each of whose population density distribution can be represented by an exponential of the form

$$n(L) = n^o \exp(-L/G_e\tau) \tag{64}$$

It is evident that the weight fraction distribution, w(L), for a particular type of particle can be expressed as

$$w(L) = \frac{\rho k_v L^3 n^o \exp(-L/\tau G_e)}{M} \tag{65}$$

The respective terms for the crystallites, clusters, and agglomerates can be substituted into Equation (65), yielding three equations which can be differentiated, set equal to zero, and solved for their respective dominant particle size. The results from such a procedure are shown below.

$$L_{d,x} = 3\tau G_{e,x} \tag{66}$$

$$L_{d,c} = 3\tau G_{e,c} + \bar{L}_{m,c} \tag{67}$$

$$L_{d,a} = 3\tau G_{e,a} + \bar{L}_{m,a} \tag{68}$$

where L_d is defined as the dominant particle size.

The previously discussed relationships have shown that the effective growth rates of the crystallites, clusters, and agglomerates are very interrelated. In fact, the effective growth rates of the clusters and agglomerates can be written in terms consisting only of the crystal growth rate, residence time, and average coagulation constants, as was done for the effective crystallite growth rate expressed in Equation (23). Substitutions of the appropriate relationships discussed above into Equations (29) and (37) yields

$$G_{e,c} = G_x \left[\frac{1}{1 + \tau k_c} + \frac{\tau k_x'}{1 + \tau(k_x' + k_x'' + k_c) + \tau^2(k_c k_x'' + k_c k_x')} \right] \tag{69}$$

and

$$G_{e,a} = G_x \left[1 + \frac{\tau k_c}{1 + \tau k_c} + \frac{\tau(2k_c + k_x'')}{1 + \tau(k_x' + k_x'')} + \frac{\tau^2 k_c k_x'}{1 + \tau(k_x' + k_x'' + k_c) + \tau^2(k_c k_x' + k_c k_x'')} \right] \tag{70}$$

It is necessary at this point to consider nucleation rates because they, in conjunction with the effective growth rates, will determine the average particle sizes, the dominant particle sizes, and the suspension density fractions. The crystallite nucleation rate, B_x^o, can be defined as

$$B_x^o = \frac{dN_x^o}{dt} = \left.\frac{dN_x}{dt}\right|_{L=0} = \left.\frac{dN_x}{dL}\right|_{L=0} \cdot \frac{dL}{dt} \tag{71}$$

or

$$B_x^o = n_x^o G_{e,x} \tag{72}$$

where the crystal nucleate population density, n_x^o, is defined as $(dN_x/dL)\big|_{L=0}$, and the effective crystal growth rate is defined as dL/dt. If the growth rate is assumed to be a linear function of supersaturation, then Equation (4), (7), and (72) can be combined to yield

$$B_x^o = k_{N,x}(G_{e,x})^{i_x}(M_T)^{j_x} \tag{73}$$

and

$$n_x^o = k_{N,x}(G_{e,x})^{i_x-1}(M_T)^{j_x} \tag{74}$$

where $k_{N,x}$ is defined as the crystallite nucleation constant, and i_x is the crystallite growth rate kinetic order of nucleation, and j_x is the crystallite suspension density kinetic order of nucleation.

Equation (74) implies that if the MSMPR precipitator is operated at different levels of supersaturation, then the growth rate kinetic order of nucleation can be obtained. This can be accomplished by operating at the same suspension density for different residence times. Conservation of mass requires that the shorter holding times must produce higher growth rates and, thus higher supersaturations. If the solubility and coagulation rates of the precipitate can be varied through changes in pH, then operation of the precipitator at constant suspension densities, constant residence times and different pH's should also allow the determination of the crystallite kinetic order of nucleation. Subsequent operation of the precipitator for different suspension densities will allow determination of the suspension density kinetic order of nucleation, j_x, and the nucleation constant, $k_{N,x}$.

The nucleation rates of the clusters and agglomerates will depend upon the coagulation constants, as do their growth rates. It seems

appropriate, therefore, to base the nucleation rate models of the clusters and agglomerates on a power function of their respective effective growth rates and suspension densities in a manner similar to that of the crystallites. This results in the following nucleation rate models for the clusters and agglomerates

$$B_c^o = k_{N,c}(G_{e,c})^{i_c}(M_T)^{j_c} \tag{75}$$

$$B_a^o = k_{N,a}(G_{e,a})^{i_a}(M_T)^{j_a} \tag{76}$$

The cluster and agglomerate nucleation rates can also be expressed as

$$B_c^o = \left.\frac{dN_c}{dt}\right|_{L=0} = \left.\frac{dN_c}{dL}\right|_{L=0} \cdot \frac{dL}{dt} \tag{77}$$

$$B_a^o = \left.\frac{dN_a}{dt}\right|_{L=0} = \left.\frac{dN_a}{dL}\right|_{L=0} \cdot \frac{dL}{dt} \tag{78}$$

or

$$B^o = n_c^o G_{e,c} \tag{79}$$

$$B_a^o = n_a^o G_{e,a} \tag{80}$$

where $(dN/dL)\big|_{L=0}$ is defined as the extrapolated nucleate population density, and dL/dt is defined as the effective growth rate. Application of Equation (79) and (80) to Equation (75) and (76), respectively, yields

$$n_c^o = k_{N,c}(G_{e,c})^{i_c-1}(M_T)^{j_c} \tag{81}$$

$$n_a^o = k_{N,a}(G_{e,a})^{i_a-1}(M_T)^{j_a} \tag{82}$$

Note that Equations (77) through (82) are based upon minimum particle sizes being zero. The average nucleate population densities of the clusters and agglomerates, taking into account the average minimum particle sizes, will be given by combining Equations (41) and (42) with Equations (81) and (82), respectively.

$$\overline{n}_c^o = k_{N,c}(G_{e,c})^{i_c-1}(M_T)^{j_c} \exp(-\overline{L}_{m,c}/\tau G_{e,c}) \tag{83}$$

$$\overline{n}_a^o = k_{N,a}(G_{e,a})^{i_a-1}(M_T)^{j_a} \exp(-\overline{L}_{m,a}/\tau G_{e,a}) \tag{84}$$

The nucleation rates of the average minimum sized particles can be written as

$$\overline{B}_c^o = \overline{n}_c^o \, G_{e,c} \exp(\overline{L}_{m,c}/\tau G_{e,c}) \tag{85}$$

$$\overline{B}_a^o = \overline{n}_a^o \, G_{e,a} \exp(\overline{L}_{m,a}/\tau G_{e,a}) \tag{86}$$

where $\overline{B}_c^o$ and $\overline{B}_a^o$ are the average cluster and agglomerate nucleation rates, respectively. For the case when average minimum cluster and agglomerate sizes are close to zero, Equation (83) to (86) may be replaced by Equations (79) to (82).

Equations (81) and (82) indicate that if the continuous MSMPR precipitator is operated at different degrees of coagulation for a constant suspension density and residence time, the kinetic order of the clusters, i_c, and agglomerates, i_a, can be obtained. If the precipitator is then operated at different suspension densities, the kinetic orders j_c and j_a, and the nucleation constants $k_{N,c}$ and $k_{N,a}$ can be determined.

The effect of dynamic flow rates on the total solids concentration can be examined by considering an overall dynamic mass balance

(accumulation = input - output). If one assumes a constant holdup volume V, then the dynamic mass balance is given by

$$V \frac{d}{dt}(M_T + C) = QP - QC - QM_T \tag{87}$$

where C is the solute concentration and P is the solute production rate. If is evident from Equation (87) that changes in flow will not perturb the solids concentration since all terms on the right hand side are affected uniformly. However, changes in concentrations and solubilities will affect the solids concentration.

It is necessary at this point to develop one final relationship which will place a constraint on the crystal growth rate. If one assumes that the mass rate of phase change due to nucleation is negligible and that the mass accumulation of solute as supersaturation is negligible, then the following solute balance results, (accumulation = input - output - rate of make)

$$0 = QP - QC - V\rho_x k_{a,x} \int_0^\infty (G_x/2) n_x(L) L^2 dL - V\rho_x k_{a,c} \int_{L_{m,c}}^\infty (G_x/2) n_c(L) L^2 dL - V\rho_x k_{a,a} \int_{L_{m,a}}^\infty (G_x/2) n_a(L) L^2 dL \tag{88}$$

where ρ_x is the crystal density and $k_{a,x}$, $k_{a,c}$, and $k_{a,a}$ are the crystallite, cluster, and agglomerate size-independent surface area shape factors, respectively. If the crystal growth rate is size-independent, then Equation (88) can be rearranged to

$$G_x = \frac{2(P - C)}{\rho_x \tau A_T} \tag{89}$$

where A_T is defined as the total particle surface area per unit volume of suspension,

$$A_T = A_x + A_c + A_a \tag{90}$$

where A_x, A_c, and A_a are the total surface areas per unit volume of suspension of the crystallites, clusters, and agglomerates as given below.

$$A_x = k_{a,x} \int_0^\infty n_x(L) L^2 dL \tag{91}$$

$$A_c = k_{a,c} \int_{L_{m,c}}^\infty n_c(L) L^2 dL \tag{92}$$

$$A_a = k_{a,a} \int_{L_{m,a}}^\infty n_a(L) L^2 dL \tag{93}$$

Equation (89) is true regardless of whether flow rates and concentrations are constant, and it provides the feedback between the crystal growth rate and the overall particle size distribution. This provides a large amount of self-regulation of the crystallite size distribution, which will in turn be reflected in the cluster and agglomerate size distributions.

At this point, one may recall that the crystal growth rate is often a linear function of supersaturation, which will be directly proportional to the solute production rate and the solute equilibrium concentration, and inversely proportional to the residence time and the total surface area available for crystal growth,

$$S = \frac{k''(P - C_e)}{\tau A_T} \tag{94}$$

where k'' is a constant.

Equation (89) can now be combined with Equation (94) and (7) to yield

$$G_x = \frac{k^* k''(P - C_e)}{\tau A_T} = \frac{k_1(P - C_e)}{\tau A_T} \tag{95}$$

This equation now places a suitable constraint on the crystal growth rate in terms of known quantities, and allows a model of the continuous MSMPR precipitator to be developed. The informational flow chart from such a model is shown in Figure 3, where it is understood that the various nucleation constants, coagulation constants, and kinetic orders of nucleation are functions of process parameters (reacting feed mole ratios, feed concentrations, suspension density, temperature, agitation, etc.), which can be determined experimentally. The particle densities and shape factors will also have to be determined experimentally, and they might also prove to be functions of the process conditions. Table 4 lists the parameters of the continuous MSMPR model and shows which ones must be determined experimentally and which ones must be calculated.

Figure 3. Informational flow diagram for continuous MSMPR precipitation model

THIS PAGE

WAS INTENTIONALLY

LEFT BLANK

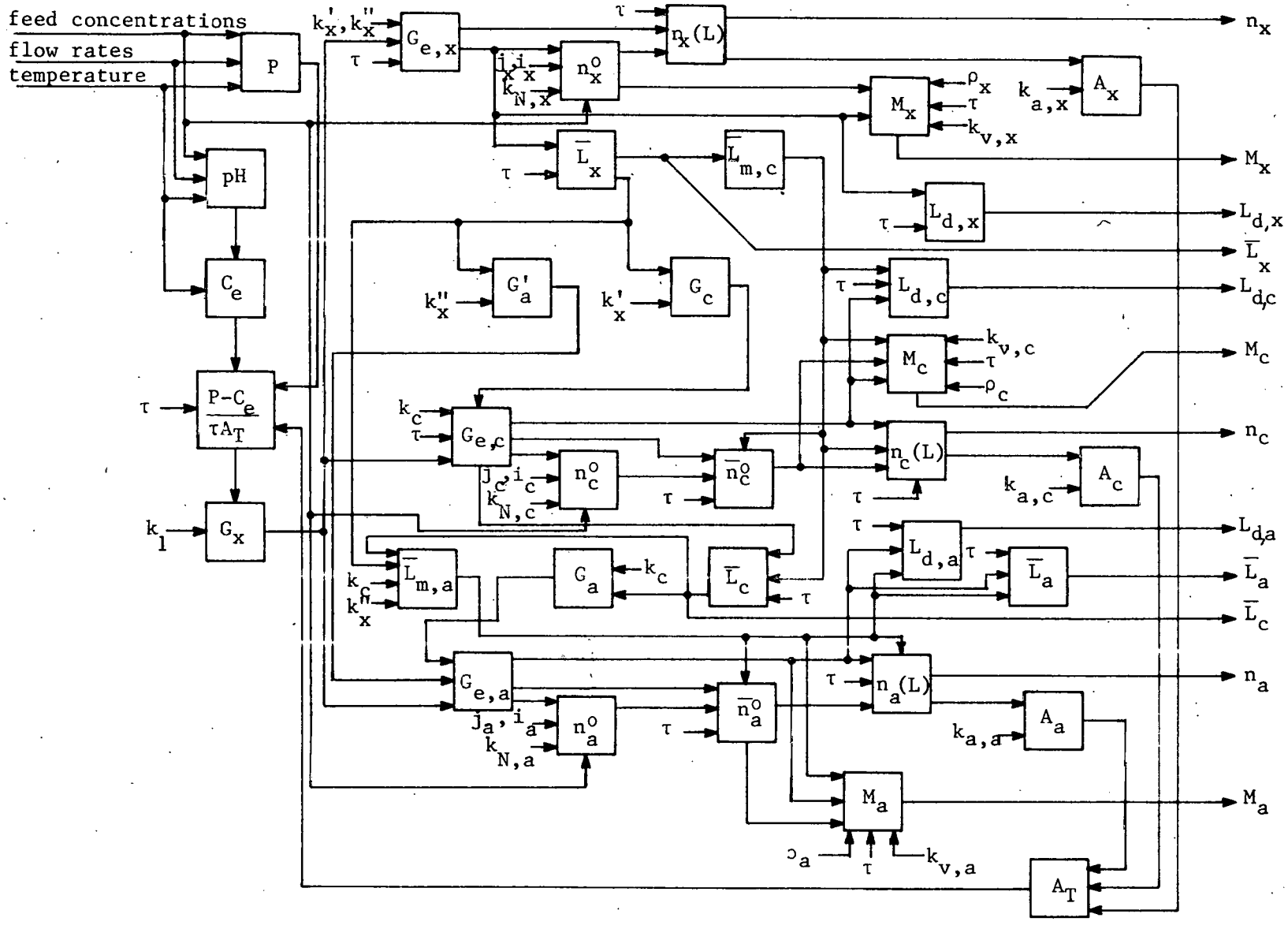
feed concentrations
flow rates
temperature
P
pH
C_e
$\frac{P-C_e}{\tau A_T}$
G_x
$G_{e,x}$
n_x^o
$n_x(L)$
$\bar{L}_x$
$\bar{L}_{m,c}$
M_x
A_x
$L_{d,x}$
G'_a
G_c
$L_{d,c}$
M_c
$G_{e,c}$
n_c^o
$\bar{n}_c^o$
$n_c(L)$
A_c
$\bar{L}_{m,a}$
G_a
$\bar{L}_c$
$L_{d,a}$
$\bar{L}_a$
$G_{e,a}$
n_a^o
$\bar{n}_a^o$
$n_a(L)$
A_a
M_a
A_T
n_x
M_x
$L_{d,x}$
$\bar{L}_x$
$L_{d,c}$
M_c
n_c
$L_{d,a}$
$\bar{L}_a$
$\bar{L}_c$
n_a
M_a

Table 4. Kinetic parameters and process variables included in the continuous MSMPR precipitation model

Variables determined by precipitation conditions	
feed concentrations	
feed flow rates	
temperature	
residence time, τ	
Parameters determined from experimental data	
precipitate production rate	P
precipitation pH	pH
solute equilibrium concentration	C_e
crystal growth rate	G_x
effective growth rates	$G_{e,x}$, $G_{e,c}$, $G_{e,a}$
nucleate population densities	n_x^o, n_c^o, n_a^o
coagulation constants	k_x', k_x'', k_c
growth rate kinetic orders of nucleation	i_x, i_c, i_a
suspension density kinetic orders of nucleation	j_x, j_c, j_a
nucleation constants	$k_{N,x}$, $k_{N,c}$, $k_{N,a}$
particle densities	ρ_x, ρ_c, ρ_a
surface area shape factors	$k_{a,x}$, $k_{a,c}$, $k_{a,a}$
volumetric shape factors	$k_{v,x}$, $k_{v,c}$, $k_{v,a}$

Table 4. (continued)

Parameters calculated from other terms	
crystal growth rate constant	k'
population density distributions	$n_x(L)$, $n_c(L)$, $n_a(L)$
average minimum sizes	$\overline{L}_{m,c}$, $\overline{L}_{m,a}$
average nucleate population densities	$\overline{n}_c^o$, $\overline{n}_a^o$
average particle sizes	$\overline{L}_x$, $\overline{L}_c$, $\overline{L}_a$
agglomerate growth rates	G_a, G_a'
dominant particle sizes	$L_{d,x}$, $L_{d,c}$, $L_{d,a}$
suspension densities	M_x, M_c, M_a
surface areas	A_a, A_c, A_a
total surface area	A_T

EQUIPMENT

The continuous precipitation process flow chart is shown in Figure 4. Ammonium hydroxide and uranyl nitrate feeds are pumped continuously into a precipitation vessel where they are intimately mixed and react. The APU slurry is intermittently pumped from the precipitator into a product storage tank where the precipitate is allowed to settle out. The supernatant liquid is then pumped through an ion-exchange column to remove any residual uranium and the liquid is discarded.

The APU was not reconverted to uranyl nitrate, although it could have been by the addition of nitric acid and water. This would have introduced various amounts of free nitric acid in the uranyl nitrate, which has been reported to affect the surface area of the APU (68).

The design of the MSMPR precipitator followed that of a proven design from which crystal size distribution data conforms to the mixed-suspension, mixed-product removal concept (54). The 2ℓ suspension volume of the precipitator is also within the size ranges of those previously investigated (54,87). The precipitation vessel, shown in Figure 5, consists of a cylindrical borosilicate glass tube with a curved bottom pushed up in its center, forming a conical baffle. A stainless steel draft tube, shown in Figure 6, is supported by four vertical stainless steel baffles and is used to direct the downward flow produced by an impeller. The conical baffle causes an upward flow and the four vertical baffles divide this upward

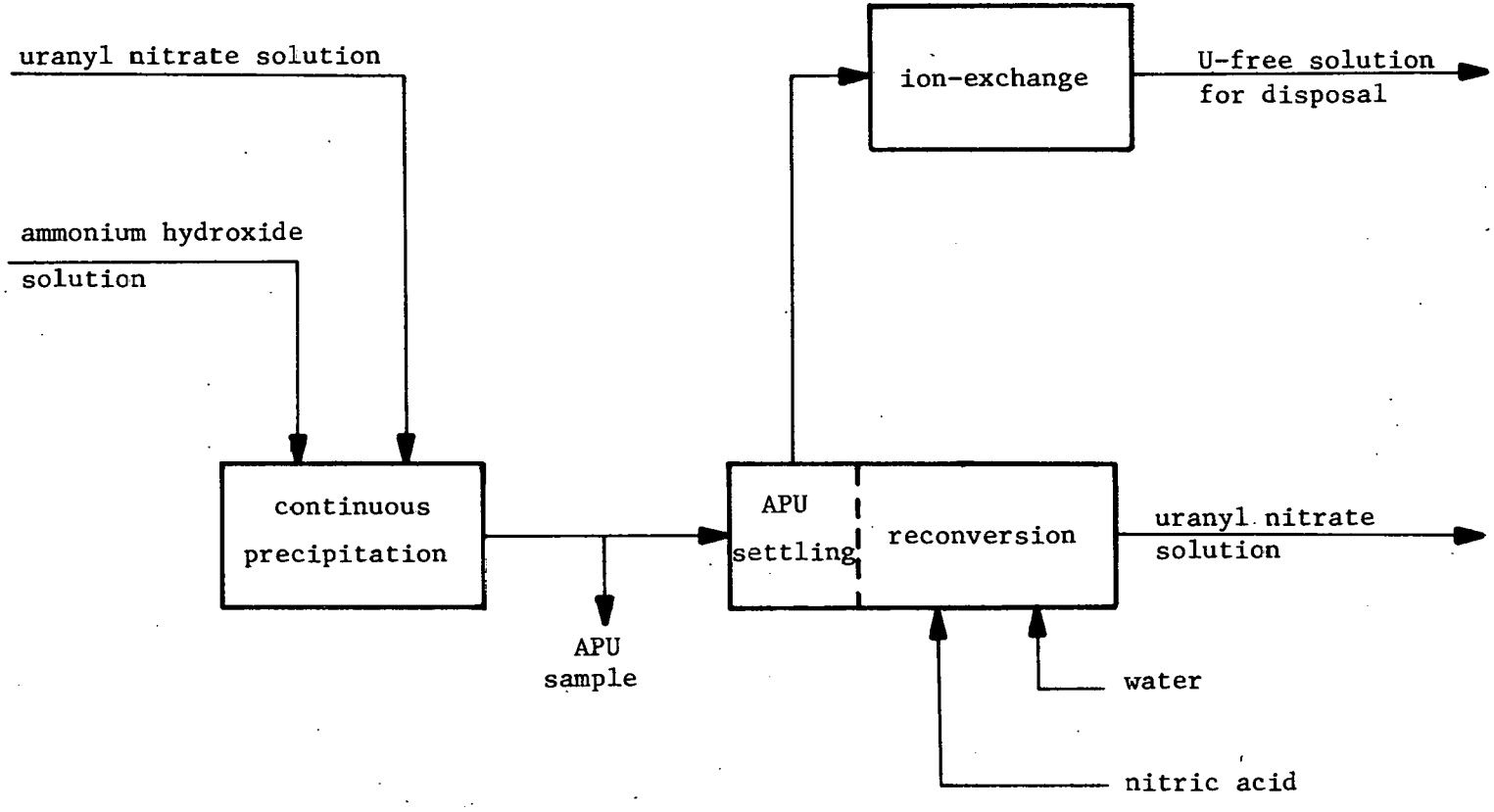

Figure 4. APU precipitation flow chart

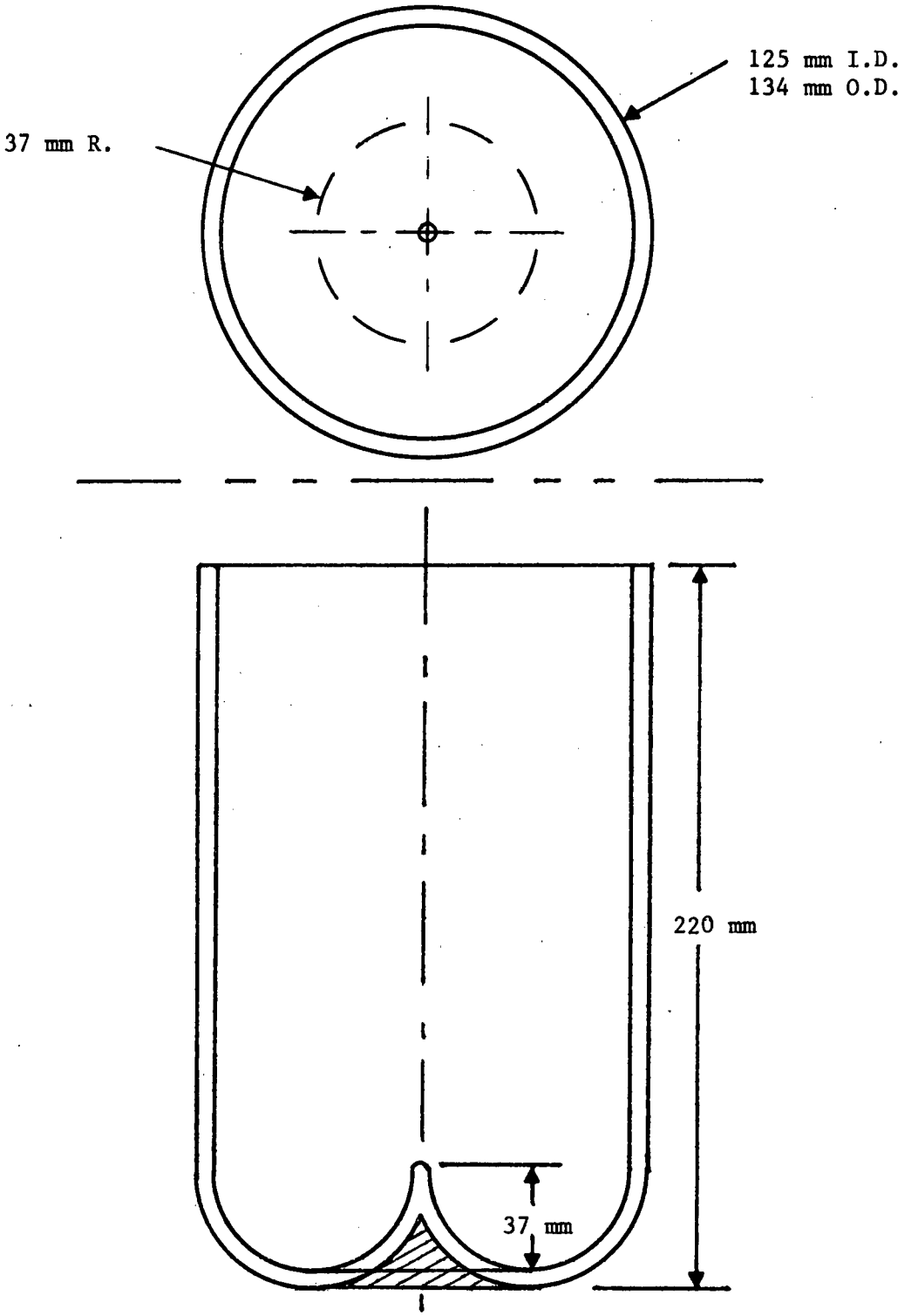

Figure 5. Glass precipitation vessel

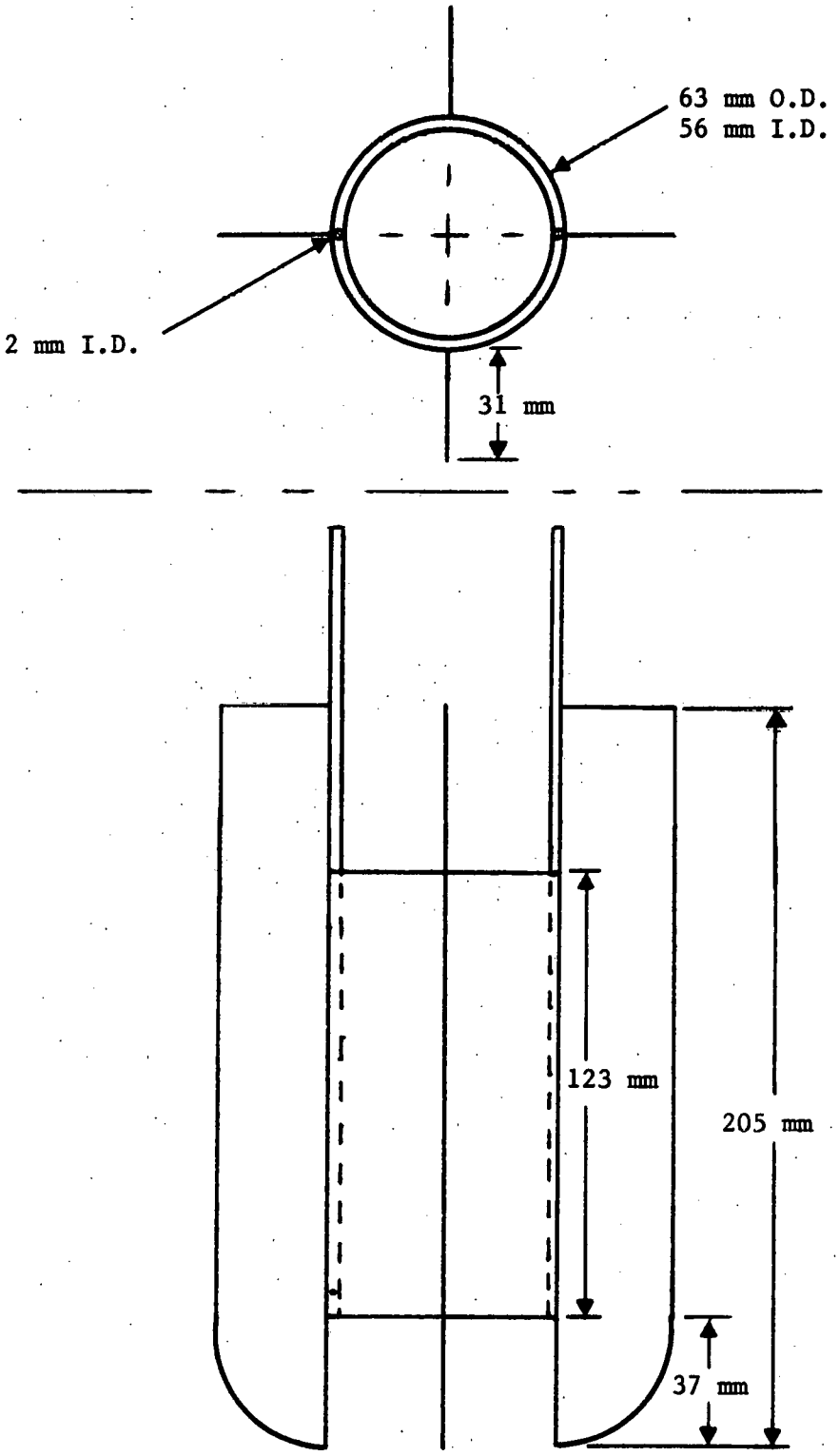

Figure 6. Stainless steel draft tube

flow into four regions, reducing the tendency of the particle suspension to swirl around the annular region. The draft tube is hollow and is provided with inlet and outlet lines so that is may be used for heating or cooling. A diagram of the assembled MSMPR precipitator is shown in Figure 7.

Feed solutions are introduced into the center of the draft tube where rapid dispersion occurs. The position of the product removal tube is near the edge of the glass vessel and at a depth just above the bottom of the draft tube. The correct location to permit isokinetic removal of sample was determined by observing the flow pattern of ion-exchange beads in the reactor and is such that the flow is uniformly vertical. A photograph of the precipitation vessel is shown in Figure 8.

Investigation of current crystallization techniques (54,87) indicated that for the residence times to be considered for this work, continuous preduct removal could involve product removal velocities low enough that product classification might occur. An intermittent product removal system has been used by other investigators to avoid this situation and was also used in this work. This intermittent system is shown in Figure 9 and consists of a relay system activated by a float and sliprod assembly which can be adjusted to maintain the desired suspension volume and intermittent product removal volume.

The equipment flow sheet is shown in Figure 10; however, the intermittent product removal control system, pH instrument, and

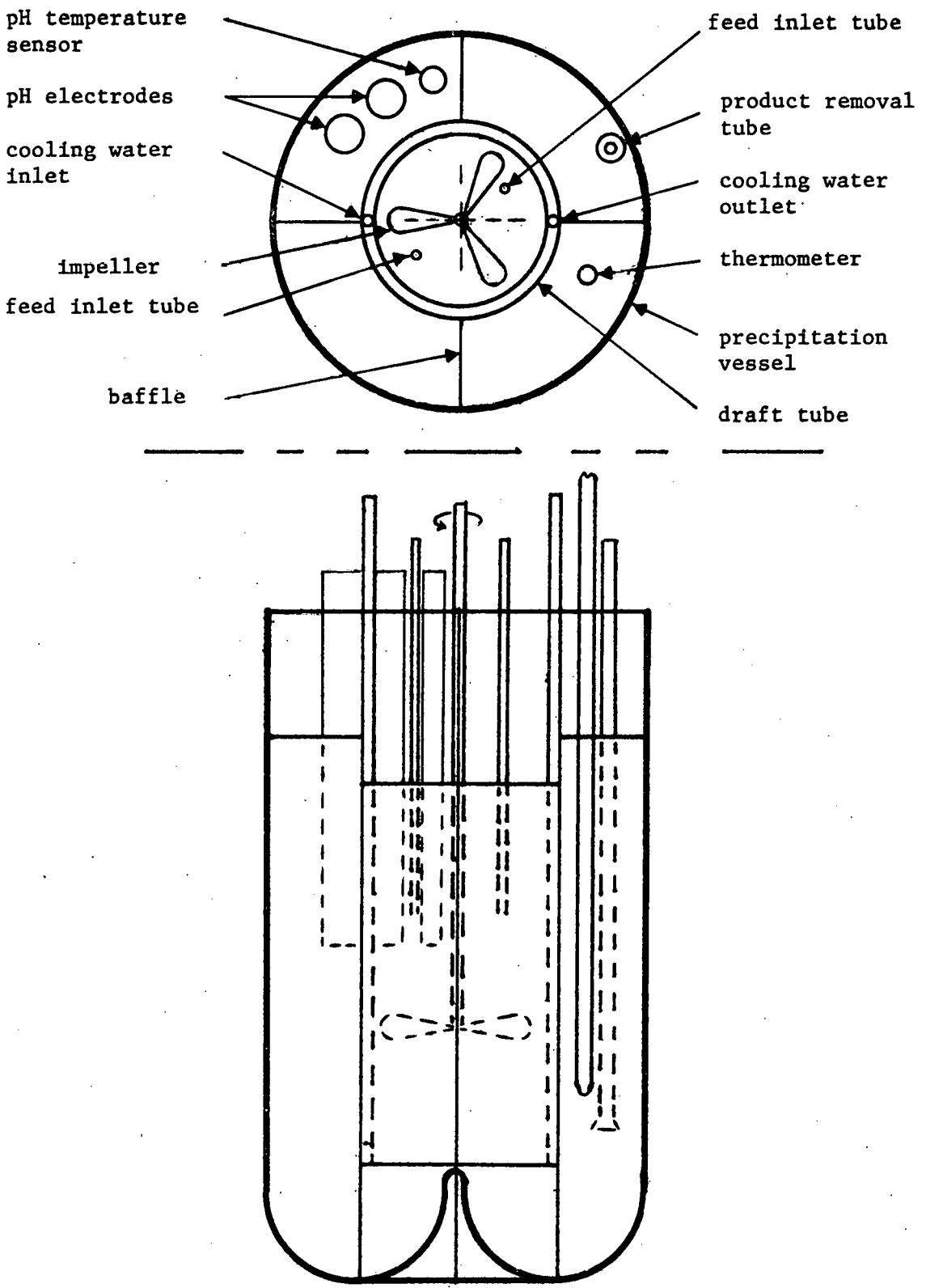

Figure 7. MSMPR precipitation reactor

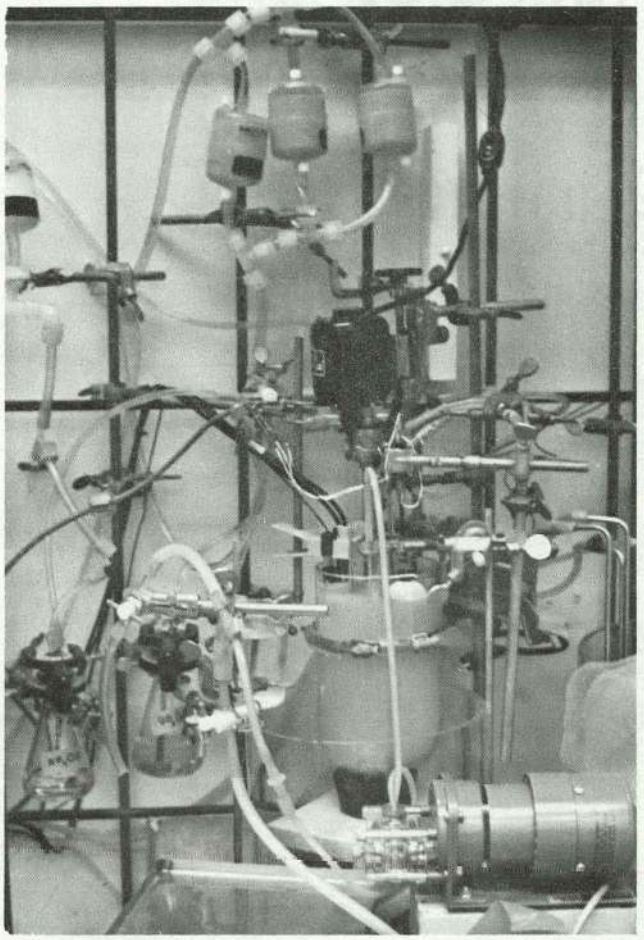

Figure 8. Continuous mixed-suspension, mixed-product-removal precipitator.

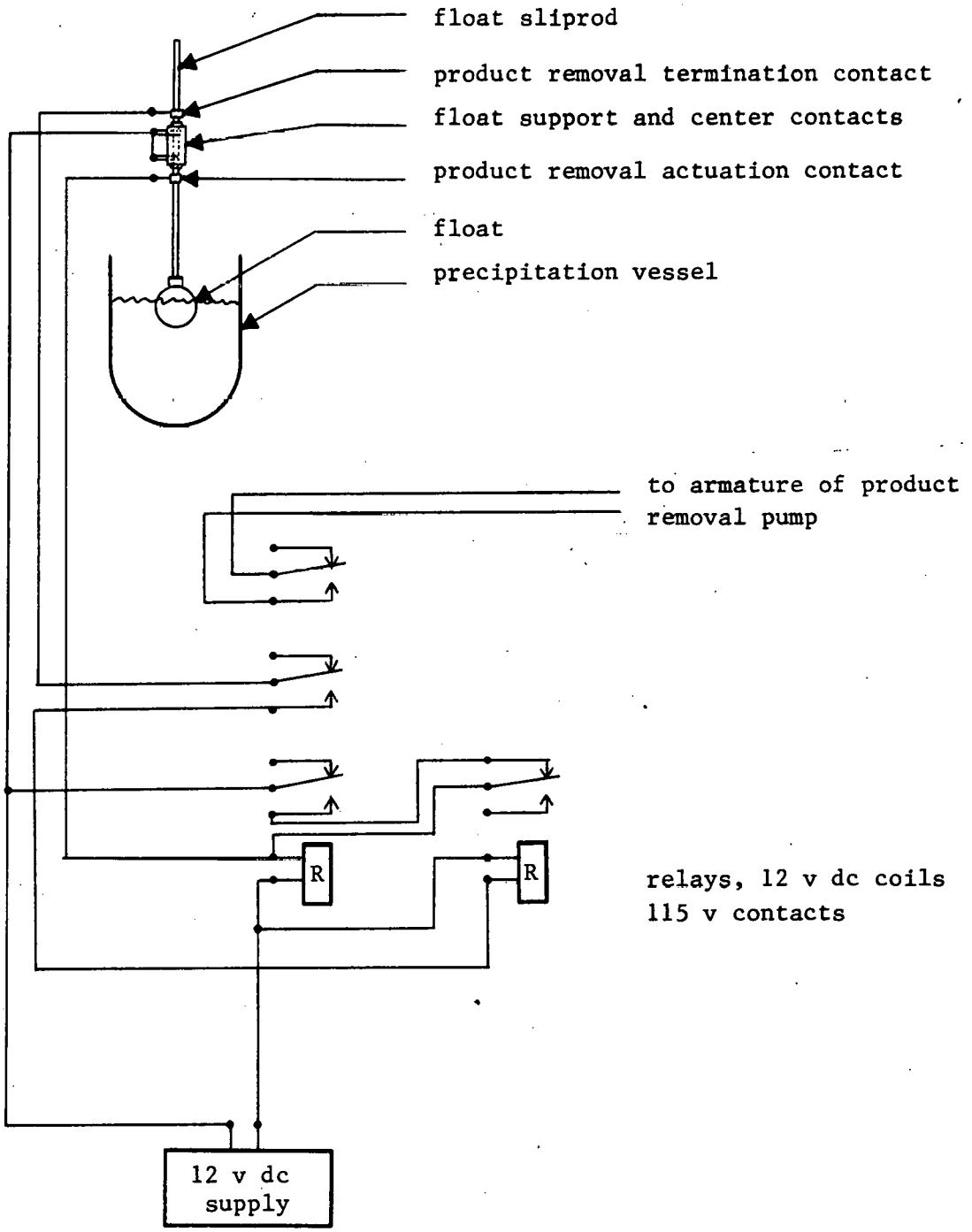

Figure 9. Intermittent product removal control system

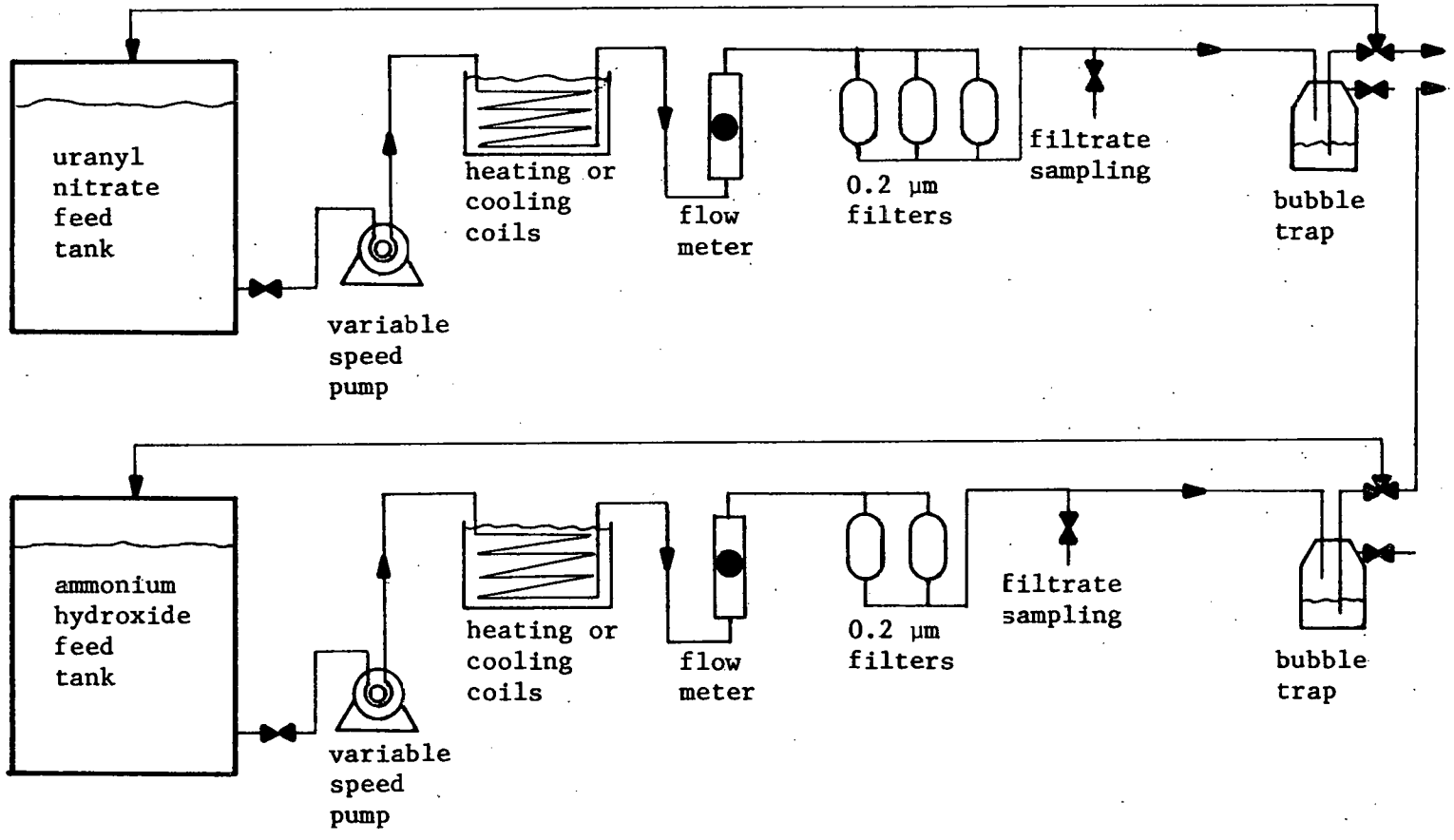

Figure 10. Equipment flow sheet

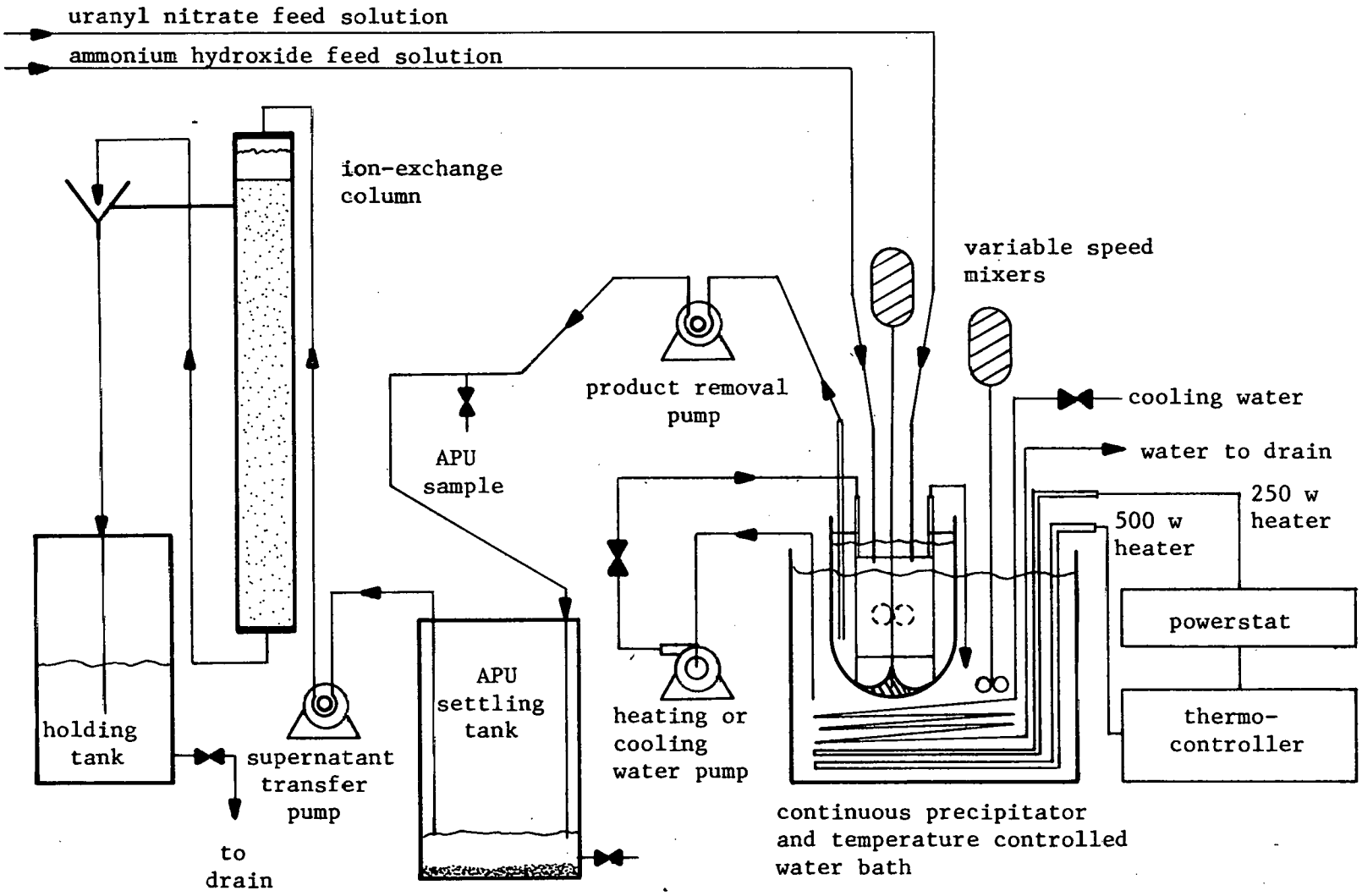

Figure 10. (continued)

thermometers are not shown. For simplicity, the heating and cooling coils have been shown as being placed in separate water baths. Actually, they are placed in the same water bath with the continuous precipitator. Most of the equipment was located in a walk-in hood, with the exception of the ion-exchange column and the 30 gallon uranyl nitrate, APU settling, and supernatant liquid holding tanks, each of which was placed on a cart for maneuverability. A photograph of the equipment setup is shown in Figure 11.

The on-line feed filters were necessary to insure counting only APU particles, and the bubble traps were used to help even out any flow perturbations. The product removal pump and both feed pumps are variable-speed peristaltic pumps using special rubber tubing.

In addition to the equipment mentioned above, another pump and filter assembly was set up to provide 0.2 μm filtered water for the initial fill of the precipitator and 0.2 μm filtered electrolyte for the Coulter counter.

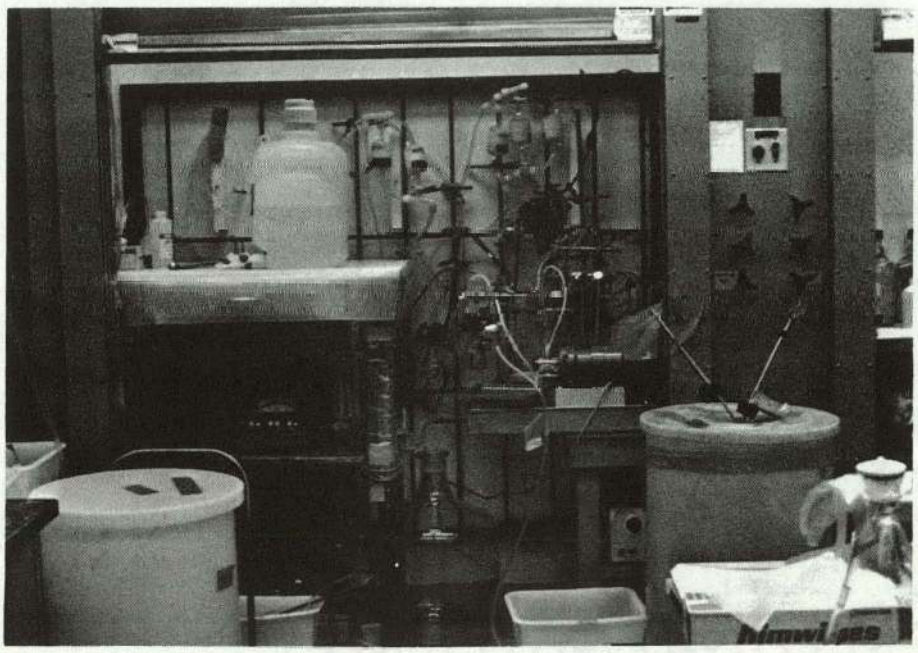

Figure 11. Equipment setup for the continuous ammonium polyuranate precipitation process.

EXPERIMENTAL PROCEDURE

The preparation for a process run involved about four hours of pre-start-up work. The product removal pump was pre-set to a flow rate such that the velocity of the mixed APU slurry being withdrawn was about the same as that of the circulating suspension. This was accomplished by calibrating the speed of the product removal pump for different flow rates and then converting this flow calibration into one of average velocity, based upon the inside diameter of the product removal tube. The circulating suspension velocity was estimated by measuring the fluid head found by placing a plastic straw at the position of the product removal tube, and calculating an average velocity based upon the equating of kinetic and potential energies. This estimated velocity was lower than the actual suspension velocity because of various energy losses, and therefore the product removal pump was set such that its product removal velocity was about 1.5 times the estimated velocity.

Four liters of filtered deionized water and filtered electrolyte, saturated with APU, were made up and both the pH meter and Coulter counter were calibrated. The feed solutions were made up and allowed to stand for about one hour to insure uniformity. Then the feed by-pass valves were set and the feed solutions circulated for about one hour through the process lines and back to the feed tanks.

Once flow through the system's lines had been established, the liquid level in the filters and bubble traps were adjusted and flowmeter

settings determined for the desired flow rates. Then the precipitation vessel was filled with filtered deionized water and the intermittent product removal float assembly adjusted for a 2ℓ suspension volume and a 0.2ℓ intermittent product removal volume.

After all the pre-start-up work had been performed, precipitation was initiated by turning the feed by-pass valves such that the feed solutions entered the precipitator. Steady state was reached between 12 and 15 residence times, after which APU samples were taken from the product removal line about every couple of residence times. The particle density of these samples was much too high for direct analysis with the Coulter counter, therefore, aliquots were taken with syringes and diluted with the filtered, APU saturated electrolyte. To help prevent particle dissolution, one drop of concentrated ammonium hydroxide was added to the electrolyte used for dilution and to the electrolyte in the counting beaker, increasing the pH to about 9.0. At the end of the run a 30 ml sample was removed from the precipitator, filtered, washed with alcohol, dried in air at 100 °C, and saved for analysis with the transmission electron microscope.

The accumulated APU slurry from the run was allowed to stand overnight during which time the precipitate settled out. The supernatant liquid was then pumped through a 4 inch diameter by 5 foot long ion-exchange column at a flow rate of 100 to 200 ml/min into a holding tank. This column was filled with Dowex 50Wx8 cation exchange resin of 40 to 50 mesh. The activity of the liquid in the holding tank was checked by the Health Physics group at Ames Laboratory and,

if it was less than the allowed maximum permissible concentration in water above natural background (4×10^{-5} μc/ml), the liquid was disposed of.

DATA ANALYSIS

Particle size distribution measurements were made on a model TA-II Coulter counter, shown in Figure 12. This instrument measures the electrical resistance across an aperture placed in an electrolyte. As each particle passes through the aperture, it displaces a volume of electrolyte equal to its own volume, causing a change in resistance. This resistance change results in a voltage pulse of short duration having a magnitude proportional to the particle volume. These pulses are then amplified, scaled, and sorted into fifteen different size ranges, based upon the volume-equivalent-diameter of spherical particles.

Usually three to five samples were taken after steady state operation of the precipitator had been achieved, and several 0.5 ml volumes counted for each sample. These particle count distributions were averaged and corrected for an average background distribution. In some instances, successive counts yielded lower numbers, indicating a small amount of particle dissolution or particle breakup. When this was apparent, only the first distribution counts of each sample were averaged together and corrected for background.

The average background distribution was determined by preparing a sample of the uranyl nitrate feed and a sample of the ammonium hydroxide feed in the same manner as was done for the APU samples. An average distribution was calculated for both feed samples, and an average background distribution determined by weighting each of the

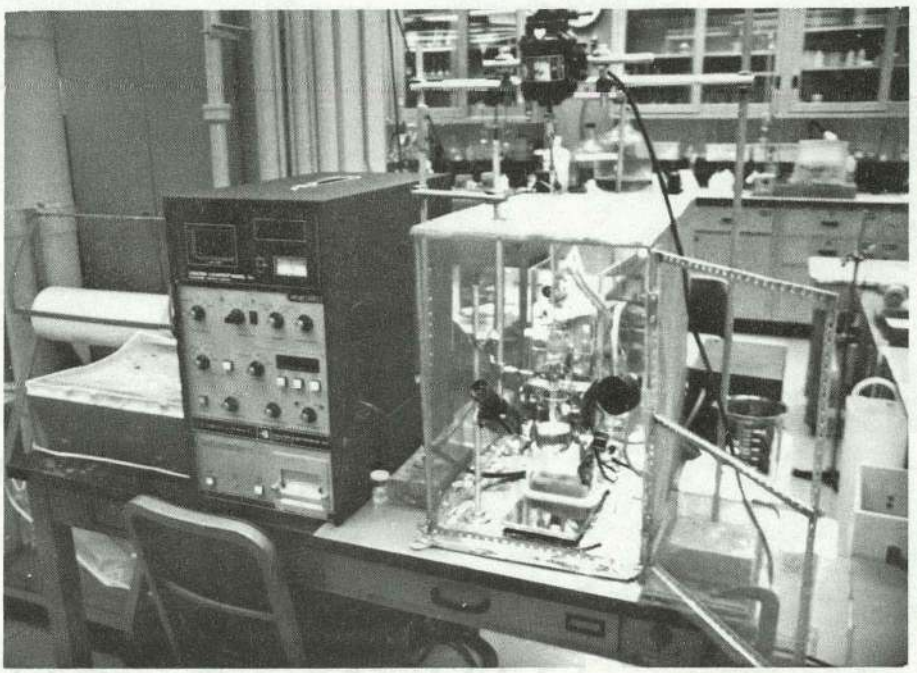

Figure 12. Model TA-II Coulter counter and shielded counting assembly.

average feed distributions by their respective fractional feed flow rate and adding the results together.

The manual for the Coulter counter indicates that coincidence particle counting is negligible at low particle concentrations which show less than 5% on the concentration index meter of the Coulter counter. These low particle concentrations were obtained through appropriate sample dilution, and therefore no corrections were made for coincidence particle counting.

The corrected average particle size distributions was converted into population density distributions by using the relation,

$$n_T(\bar{L}_i) = \frac{D\, N_i}{(L_{i+1}-L_i)v} \tag{96}$$

where D is the overall dilution factor, N_i is the average particle count for channel i, L_i is the threshold particle size for counting in channel i, L_{i+1} is the threshold particle size for counting in channel i+1, v is the APU suspension sample volume counted, and $\bar{L}_i$ is the mean particle size of channel i as given by

$$\bar{L}_i = \frac{L_{i+1} + L_i}{2} \tag{97}$$

As previously mentioned, a plot of log $n_T(\bar{L})$ versus $\bar{L}$ is the sum of three straight lines if crystal growth, primary coagulation, and secondary coagulation are all present and if the growth rates are all size-independent. However, only the primary coagulated and the secondary coagulated particles were counted since all individual crystallite sizes are below the threshold limit of the Coulter counter.

This results in the experimentally obtained population density distribution curve being the sum of only one or two straight lines, depending upon whether or not both coagulation processes are present. If only primary coagulation was present, then the data were fit with a least squares straight line. If both primary and secondary were present, a least squares straight line was fit through that portion of the curve which represented only secondary coagulation. This straight line was then subtracted from the original curve to yield only the primary coagulation data, which was subsequently fit with another least squares straight line.

The least squares program used in this work calculates the regression coefficients for p data points as

$$\text{slope} = \frac{-1}{G_e \tau} = \frac{\sum \bar{L}_i \ln n_i - \frac{1}{p}\left(\sum \bar{L}_i\right)\left(\sum \ln n_i\right)}{\sum \bar{L}_i^{\,2} - \frac{1}{p}\left(\sum \bar{L}_i\right)^2} \tag{98}$$

$$\text{intercept} = \ln n = \frac{1}{p}\left(\sum \ln n_i - b \sum \bar{L}_i\right) \tag{99}$$

and the coefficient of determination as

$$r^2 = \frac{\left(\sum \bar{L}_i \ln n_i - \frac{1}{p}\sum \bar{L}_i \sum \ln n_i\right)^2}{\left[\sum \bar{L}_i^{\,2} - \frac{1}{p}\left(\sum \bar{L}_i\right)^2\right]\left[\sum \left(\ln n_i\right)^2 - \frac{1}{p}\left(\sum \ln n_i\right)^2\right]} \tag{100}$$

RESULTS AND DISCUSSION

Most of the experimental runs involved only precipitations at different values of pH, since the literature review indicated that the pH is the primary process variable controlling the particle size of the APU precipitate. The uranium concentration was varied in the later experiments to see the effect of changes in suspension density for two specific ammonia to uranium (NH_3:U) mole ratios.

Prior to the operation of the continuous APU precipitation process, several batch precipitations were carried out in a stepwise manner by adding ammonium hydroxide to uranyl nitrate solutions made from analytical grade uranyl nitrate hexahydrate (UNH). With the total suspension volumes being held at 1000 $\pm$ 50 ml, the pH values were recorded at various NH_3:U mole ratios. This was done only after the pH remained stable for a period of at least 20 to 30 sec, since equilibrium is established slowly. The color of the yellow uranyl nitrate solution deepened as ammonium hydroxide was added, and sometimes a gel-like precipitate formed and slowly re-dissolved. Further addition of alkali resulted in a permanent precipitate being formed at an NH_3:U mole ratio of about 1.6. Three of these pH curves are shown in Figure 13, and they are similar to those which have been previously reported in the literature (26,38,39,103). These curves were used to determine the NH_3:U reacting feed mole ratios (RFMR) necessary for precipitation at desired pH values. Note that both the uranium concentration and the NH_3:U RFMR are important in determination of the pH at a given temperature.

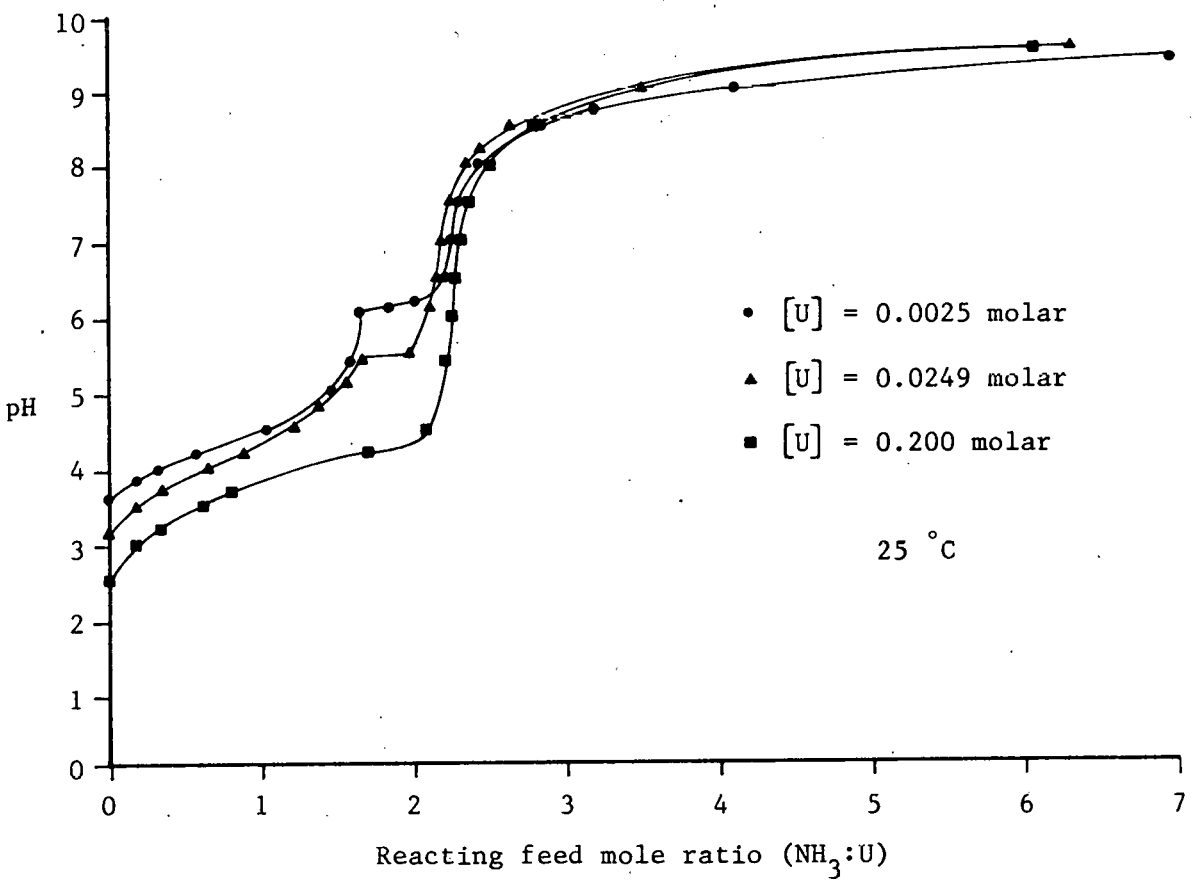

Figure 13. Titration curves for different uranium concentrations (ammonium hydroxide being added to uranyl nitrate solution)

The UNH which was used for the continuous APU precipitation process was obtained from the National Lead Company of Ohio. Their people indicated that this UNH was 50.5 wt% uranium and that it already contained some ammonia, as was evident by its bright yellow color rather than the very pale yellow color of analytical grade UNH. A pH curve was made for this UNH ($[U]$ = 0.0249 molar) and compared to that made from the analytical grade UNH. These curves are similar except that they are displaced 0.35 NH_3:U mole ratio units apart, indicating the presence of 0.35 moles of ammonia per mole of uranium in the UNH.

The continuous APU precipitation process was operated for 20 experimental runs, the conditions of which are listed in Table 5. The precipitations were done at room temperature (25 to 27 °C) to avoid difficulties in maintaining the filtered saturated electrolyte and APU samples at the operating temperature during sample analysis. A residence time of 13 min was chosen so that steady state conditions would be reached within a reasonable length of time (2.5 to 3.5 hrs). The first 14 runs involved changes in the NH_3:U RFMR for a 0.0249 molar uranium concentration. This concentration was chosen because it is within the concentration range which has been reported in the literature, and yet it was low enough to require relatively small amounts of uranium for experimental runs. Figure 14 shows the extremes of the population density distribution (PDD) obtained under these conditions through changes in the NH_3:U RFMR. The population densities varied from a narrow range arising from primary

Table 5. Experimental conditions for APU precipitations

uranyl nitrate flow rate = 140 ml/min
ammonium hydroxide flow rate = 17.8 ml/min
suspension hold up volume = 2050 ml
residence time = 13.0 min
stirring rate = 1200 rpm

Run Number	U (moles/ℓ)	NH_3 (moles/ℓ)	RFMR	T (°C)	pH (at 25°C)
1	0.0249	0.4602	2.70	25.0	8.60
2	0.0249	0.4367	2.58	25.2	8.50
3	0.0249	0.3682	2.23	25.0	7.51
4	0.0249	0.3995	2.39	25.5	8.15
5	0.0249	0.3956	2.37	25.5	8.12
6	0.0249	0.3896	2.34	25.5	8.00
7	0.0249	0.3593	2.20	25.0	7.10
8	0.0249	0.3593	2.19	25.5	7.13
9	0.0249	0.3691	2.23	26.0	7.50
10	0.0249	0.3769	2.28	26.0	7.78
11	0.0249	0.3437	2.08	25.5	5.84
12	0.0249	0.3515	2.15	25.5	6.49
13	0.0249	0.3554	2.17	26.0	6.80
14	0.0249	0.6132	3.47	26.0	9.00
15	0.2000	2.886	2.18	27.0	4.60
16	0.0025	0.0361	2.19	25.0	5.47
17	0.0025	0.0616	3.73	25.5	8.88
18	0.2000	4.926	3.48	27.5	9.0
19	0.0100	0.246	3.48	25.5	8.27
20	0.1000	2.463	3.48	26.0	9.10

Figure 14. Population density distribution extremes for precipitation at a constant uranium concentration of 0.0249 molar

THIS PAGE

WAS INTENTIONALLY

LEFT BLANK

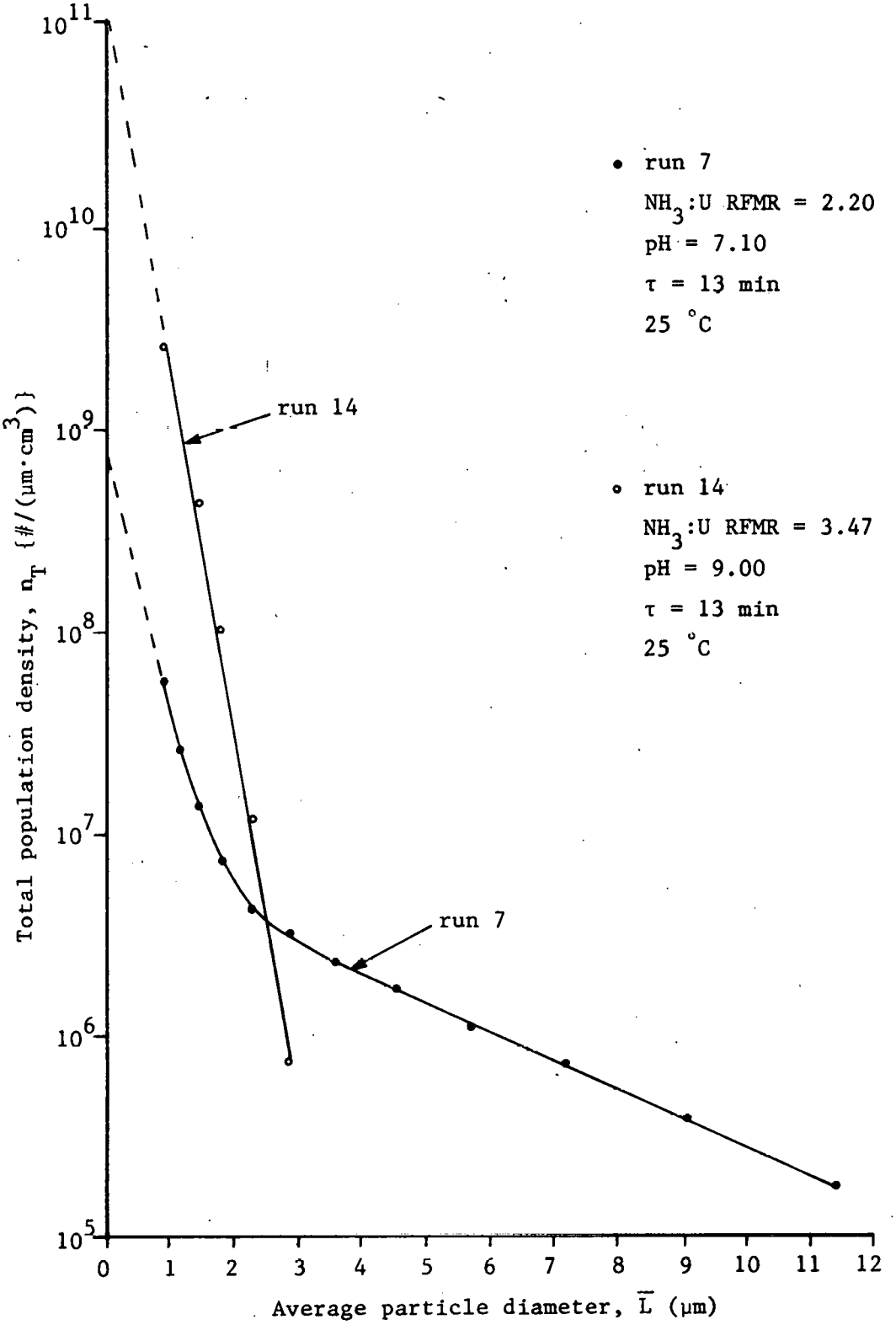
10^{11}
10^{10}
10^{9}
10^{8}
10^{7}
10^{6}
10^{5}
Total population density, n_T {#/(μm·cm^3)}
0 1 2 3 4 5 6 7 8 9 10 11 12
Average particle diameter, $\bar{L}$ (μm)
run 14
run 7
• run 7
NH_3:U RFMR = 2.20
pH = 7.10
τ = 13 min
25 °C
∘ run 14
NH_3:U RFMR = 3.47
pH = 9.00
τ = 13 min
25 °C

coagulation in run number 14 (NH_3:U RFMR = 3.47, pH = 9.00) to a much wider range resulting from both primary and secondary coagulation in run number 7 (NH_3:U RFMR = 2.20, pH = 7.10). The shape of the PDD from run number 14 is typical of those obtained when precipitating at high pH values (NH_3:U RFMR $\geq$ 2.34, pH $\geq$ 8.00); and the shape of the PDD from run number 7 is typical of those obtained when precipitating at low pH values (NH_3:U RFMR < 2.34, pH < 8.00)

Characterization of APU Particle Growth Rates and Structures

The measured PDD's for low values of NH_3:U RFMR and pH result from the sum of two size-independent particle growth processes, as indicated in Figure 15. The postulation that these two processes are actually primary and secondary coagulation, rather than some type of size-dependent process, is supported not only from the shape of the PDD, but also through observations of the precipitate with the scanning electron microscope (SEM). Figure 16 and 17 show several particles ranging from approximately 1 to 15 μm in diameter, obtained from run number 12. The large particles are agglomerates of smaller clusters, whose upper size limit is between 3 and 4 μm. The clusters are also composed of smaller particles, those being the individual APU crystallites in the submicron size range. The larger of the three small particles shown just above the large particle in Figure 17 could be either a cluster or small agglomerate, since it is difficult to distinguish between these two types of particles when they are of similar size. The remaining two smaller particles could be individual crystals of APU.

Figure 15. Resolution of the population density distribution from run number 7, shown in Figure 14, into two size-independent growth processes

THIS PAGE

WAS INTENTIONALLY

LEFT BLANK

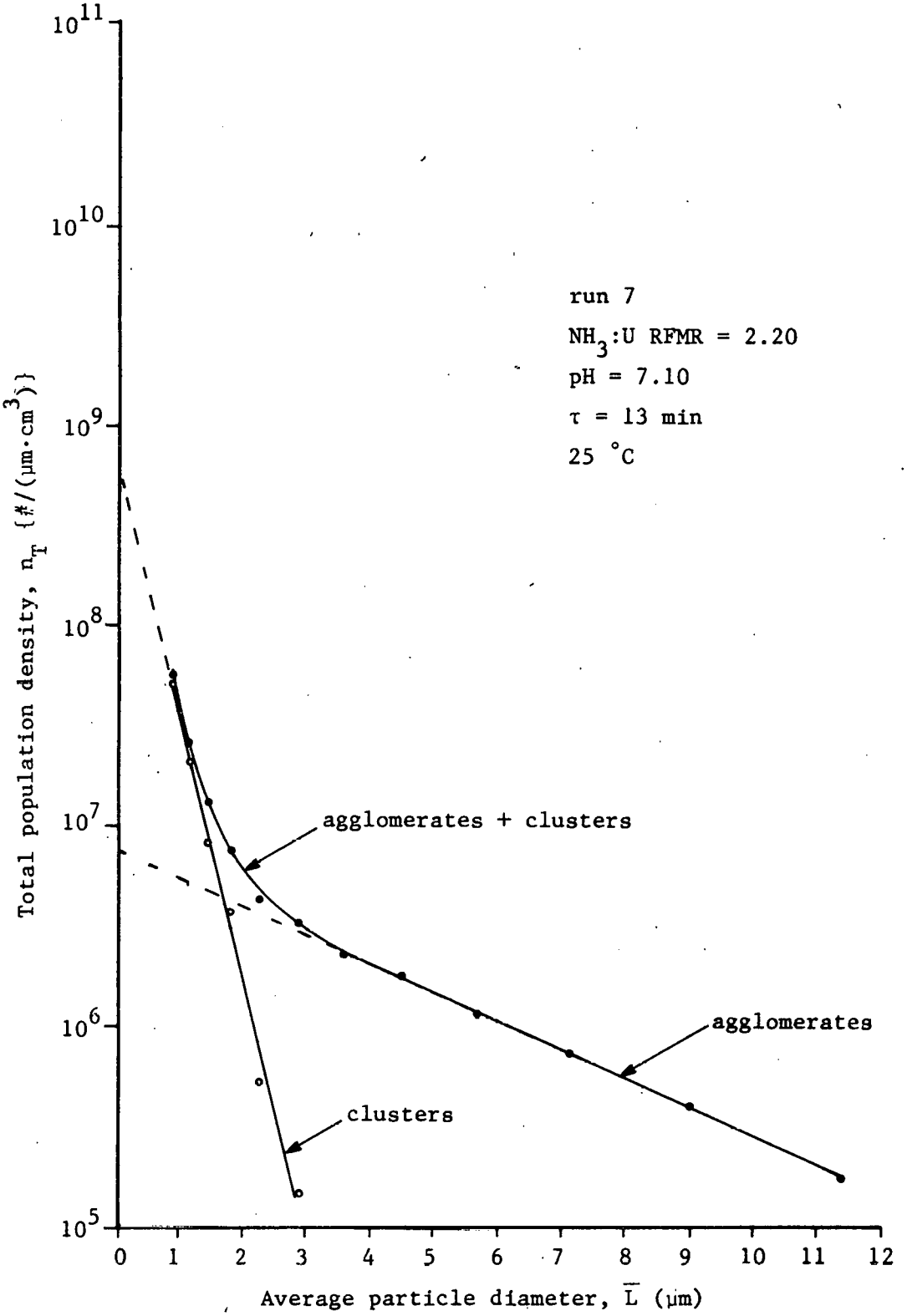
run 7
NH3:U RFMR = 2.20
pH = 7.10
τ = 13 min
25 °C
agglomerates + clusters
agglomerates
clusters
Total population density, nT {#/(μm·cm3)}
Average particle diameter, L̄ (μm)
10^11
10^10
10^9
10^8
10^7
10^6
10^5
0 1 2 3 4 5 6 7 8 9 10 11 12

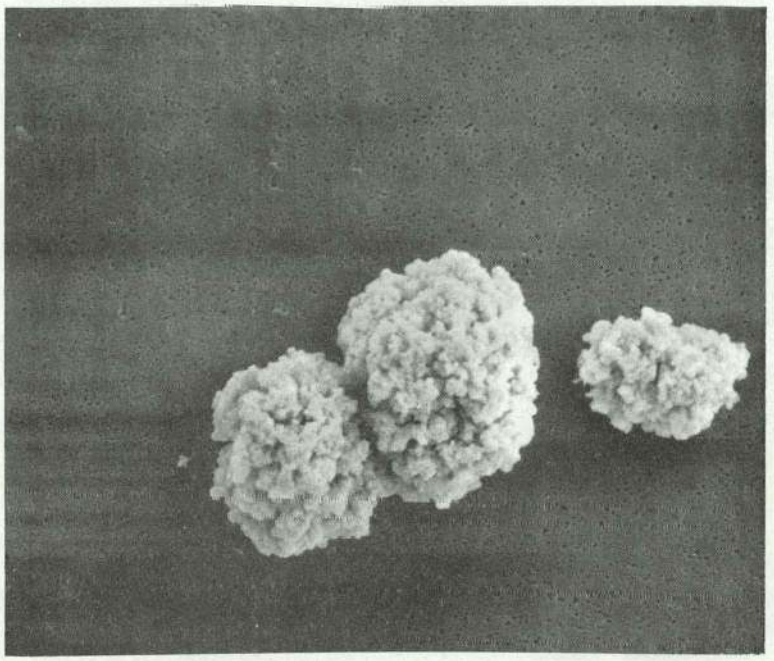

1μm

Figure 16. SEM micrograph (2,700 x) of APU from run number 12 (NH_3:U RFMR = 2.15, pH = 6.49).

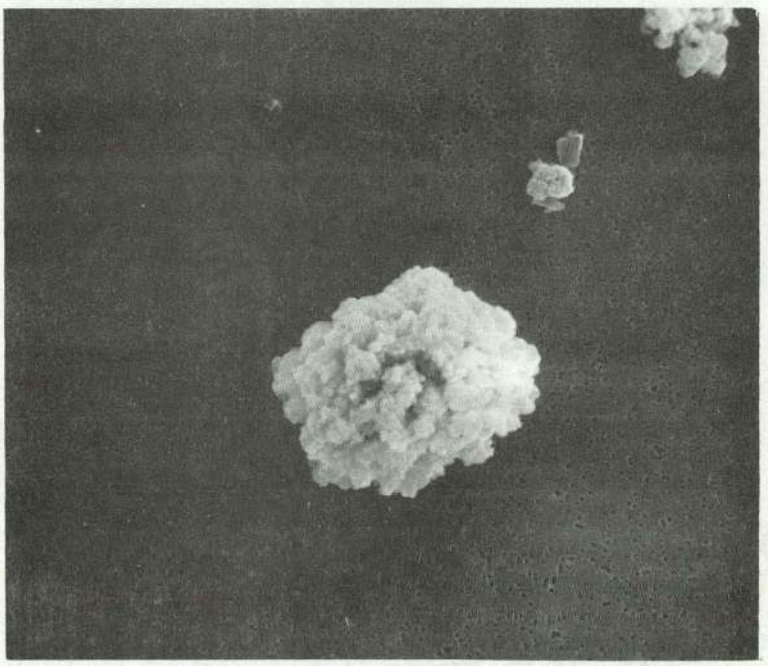

1μm

Figure 17. SEM micrograph (3,300 x) of APU from run number 12 (NH_3:U RFMR = 2.15, pH = 6.49).

The structure of the large agglomerates is such that many large pores and open spaces (~1 μm) are present, while that of the clusters is more closely packed, with only small voids (<0.3 μm) being present. The structure and size range of these APU particles are consistent with those reported in the literature (5,31,62,86) and the agglomerates have been previously differentiated as primary and secondary agglomerated particles (40). Explanation of their size range, however, through the use of coagulated particle growth rates and nucleation rates is a new approach to the characterization of this precipitate. As will be shown later, these growth rates and nucleation rates can be correlated with the process conditions, allowing the population densities and distributions of these different particles to be predicted and controlled.

The agglomerates do not conform to any size-dependent growth process, unless a mechanism can be proposed to explain not only their structure, but also the change in the shape of their PDD from a curve (size-dependent growth) for particles greater than 4 μm in diameter as shown for run 7 in Figure 15. It was mentioned previously in the theory on the kinetics of precipitation that coagulation will not be present if the population density is less than 10^6 particles/ml unless coagulation agents are added. The presence of any coagulation of higher order than secondary would, in this precipitation work, be unexpected because of the relatively low agglomerate population densities.

Figures 17 and 18 show that the structure of the clusters and agglomerates becomes looser and more flocculent as the pH and NH_3:U RFMR is increased until, at values of pH above 7.8 and NH_3:U RFMR above 2.3,

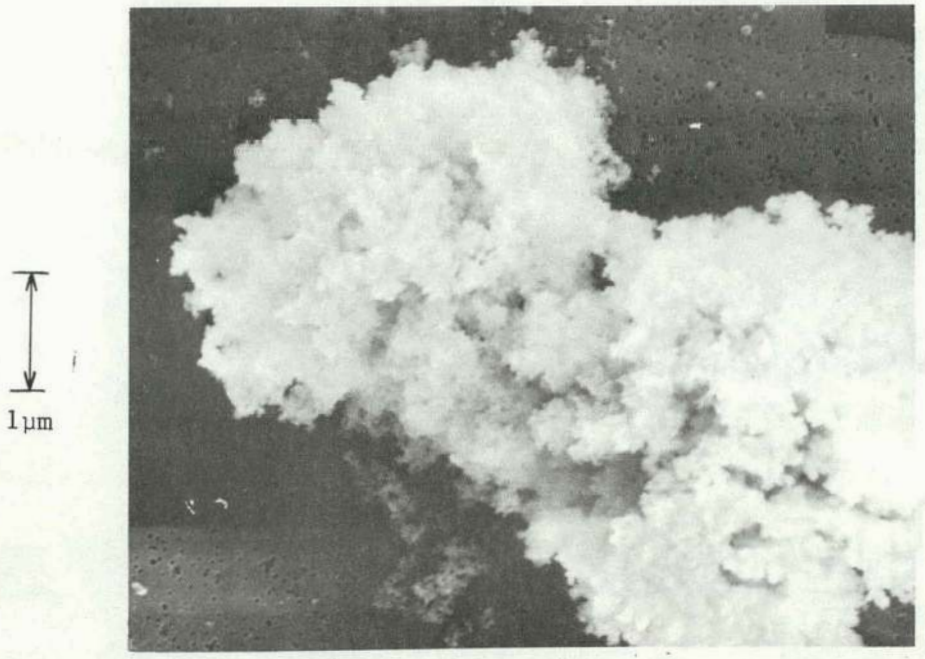

Figure 18. SEM micrograph (3,300 x) Of APU from run number 8 (NH_3:U RFMR = 2.19, pH = 7.13).

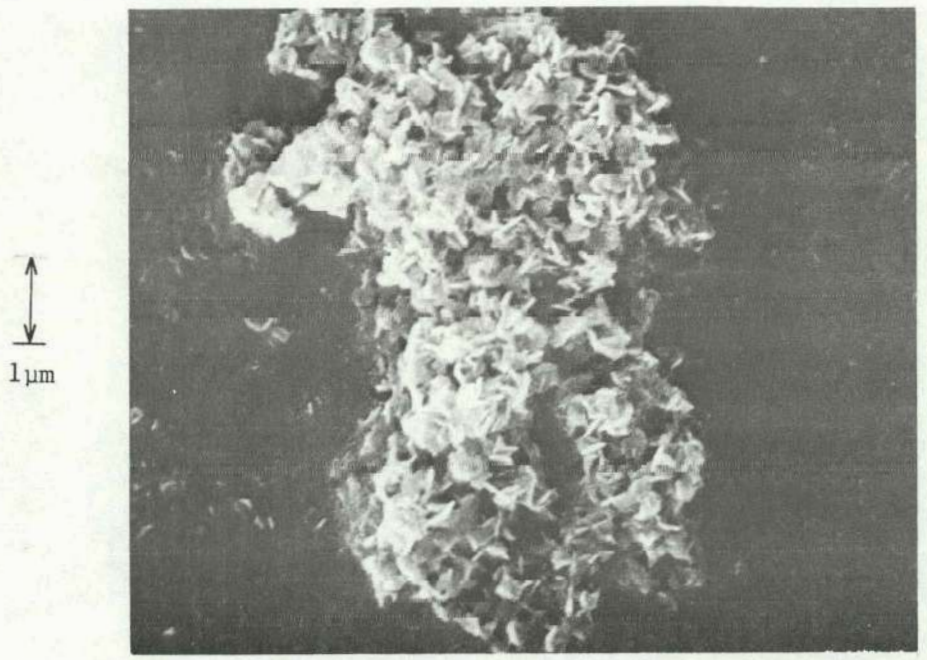

Figure 19. SEM micrograph (11,000 x) of APU from run number 14 (NH_3:U RFMR = 3.47, pH = 9.00).

they collapse on the filter membrane as shown in Figure 19. When the NH_3:U RFMR is above 2.3, it is difficult to distinguish between the primary and secondary coagulation processes because the particles are too loosely bonded and their growth rates are too close to one another. The fact that this effect is really that of increased NH_3:U RFMR rather than one of increased pH will be discussed later.

Some of the precipitate from each run was filtered, washed with alcohol, and dried in air at 100 °C for 48 hrs. Figures 20, 21 and 22 are SEM micrographs of some of these APU filter cakes and they show that the structure and size of the APU crystallites vary with the NH_3:U RFMR and the pH of precipitation (note that the magnification in Figure 19 is about three times that shown in Figures 17 and 18). The fact that the elementary APU particles are thin, hexagonal crystals is clearly illustrated in the micrograph from a transmission electron microscope (TEM), shown in Figure 23.

A more accurate characterization of the APU particle structure is the subject of a forthcoming thesis by Timothy Oolman, a graduate student in the Department of Chemical Engineering at Iowa State University. He is characterizing the APU particle structure with the SEM, and also determining the APU effective crystal growth rate ($G_{e,x}$) and average crystal size ($\overline{L}_x$) with the TEM. Since this information is not yet available, it was not possible to determine values for the APU crystal growth rates (G_x), coagulation constants (k'_x, k''_x, k_c), average particle sizes ($\overline{L}_c$, $\overline{L}_a$), average minimum particle sizes ($\overline{L}_{m,c}$, $\overline{L}_{m,a}$), average nucleate population densities ($\overline{n}^o_c$, $\overline{n}^o_a$), dominant particle

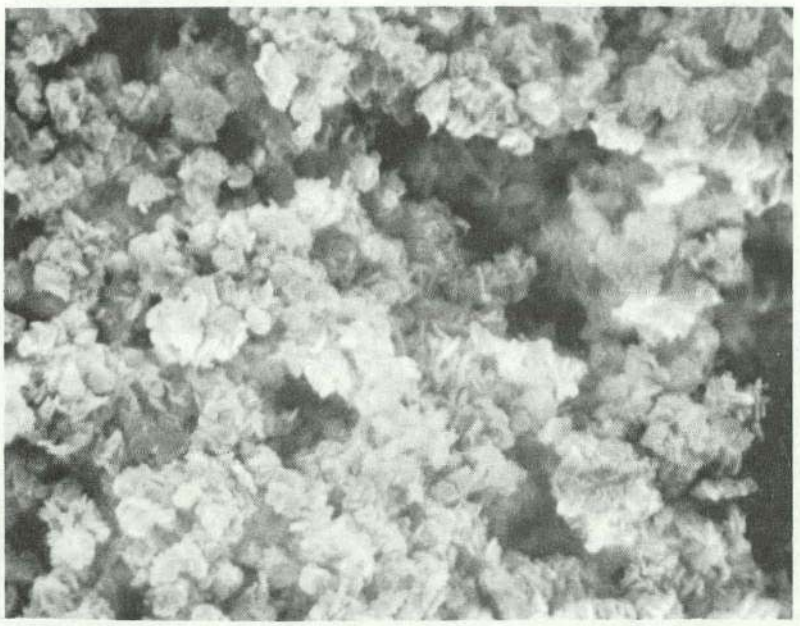

1μm

Figure 20. SEM micrograph (11,000 x) of APU filter cake from run number 7 (NH_3:U RFMR = 2.20, pH = 7.10).

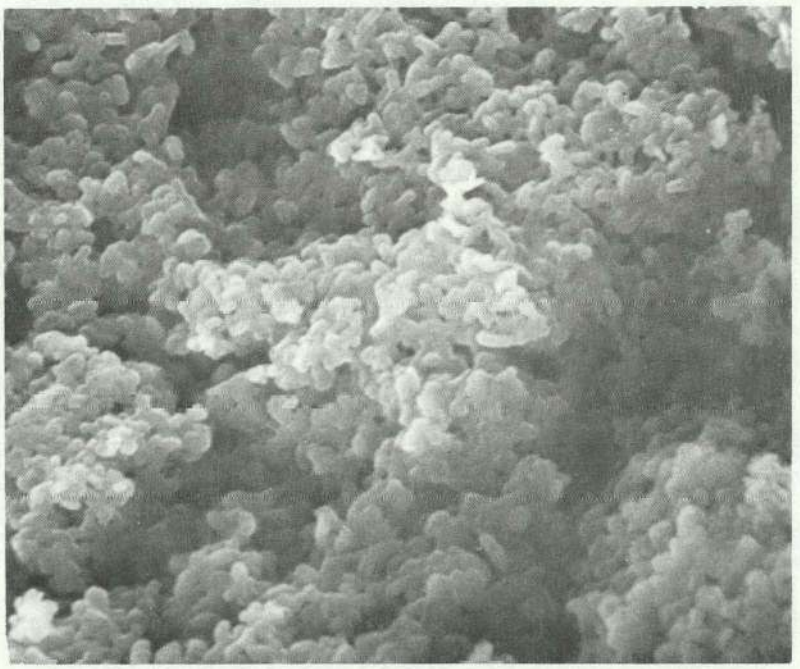

1μm

Figure 21. SEM micrograph (11,000 x) of APU filter cake from run number 10 (NH_3:U RFMR = 2.28, pH = 7.78).

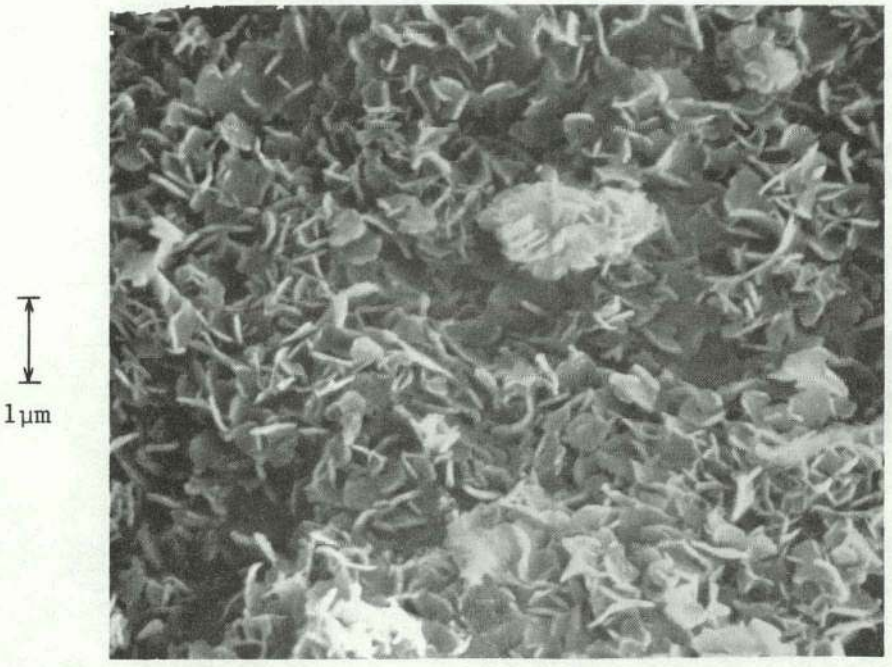

Figure 22. SEM micrograph (11,000 x) of APU filter cake from run number 14 (NH_3:U RFMR = 3.47, pH = 9.00).

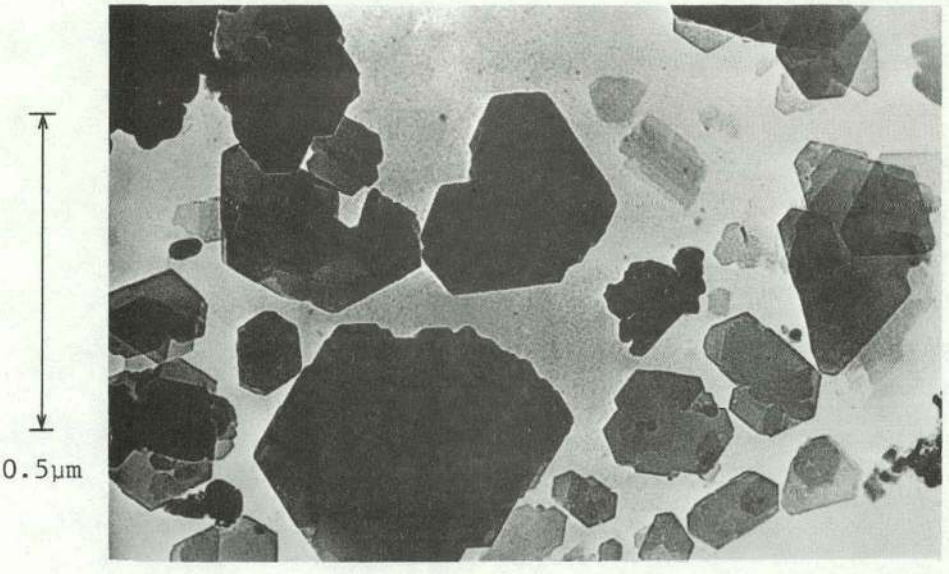

Figure 23. TEM micrograph (83,000 x) of APU filter cake from run number 7 (NH_3:U RFMR = 2.20, pH = 7.10).

sizes ($L_{d,x}$, $L_{d,c}$, $L_{d,a}$), and suspension densities (M_x, M_c, M_a) for the different experimental runs (see Table 4). It was possible to investigate the behavior of the effective coagulation growth rates with respect to changes in process variables. It was also possible to determine the effect of process variables on the nucleate population densities and nucleation rates by using extrapolated nucleate population densities (n_c^o, n_a^o) rather than the average nucleate population densities ($\overline{n}_c^o$, $\overline{n}_a^o$). This introduces a slight error in calculated values of nucleation rates, nucleation constants, and kinetic orders of nucleation if the average minimum particle sizes ($\overline{L}_{m,c}$, $\overline{L}_{m,a}$) are much greater than zero, however, the trend of the results will still be the same. This error goes to zero as the average minimum sizes approach zero, since the values of the average nucleate population densities will approach those of the extrapolated nucleate population densities.

Kinetic Results of Precipitation

The kinetic results from the continuous precipitation experiments are listed in Table 6. The PDD from runs number 1 through number 6 could not be resolved into both primary and secondary coagulation processes because of noise in the first few channels of the Coulter counter and the fact that, under their precipitation conditions, the two coagulation growth rates are too close together.

The regression coefficients are significantly close to unity to indicate that the fitted least squares straight lines are good representations of the experimental data. In slightly less than half of the precipitations, some amount of particle dissolution or break up was

Table 6. Kinetic results from experimental runs

Run Number	Type of Particles[a]	$n^o \times 10^{-8}$ #/(μm·cm^3)	$G_e \times 10^{+4}$ (μm/sec)	$B^o \times 10^{-5}$ #/(cm^3·sec)	r^2
1	a	507	4.09	208	0.9978
2	a	322	4.46	144	0.9986
3[b]	-	-	-	-	-
4	a	14.7	6.87	28.7	0.9995
5[c]	a	16.2	8.33	13.5	0.9985
6	a	13.7	9.27	12.7	0.9976
7[c]	c	6.64	4.23	2.81	0.9932
	a	0.0773	38.7	0.299	0.9998
8[c]	c	6.95	4.51	3.13	0.9988
	a	0.0740	39.4	0.292	0.9993
9	c	9.84	4.77	4.69	0.9951
	a	0.166	32.7	0.541	0.9994
10[c]	c	31.4	3.47	10.9	0.9927
	a	1.79	17.1	3.05	0.9979
11	c	7.02	3.71	2.60	0.9893
	a	0.773	25.8	2.00	0.9982
12[c]	c	3.60	4.34	1.56	0.9995
	a	0.167	37.2	0.619	0.9994
13[c]	c	6.02	3.96	2.38	0.9986
	a	0.0912	38.9	0.355	0.9969
14[c]	c	1,440	3.06	440	0.9942

[a] c = clusters, a = agglomerates

[b] Pump failed before steady state was reached

[c] Some particle dissolution or break up noticed while counting

[d] No precipitation under these conditions

Table 6. (continued)

Run Number	Type of Particles[a]	$n^o \times 10^{-8}$ #/(μm·cm^3)	$G_e \times 10^{+4}$ (μm/sec)	$B^o \times 10^{-5}$ #/(cm^3·sec)	r^2
15	c	8.83	3.53	3.11	0.9987
	a	0.101	83.1	0.843	0.8652
16	c	11.9	1.90	2.25	0.9567
	a	0.000332	33.4	0.00111	0.9888
17[d]	-	-	-	-	-
18	c	9,470	2.68	2,540	0.9960
	a	0.774	7.68	0.594	0.9926
19[c]	c	11.4	9.36	0.107	0.9987
20	c	5,010	3.29	1,650	0.9989

noticed during sample analysis. This was evident through decreasing numbers of successive particle counts. The results were consequently affected in such a way that the calculated values of the growth rates were higher than their actual values, and the nucleate population densities and nucleation rates were lower than their true values. The percentage change in the calculated values of effective growth rates, G_e, nucleate population densities, n^o, and nucleation rates, B^o, between the first count and the second count were less than 4%, 10%, and 7% respectively for the secondary process, and less than 13%, 40%, and 35% respectively for the primary process. Usually the errors were less than half of these values.

This problem was significantly reduced after run number 12, where it was found that the addition of one drop of concentrated ammonia to the APU sample considerably reduced the amount of particle disappearance. Thus much of the problem was related to the solubility of APU, which is less soluble at high values of pH. It is not known why some experimental runs showed some particle break up or dissolution during sample analysis while others did not. In those cases where this particle disappearance phenomenon was present, the errors involved were not enough to affect the general trend of the results. No attempt was made at placing confidence limits on these results since the process was run only once at any given set of conditions.

The effective coagulation growth rates are plotted as functions of pH in Figure 24. Secondary coagulation, which gives rise to agglomerates, appears to be very sensitive to changes in pH, whereas

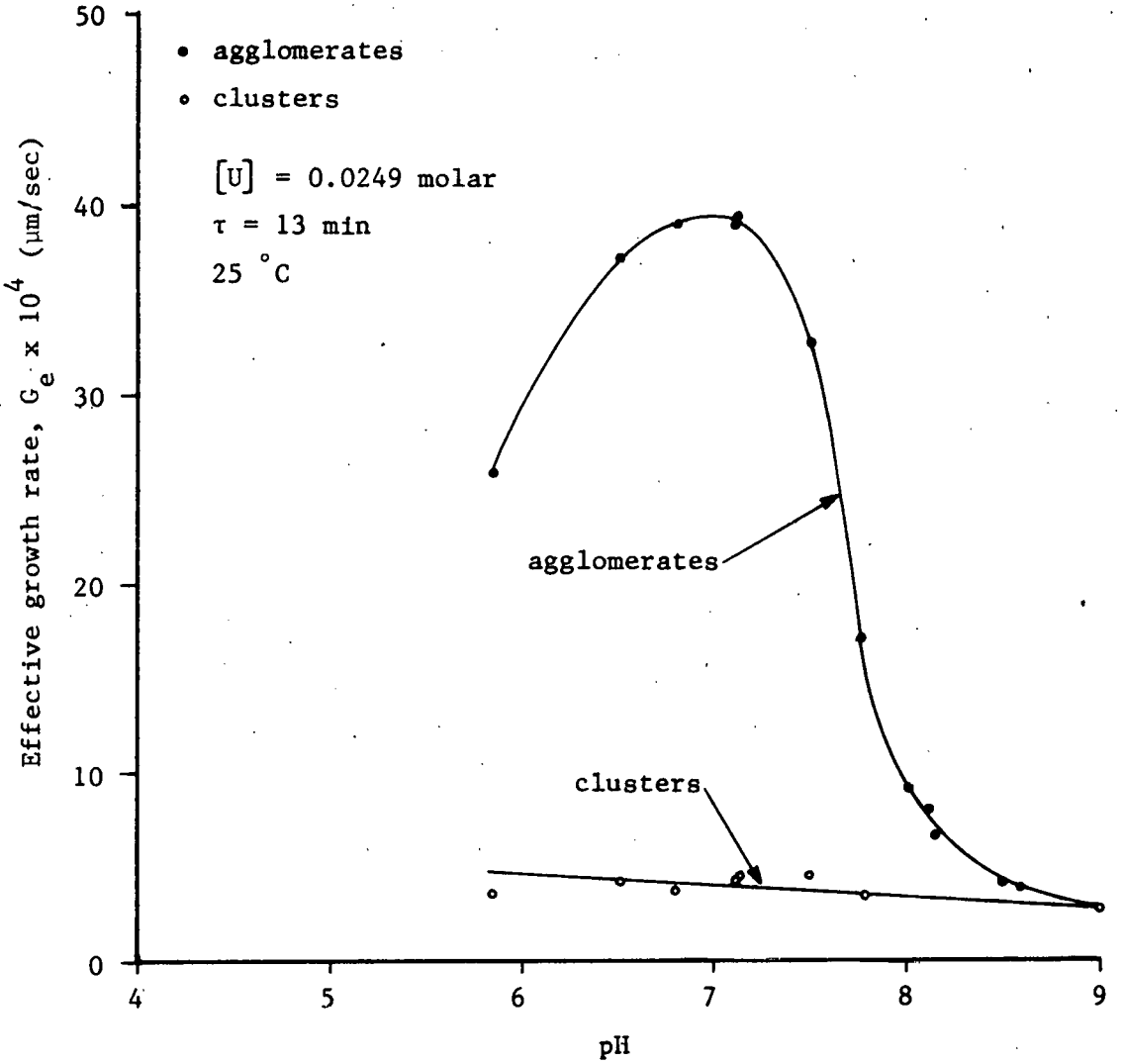

Figure 24. Strong dependence of agglomerate growth rate on the pH of precipitation

the primary coagulation, which produces clusters, seems relatively insensitive to the precipitation pH. The peak in the secondary coagulation growth rate is the result of the combination of coagulation rate changes and supersaturation changes. As mentioned earlier, the coagulated particles are less strongly bonded as the pH or NH_3:U RFMR is increased, indicating that the zeta potential around the particles is being increased through the addition of ammonium hydroxide. This causes the coagulation rates to decrease and results in increased surface area being available for crystal growth because of looser particle structures and smaller particle size distributions. The supersaturation, which determines the APU crystallites growth rate and nucleation rate, decreases because of the increased surface area. This effect is counteracted by the increase in supersaturation which arises from the extreme decrease in APU solubility as the pH increases. The combination of these supersaturation effects and the coagulation effect results in a peak in the agglomerate growth rate. These same effects also influence the cluster growth rate, however the result is not as noticeable since the clusters involve fewer crystallites.

The extrapolated nucleate population densities and their respective nucleation rates are shown in Figures 25 and 26 as functions of pH. These curves have pronounced minimums because of the inverse relationship between nucleate population density and the effective growth rate. This inverse relationship is illustrated in Figure 27, in which log n^o is plotted versus log G_e. The primary coagulation data are scattered more than the secondary coagulation data because of the larger errors which

Figure 25. Pronounced minimums for extrapolated nucleate population densities of clusters and agglomerates

THIS PAGE

WAS INTENTIONALLY

LEFT BLANK

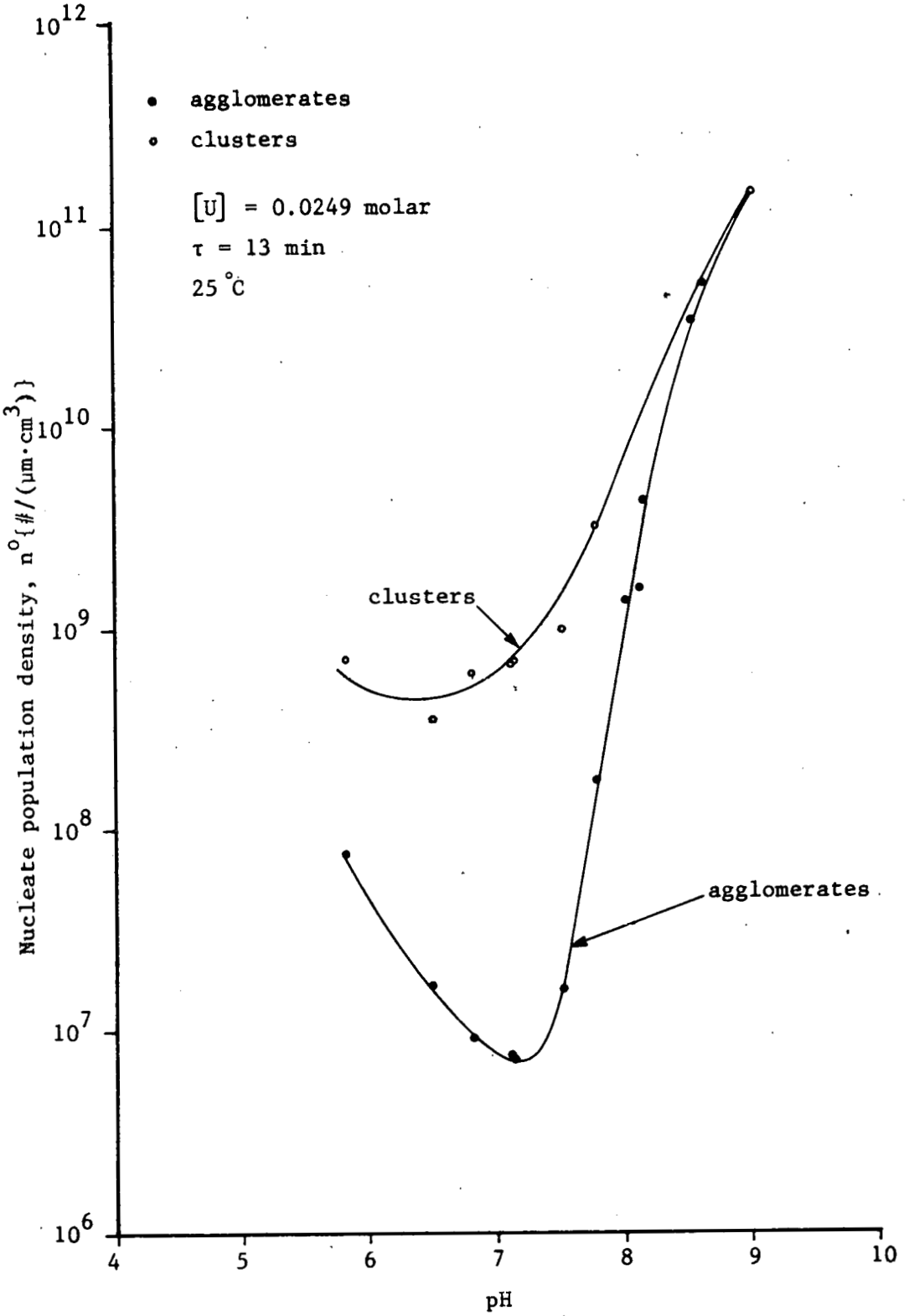
agglomerates
clusters
[U] = 0.0249 molar
τ = 13 min
25 °C
clusters
agglomerates
Nucleate population density, n°{#/(μm·cm³)}
pH
10¹²
10¹¹
10¹⁰
10⁹
10⁸
10⁷
10⁶
4
5
6
7
8
9
10

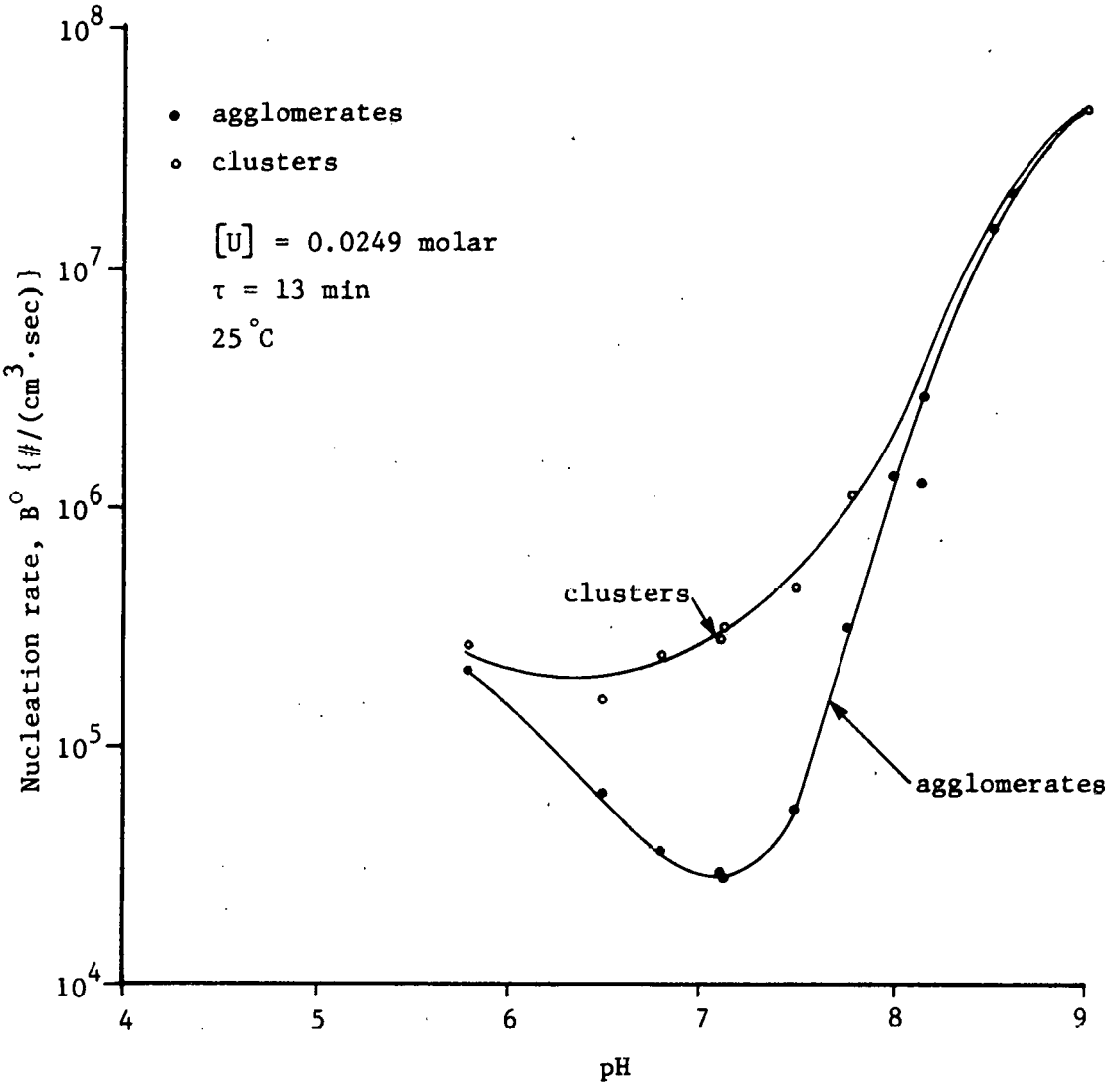

Figure 26. Pronounced minimums for the nucleation rates of the clusters and agglomerates

Figure 27. Kinetic correlation for APU agglomerates and clusters

THIS PAGE

WAS INTENTIONALLY

LEFT BLANK

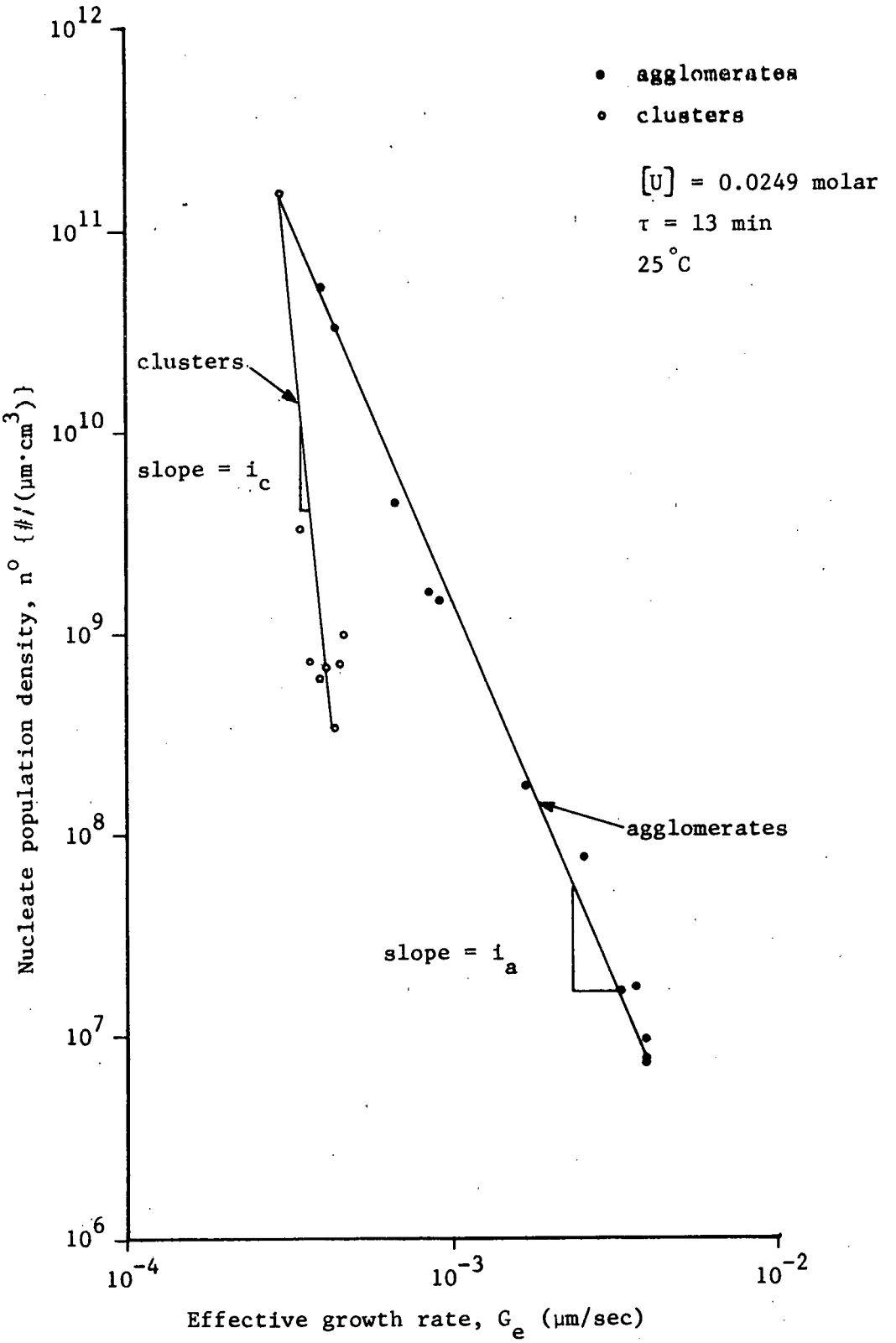
agglomerates
clusters
[U] = 0.0249 molar
τ = 13 min
25 °C
clusters
slope = i_c
agglomerates
slope = i_a
Nucleate population density, n° {#/(μm·cm^3)}
Effective growth rate, G_e (μm/sec)
10^{12}
10^{11}
10^{10}
10^{9}
10^{8}
10^{7}
10^{6}
10^{-4}
10^{-3}
10^{-2}

are possible when extrapolating the PDD of the clusters in order to obtain the cluster nucleate population density. It is also interesting to note in Figures 24, 25, and 26 that as the secondary coagulation process diminishes at high values of pH, the values of its kinetic parameters approach those of primary coagulation.

The extrapolated nucleate population densities of the clusters and agglomerates can be expressed by Equation (81) and (82).

$$n_c^o = k_{N,c}(G_{e,c})^{i_c-1}(M_T)^{j_c} \qquad (81)$$

$$n_a^o = k_{N,a}(G_{e,a})^{i_a-1}(M_T)^{j_a} \qquad (82)$$

With the suspension densities having been held constant, the following values for the growth rate kinetic orders of nucleation can be obtained from the slopes of the curves shown in Figure 27,

$i_c = -9.42$ $\qquad r^2 = 0.6304$

$i_a = -2.69$ $\qquad r^2 = 0.9919$

where r^2 is the regression coefficient. Note that in the case of coagulating particles the kinetic order of nucleation is negative. This is just the opposite of what occurs during crystallization, where the kinetic order of nucleation is always positive. This phenomena was expected, since a shift in the PDD of coagulated particles to larger sizes must require lower population densities in the smaller sizes, if the total number of crystallites remains relatively constant.

Kinetic Correlations with NH_3:U RFMR

One persistent question which evolved through this work was whether or not the kinetic parameters are functions of pH, NH_3:U RFMR, or both.

Precipitations were not carried out at a specific NH_3:U RFMR for different values of pH but a report by Janov, Alfredson, and Vilkartis (62), who investigated the influence of precipitation conditions on the properties of APU and UO_2 powders, helped provide an answer to this question. They correlated precipitation pH with APU settling and filtration rates, as others have done. However they also used the SEM to look at the particle structure. When precipitation was carried out at 50 °C and 0.3 molar uranium concentration, the highest settling rates were obtained for a pH of 3.5 (NH_3:U RFMR = 2.2). The precipitate showed the presence of large, strongly agglomerated particles (20 to 24 μm). These agglomerates persisted throughout calcination and reduction, yielding a heterogeneous UO_2 pellet microstructure containing grains larger than 10 μm. This proved to be undesirable since a higher pellet density can be achieved when the grain structure is homogeneous and of small size (~3 μm). They reported that in order to produce such a homogeneous grain structure the APU particles should be small and loosely agglomerated, as obtained at high pH values (~8.4). Unfortunately the particles which were formed at high pH proved difficult to filter, and therefore it was necessary to compromise by lowering the pH to 7.2 (NH_3:U RFMR = 2.4), where the particles are still 3 μm or smaller and not too strongly agglomerated.

It is interesting to note that the peak in the agglomerate particle size in their work occurred at a pH of 3.5, whereas the peak in the agglomerate growth rate in this work was found at a pH of about 7.0. In both cases, the NH_3:U RFMR was 2.2, indicating that the APU precipitate should be correlated with this variable rather than pH. With this being

the case, the kinetic parameters G_e, n^o, and B^o should really be expressed as functions of the NH_3:U RFMR as shown in Figures 28, 29 and 30. This is a significant conclusion since the precipitation studies reported in the literature show correlations of the APU settling and filtration rates, and hence particle size, with the precipitation pH.

Kinetic Effects of Suspension Density

The results discussed up to this point have shown that it is possible to vary the particle size distribution and structure of the APU precipitate by changing the NH_3:U RFMR. The effects of changes in the suspension density will now be discussed and shown to be an equally important process variable.

In order to examine the effects of different suspension densities, several precipitations were done using different uranium concentrations for two specific NH_3:U RFMR's (runs number 15 to number 20). These precipitations involved the following NH_3:U RFMR's; (1) a value of 2.20, when the particle growth rate is the greatest and the particle structure is strongly bonded, and (2) a value of 3.47, when the particle growth rate is the smallest and the particles are very loosely structured.

Figures 31, 32, and 33 show how G_e, n^o, and B^o vary with increasing uranium concentration at an NH_3:U RFMR of 2.2. Both cluster and agglomerate growth rates increase initially but at a sufficiently high particle density the cluster growth rate decreases and secondary coagulation becomes dominant. The strong dependence of the secondary coagulation process on the particle density is evident through the rapid increase in agglomerate nucleate population density, shown in Figure 32, and nucle-

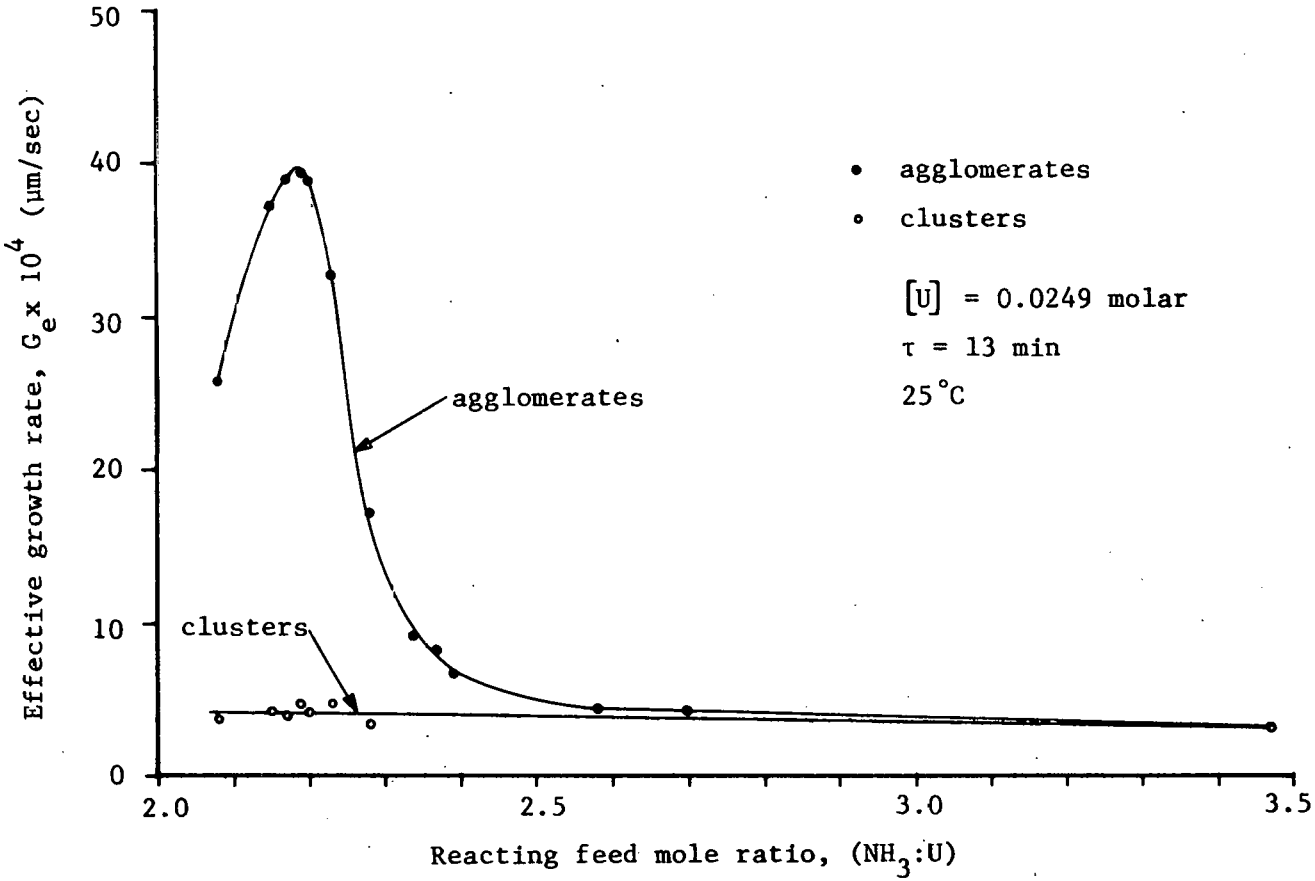

Figure 28. Strong dependence of the agglomerate effective coagulation growth rate on the NH_3:U RFMR

Figure 29. Pronounced minimums and leveling off of extrapolated nucleate population densities of clusters and agglomerates

THIS PAGE

WAS INTENTIONALLY

LEFT BLANK

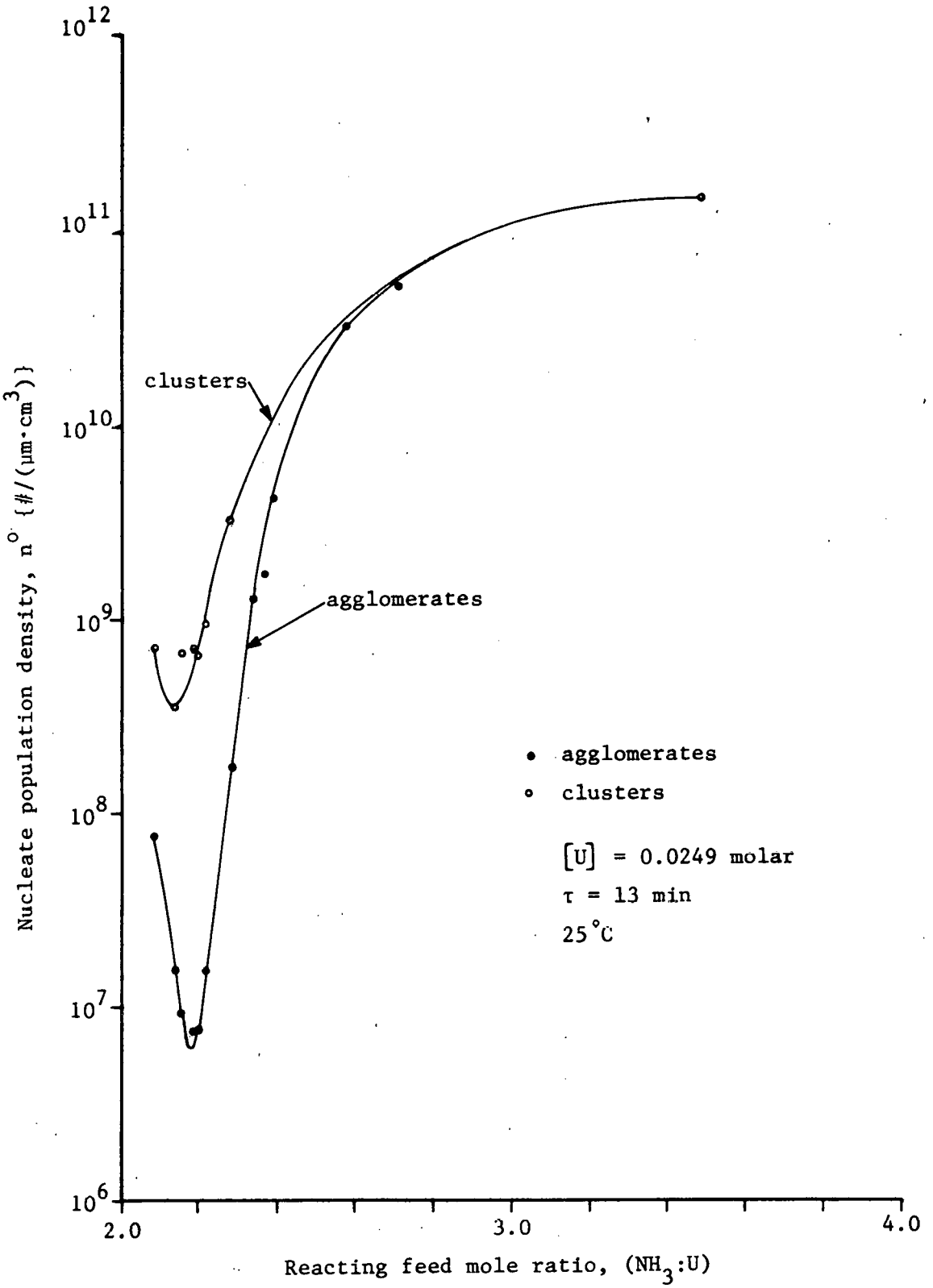
10^{12}
10^{11}
10^{10}
10^{9}
10^{8}
10^{7}
10^{6}
Nucleate population density, n° {#/(μm·cm^3)}
clusters
agglomerates
• agglomerates
∘ clusters
[U] = 0.0249 molar
τ = 13 min
25 °C
2.0
3.0
4.0
Reacting feed mole ratio, (NH_3:U)

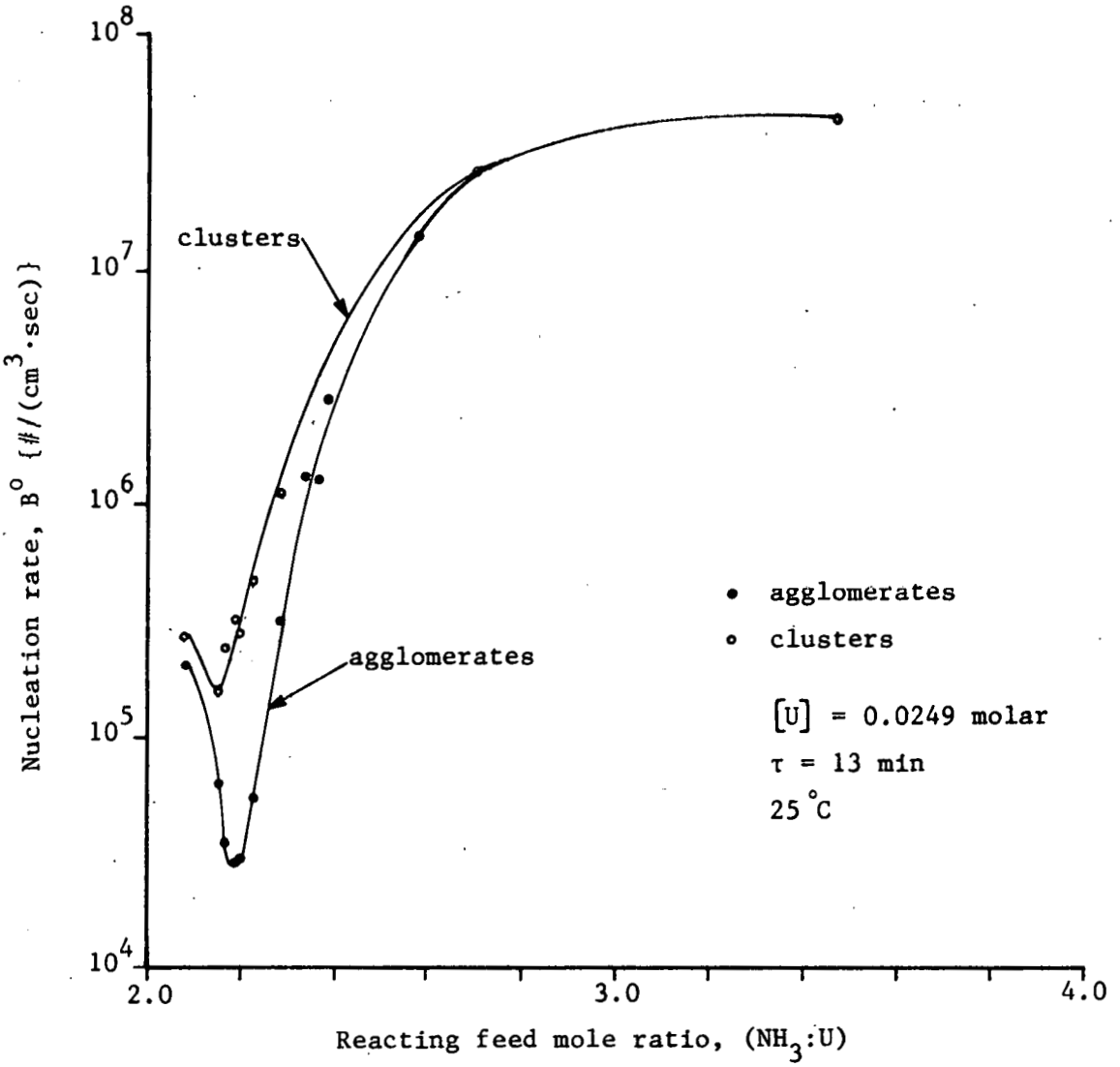

Figure 30. Pronounced minimum and leveling off of cluster and agglomerate nucleation rates

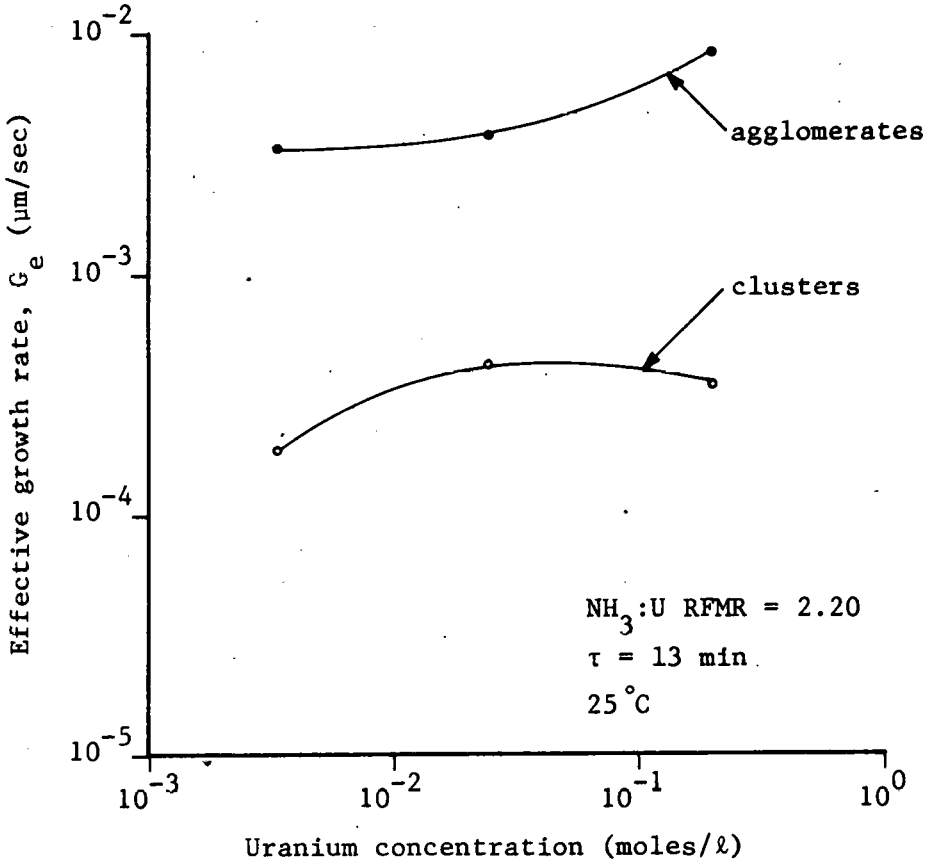

Figure 31. Increasing cluster (∘) and agglomerate (•) growth rates, with the agglomerate growth rate becoming dominant at high uranium concentrations

Figure 32. Rapid increase and leveling off of agglomerate extrapolated nucleate population density

THIS PAGE

WAS INTENTIONALLY

LEFT BLANK

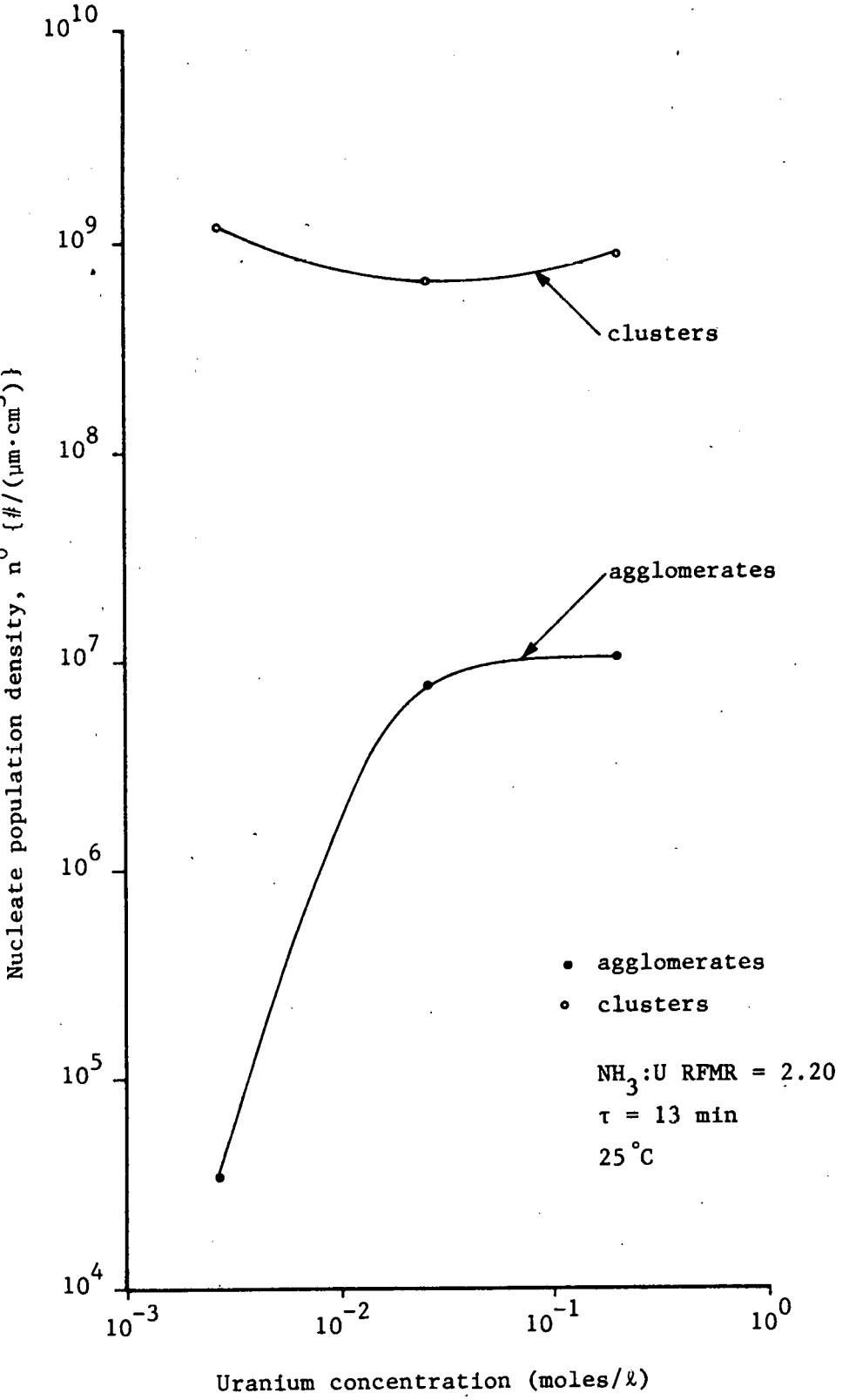
10^{10}
10^{9}
10^{8}
10^{7}
10^{6}
10^{5}
10^{4}
Nucleate population density, n^{o} {#/(μm·cm^{3})}
clusters
agglomerates
• agglomerates
∘ clusters
NH_3:U RFMR = 2.20
τ = 13 min
25 °C
10^{-3}
10^{-2}
10^{-1}
10^{0}
Uranium concentration (moles/ℓ)

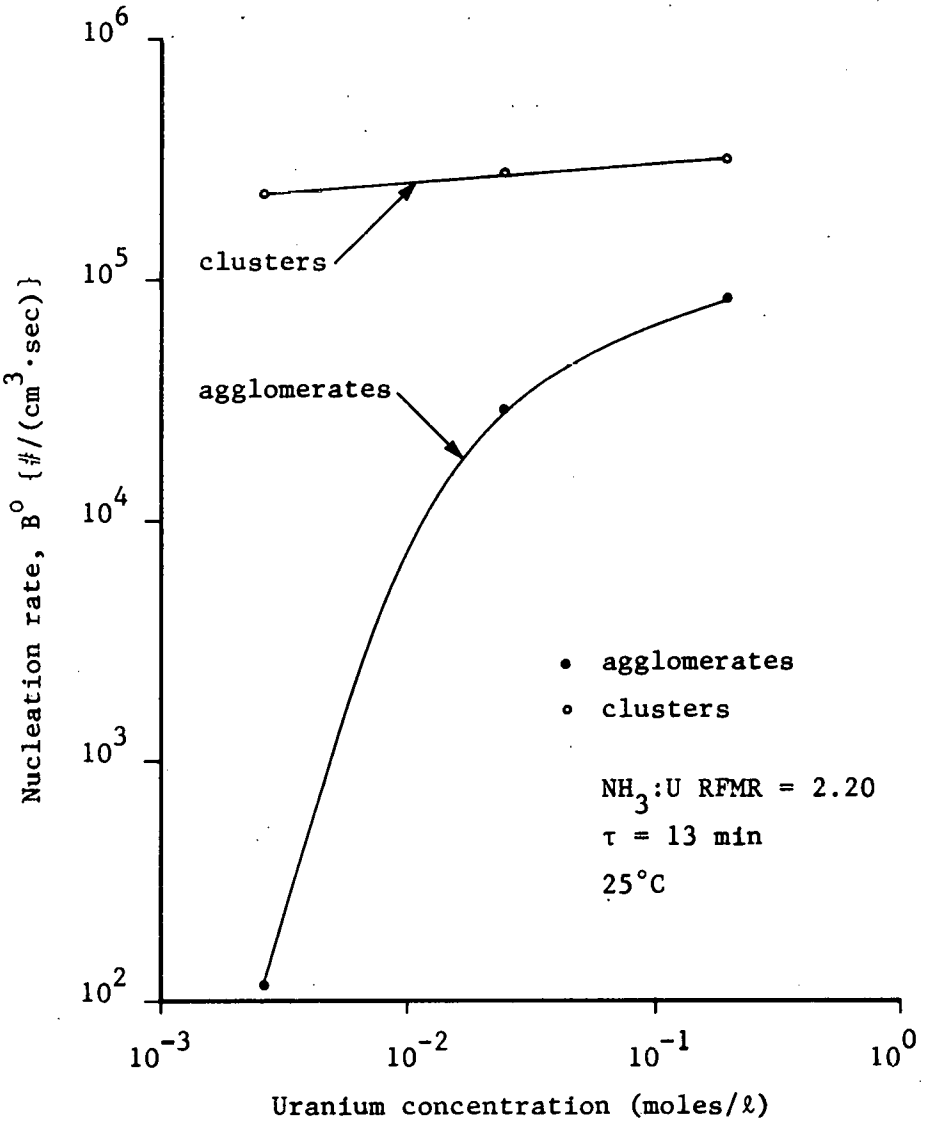

Figure 33. Increasing agglomerate nucleation rate

ation rate, shown in Figure 33, as the uranium concentration is increased from low levels. At this point, one can make a very interesting observation recalling that the total number of clusters and agglomerates is given by Equations (47) and (48),

$$N_c = \bar{n}_c^{o} G_{e,c} \tau \qquad (47)$$

$$N_a = \bar{n}_a^{o} G_{e,a} \tau \qquad (48)$$

and that their average nucleation rates are given by Equations (85) and (86).

$$\bar{B}_c^{o} = \bar{n}_c^{o} G_{e,c} \exp(\bar{L}_{m,c}/\tau G_{e,c}) \qquad (85)$$

$$\bar{B}_a^{o} = \bar{n}_a^{o} G_{e,c} \exp(\bar{L}_{m,a}/\tau G_{e,a}) \qquad (86)$$

The total number of clusters and agglomerates is seen to be simply the product of the residence time and average nucleation rate, modified by a factor accounting for their average minimum sizes. The behavior of the nucleation rate with respect to changes in the uranium concentration will also represent the dependence of the total number of particles (of a certain type) on the uranium concentration. Figure 33 indicates, therefore, that as the uranium concentration is increased, the total number of clusters remains relatively constant while the number of the agglomerates increases dramatically. Now, if a particular ratio of these two types of particles is desired in order to achieve a specific grain structure in a sintered product, then this can be accomplished by choosing the appropriate uranium concentration.

Figures 34, 35, and 36 show how G_e, n^o, and B^o are affected by changes in the uranium concentration when the NH_3:U RFMR is 3.47. Under this condition, secondary coagulation does not occur until the very

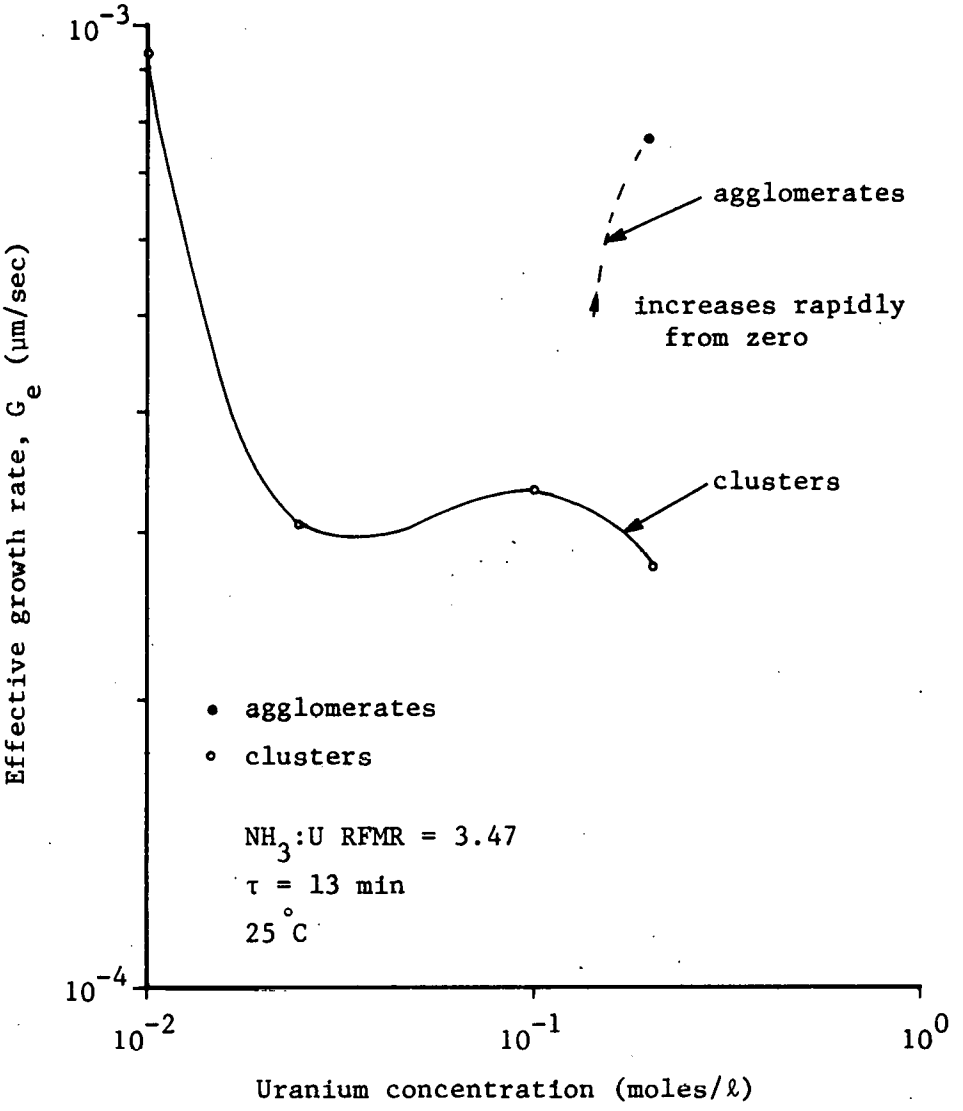

Figure 34. Decreasing cluster growth rate resulting from zeta potential effects at low uranium concentrations and secondary coagulation effects when uranium concentrations are greater than 0.1 molar

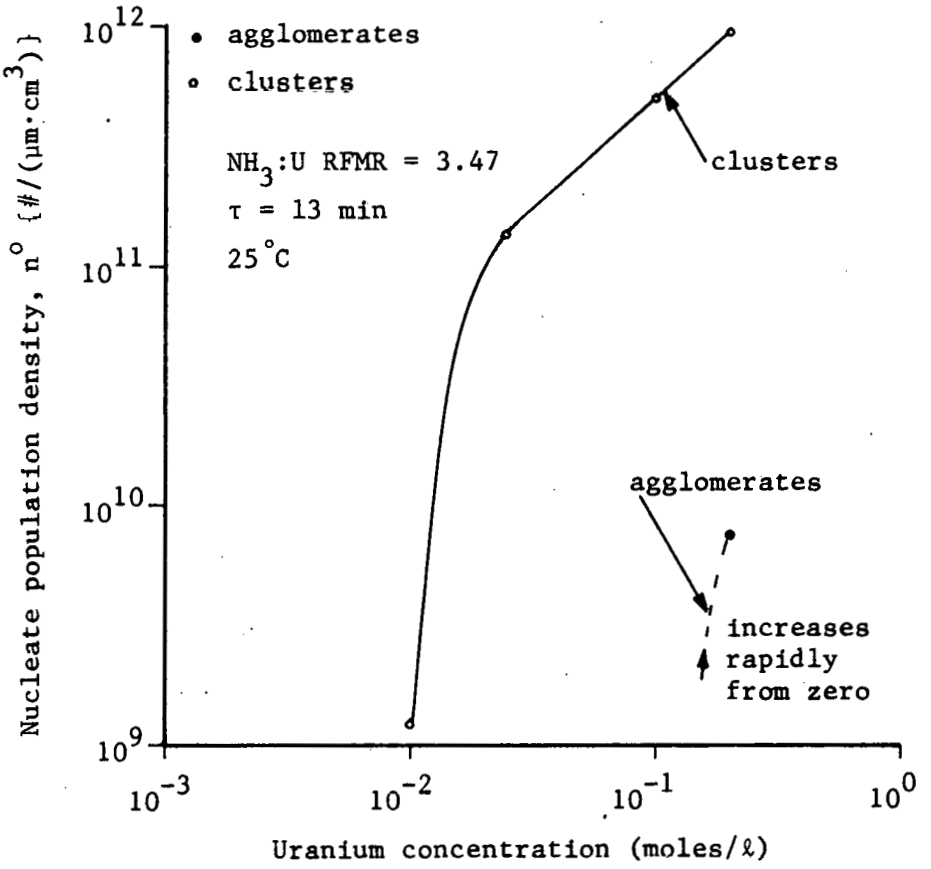

Figure 35. Rapidly increasing cluster and agglomerate extrapolated nucleate population densities

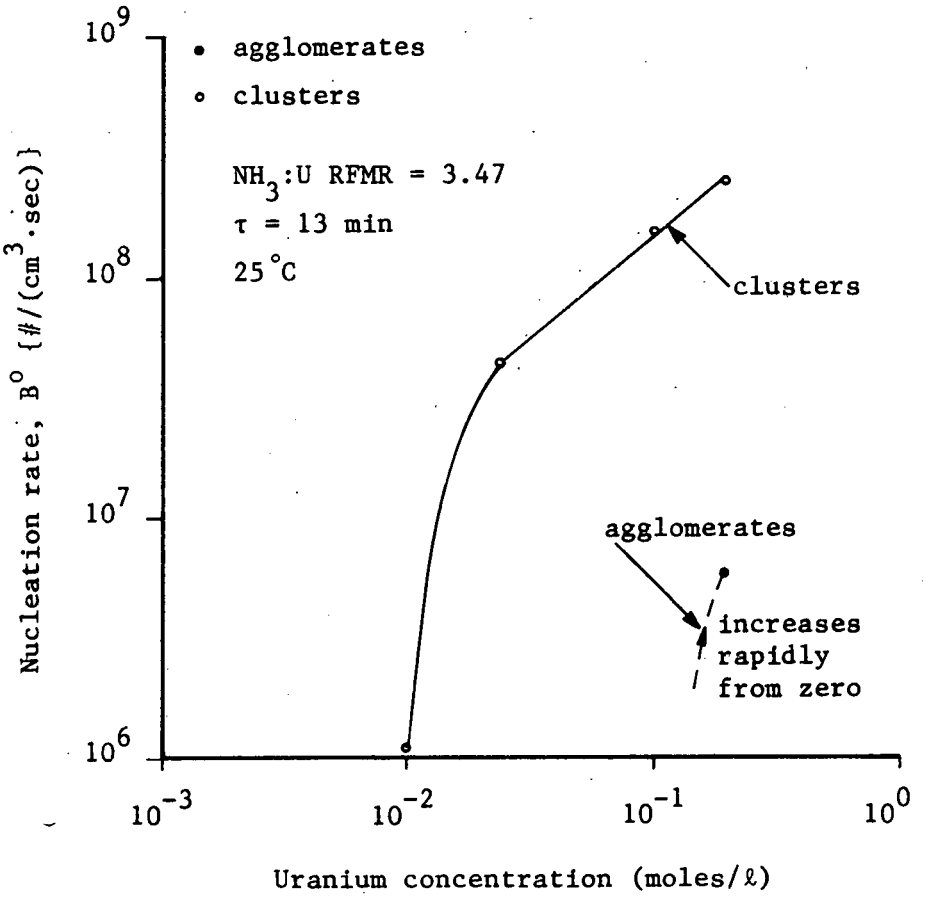

Figure 36. Rapidly increasing cluster and agglomerate nucleation rates

high cluster population densities associated with high uranium concentration are present. Initially the cluster growth rate decreases as the uranium concentration is increased. This can be explained by a large decrease in the zeta potential due to the increase in ammonia concentration; however this effect is eventually counteracted by the large increase in the crystallite population density at higher uranium concentrations. As the uranium concentration continues to increase, secondary coagulation sets in, decreasing the cluster growth rate.

The extrapolated cluster nucleate population density, cluster nucleation rate, and hence total number of clusters, increase rapidly as the uranium concentration increases in the range where the zeta potential effect is dominant. As the uranium concentration increases in the range where the effect of crystallite population density becomes significant, they then show a linear relationship with the uranium concentration or suspension density.

Referring once again to Equations (81) and (82), which represent the cluster and agglomerate extrapolated nucleate population densities, a plot of $-\log(n^o/(G_e)^{i-1})$ versus $-\log[U]$ will allow determination of the suspension density kinetic order of nucleation, j, from the slope, and the nucleation constant, k_N, from the intercept. Figure 37 shows these curves for the two NH_3:U RFMR's which were investigated for suspension density effects. The following values were obtained for the nucleation constants and suspension density kinetic orders of nucleation.

NH_3:U RFMR = 3.47 $\quad k_{N,c} = 3.37 \times 10^{-27} \quad j_c = -1.53 \quad r^2 = 0.440$

Figure 37. Kinetic correlation for APU clusters and agglomerates

THIS PAGE

WAS INTENTIONALLY

LEFT BLANK

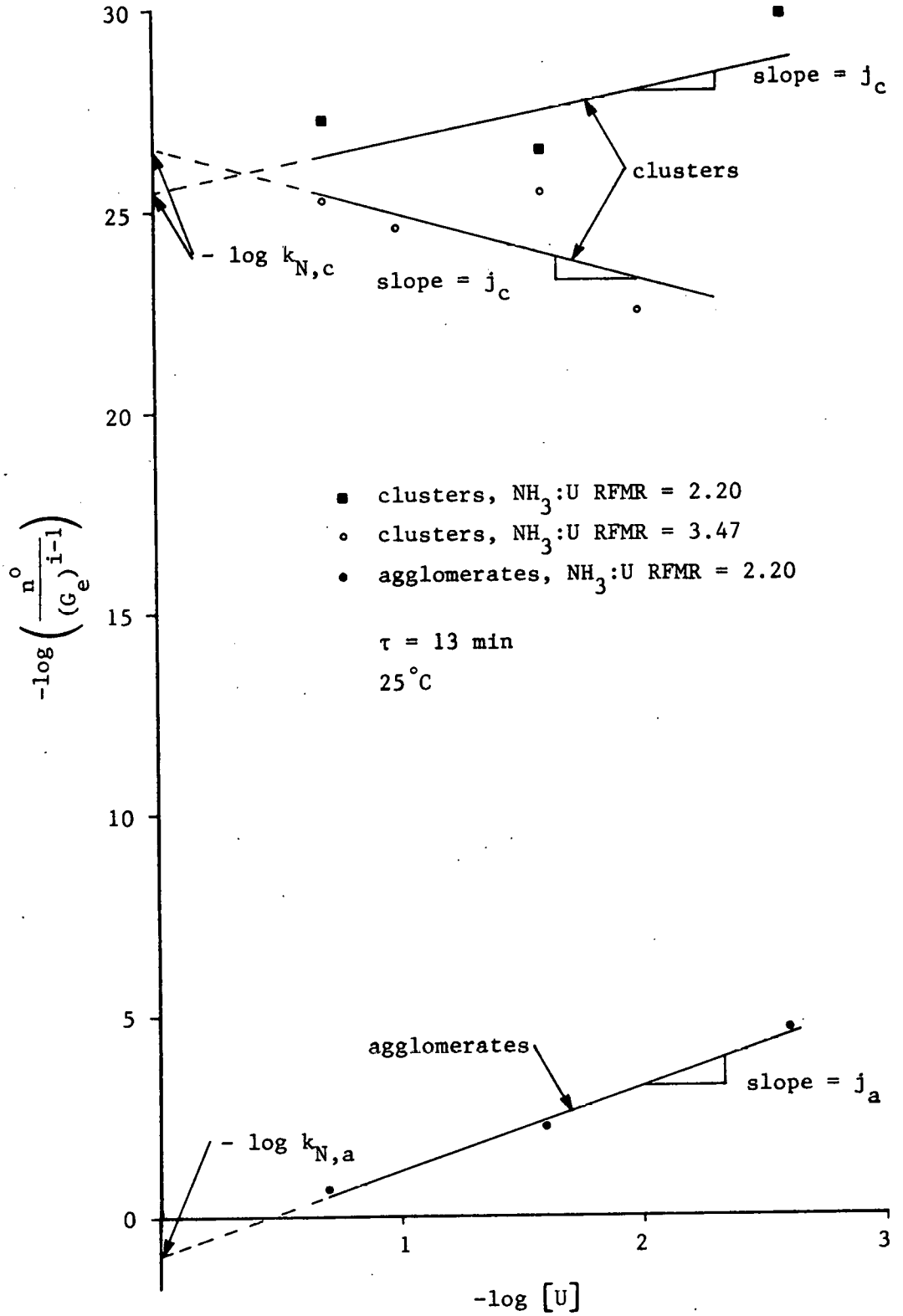
30
25
20
15
10
5
0
1
2
3
slope = j_c
clusters
- log $k_{N,c}$
slope = j_c
clusters, NH_3:U RFMR = 2.20
clusters, NH_3:U RFMR = 3.47
agglomerates, NH_3:U RFMR = 2.20
τ = 13 min
25°C
agglomerates
slope = j_a
- log $k_{N,a}$
$-\log\left(\frac{n^\circ}{(G_e)^{i-1}}\right)$
-log [U]

NH_3:U RFMR = 2.20 $k_{N,c} = 4.60 \times 10^{-26}$ $j_c = 1.44$ $r^2 = 0.591$

NH_3:U RFMR = 2.20 $k_{N,a} = 9.19$ $j_a = 2.08$ $r^2 = 0.976$

with r^2 being the regression coefficient again.

One unusual and unexpected occurrence in this work was that for a uranium concentration of 0.0025 molar, precipitation did not take place when the NH_3:U RFMR was 3.47. In contrast to this, precipitation did occur for this uranium concentration when the NH_3:U RFMR was 2.2. Presently this can not be explained without having more information on the composition of APU and on the reaction kinetics that are involved.

Effects of Other Variables

The type of model describing the nucleation rates can also be developed for the coagulation constants, once the kinetic data for the APU crystallites becomes available. Ideally, one would also want to investigate the effects of temperature, agitation, ultrasonics, surfactants, and the use of ammonia rather than ammonium hydroxide. Although these variables were not included in this work, one can infer what their effects might be. Temperatures can be expected to affect solubilities and hence, supersaturation. This means that it should be possible to control the APU crystallite size by controlling the temperature. Agitation would not be expected to have much effect except at very high rates where agglomerate break up would occur. The use of surfactants can be expected to either increase or decrease the rate of coagulation, depending upon the characteristics of the one being used. Ultrasonics has been reported (81) to increase the coagulation rate by

increasing the collision rate between particles. The use of ammonia rather than ammonium hydroxide has been reported (25) to yield very small, unagglomerated APU crystallites. This is probably the result of dilution difficulties, with many local regions having a high NH_3:U RFMR near the point of gas entry.

Significance of Results

The results of this work have shown that the continuous APU precipitation process can be operated in such a manner that it is possible to control the number ratio of clusters to agglomerates, their particle size distributions, and their firmness or cohesiveness. This indicates that it should be possible to produce a precipitate whose physical characteristics are such that ball-milling, use of pore formers, and the blending of powders of different structures and sizes can be eliminated in the nuclear fuel fabrication process. This would significantly reduce the cost of the fabrication process through the increased efficiency of a continuous process over that of a batch process, through increased product uniformity, and through reduced inventories of fuel material.

SUMMARY AND CONCLUSIONS

A mathematical model describing the kinetics of continuous precipitation has been developed. This model accounts for crystal nucleation, crystal growth, primary coagulation, and secondary coagulation, with the coagulation processes being represented with average nucleation rates and effective growth rates. Development of the model has followed from the assumptions that; (1) the particles can be represented by some characteristic dimension, (2) the growth rates of the crystals, primary coagulated particles, and secondary coagulated particles are all size-independent, and (3) the coagulation constants can be described through functions of the process variables (temperature, feed concentrations, reacting feed mole ratios, etc.). The kinetic model includes emperical relationships for the nucleation rates such that the population density distributions, average particle sizes, dominant particle sizes, and suspension density fractions of the crystallites, primary agglomerates, and secondary agglomerates leaving the continuous precipitator can be determined.

This kinetic model has been successfully applied to the continuous precipitation of ammonium polyuranate, which has been found to consist of three types of particles; (1) elementary crystals, (2) clusters or primary coagulated particles, and (3) agglomerates or secondary coagulated particles. The ammonium polyuranate crystallites have been shown to be thin, hexagonal platelets, the size of which depends upon the precipitation conditions, but were submicron in all cases studied. The clusters had an upper size limit of about 7 μm in diameter and

contained numerous small voids (<0.3 μm) due to the packing of the crystallites. The agglomerates, on the other hand, had an upper size limit of about 40 μm in diameter and contained large voids (~1 μm) which resulted from loose packing of both clusters and crystallites.

The precipitation conditions have been shown to affect the nucleation rates, growth rates, and particle structures of the primary and secondary coagulated particles. The kinetic parameters governing the particle size and structure of the precipitate have been shown to be correlated with the ammonium to uranium reacting feed mole ratio (NH_3:U RFMR) rather than the precipitation pH. This is contrary to the results previously published by others, where particle size, settling rates, and filtration rates were correlated with the pH of precipitation.

The effective growth rate of the agglomerates has been shown to be very sensitive to the NH_3:U RFMR, peaking at a value of 2.2, while that of the clusters has been shown to be relatively insensitive to the NH_3:U RFMR. As the NH_3:U RFMR was shifted away from a value of 2.2, the effective growth rates of the clusters and agglomerates decreased and their nucleation rates increased, causing the number of particles of each type to increase. The cohesiveness or bonding strength of both the clusters and agglomerates decreased as the NH_3:U RFMR was increased until, at a value greater than about 2.35, the particles were so loosely structured that they collapsed upon being filtered out of solution.

The effect of changes in the suspension density for specific NH_3:U RFMR's was investigated by varying the uranium feed concentration.

Generally, increased uranium concentrations resulted in increased growth rates of both clusters and agglomerates, except at high uranium concentrations when secondary coagulation becomes dominant, resulting in a slight decrease in the cluster growth rate. The most profound effect was the dependence of the agglomerate nucleation rate on the uranium concentration, while that of the clusters showed only a slight dependency. This was evident through a dramatic increase in the agglomerate nucleation rate, and hence total number of agglomerates, as the uranium concentration was increased.

The results of this work have shown that the particle size distribution and particle structure of the ammonium polyuranate precipitate can be controlled through proper regulation of the precipitation conditions. The ratio of clusters to agglomerates can be best controlled through the uranium concentration, and the cohesiveness or internal bonding strength of the particles can be controlled with the NH_3:U RFMR. These two conditions, in conjunction with the residence time, will determine the nucleation rates, growth rates, and size distributions of the particles leaving the continuous precipitator.

It has been inferred that with proper control of the physical characteristics of the APU precipitate, the use of pore formers, ball-milling, and powder blending can probably be eliminated from the fuel fabrication process. This would substantially reduce the cost of fuel fabrication and therefore decrease the cost of the overall nuclear fuel cycle.

RECOMMENDATIONS

Results from this work have indicated several areas which need further investigation. It is recommended that the following subjects be considered for future research programs, the first three of which have already been initiated:

1. Comparison of the particle growth rates calculated from the particle size distributions measured by the Coulter counter to those calculated from the particle size distributions found with the scanning electron microscope.
2. Characterization of the APU crystallite size distributions and morphology with respect to precipitation conditions by using the scanning electron microscope. This kinetic data could then be combined with that of the primary and secondary coagulation to complete the APU precipitation model.
3. Simulation of the continuous MSMPR precipitation process with a computer to investigate control methods which could be used to produce particles of a given structure and size.
4. Examination of the effects of temperature, ultrasonics, and surfactants on the APU precipitation kinetics and particle structures.
5. Determination of the crystal structure and composition of APU obtained from different NH_3:U RFMR's.
6. Characterization of the effects of calcination conditions on the particle size distribution and structure of the APU particles when calcining to UO_3 and U_3O_8.

7. Characterization of the effects of reduction conditions on the particle size distribution and structure of the UO_3 and U_3O_8 particles when reducing to UO_2.
8. Correlation of the UO_2 particle structure and size distribution to the microstructure of the sintered UO_2 pellet.
9. Application of the continuous MSMPR precipitation model to other precipitation reactions where control of the precipitate's size and structure is necessary.

BIBLIOGRAPHY

1. Aas, Steinar. 1972. Mechanical interaction between fuel and cladding. Nuclear Engineering and Design 21:237.

2. Adwick, A. G., and R. J. Warmer. 1966. The influence of particle size distributions on the sintering of ceramic powders. Pages 329-343 in the Proceedings of the Particle Size Analysis Conference. The Society for Analytical Chemistry, London, England.

3. Ainscough, J. B. 1961. The characteristics and sintering behavior of uranium dioxide prepared by a homogeneous precipitation route. J. Appl. Chem. 11:365.

4. Ainscough, J. B., and B. W. Oldfield. 1962. Effect of ammonium diuranate precipitation and conditions on the characteristics and sintering behavior of uranium dioxide. J. Appl. Chem. 12:418.

5. Alfredson, P. G. 1972. Pilot plant development of processes for the production of nuclear grade uranium dioxide. AAEC/E245.

6. Alfredson, P. G., and J. Janov. 1971. Investigation of batch-tray calcination-reduction of ammonium diuranate to uranium dioxide. AAEC/TM599.

7. Anderson, J. S., E. A. Harper, S. Moorbeth, and L. E. J. Roberts. 1957. The properties and microstructure of uranium dioxide: Their dependence upon the mode of preparation. AERE C/R-886.

8. Bancroft, A. R., and L. C. Watson. 1958. Preparation of uranium dioxide for use in ceramic fuels, part III ammonium diuranate reduction studies. CRCE-716, Part III.

9. Bane, R. W. 1949. The effect of sodium ion on the precipitation of uranium with ammonium hydroxide. Pages 47-49 in Summary Report. ANL-4232.

10. Barr, M. J. 1970. Activation of some UO_2 powders by milling and oxidation-reduction. WHAN-FR-8.

11. Barr, M. J., J. L. Jaech, and A. G. Anderson. 1970. Investigation of mixed oxide $(U_{0.75}Pu_{0.25})O_2$ processing using a nine variable fractional factorial experiment. BNWL-1445.

12. Barr, M. J., M. W. Urie, J. L. Daniel, and S. J. Mayhan. 1970. Characterization of some UO_2 and Pu_2 powders. BNWL-1441.

13. Bel, A., and Y. Carteret. 1958. Contribution to the study of sintering of uranium dioxide. Proceedings of the Second United Nations International Conference on the Peaceful Uses of Atomic Energy 6:612-619. United Nations, Geneva.

14. Belle, J. 1950. Properties of uranium dioxide. Proceedings of the Second United Nations International Conference on the Peaceful Uses of Atomic Energy 6:569-589. United Nations, Geneva.

15. Belle, J., and B. Lustman. 1957. Properties of uranium dioxide. Bettis Plant, Pittsburgh, Pennsylvania. WAPD-184.

16. Boltax, A. 1962. Behavior of fissionable material under irradiation. Chapter 9 in A. R. Kaufmann, ed. Nuclear Reactor Fuel Elements, Metallurgy and Fabrication. Interscience Publishers, New York-London.

17. Bourns, W. T., and L. C. Watson. 1958. Preparation of uranium dioxide for use in ceramic fuels, part I, batch precipitation of ammonium diuranate. CRCE-716, Part I.

18. Bourns, W. T., and L. C. Watson. 1961. Preparation of uranium dioxide for use in ceramic fuels, part V, the enriched uranium dioxide plant. AECL-1312.

19. Brandberg, S. G. 1973. The conversion of uranium hexafluoride to uranium dioxide. Nuclear Technology 18(2):177-184.

20. Bupp, L. P., and E. A. Evans. 1969. Oxide fuel trends. Pages 16-24 in O. L. Kruger, ed. Ceramic Nuclear Fuels. American Ceramic Society, Inc. Columbus, Ohio.

21. Burke, J. E. 1968. Sintering and microstructure control. General Electric, Metallurgy and Ceramics Laboratory (Schenectady, New York). Report No. 68-C-368.

22. Chalder, G. H., N. F. H. Bright, D. L. Paterson, and L. C. Watson. 1958. The fabrication and properties of uranium dioxide fuel. Proceedings of the Second United Nations International Conference on the Peaceful Uses of Atomic Energy 6:590-604. United Nations, Geneva.

23. Christensen, J. A. 1970. Structure evolution in an oxide fuel pin. WHAN-SA-79.

24. Chubb, W., A. C. Hott, B. M. Argall, and G. R. Kilp. 1975. The influence of fuel microstructure on in-pile densification. Nuclear Technology 26:486.

25. Clayton, J. C., and S. Aronson. 1961. Some preparative methods and physical characteristics of uranium dioxide powders. J. Chemical and Engineering Data 6:43-51.

26. Cordfunke, E. H. P. 1962. On the uranates of ammonium-I, the ternary system NH_3-UO_3-H_2O). J. Inorg. Nucl. Chem. 24:303.

27. Cordfunke, E. H. P. 1969. The chemistry of uranium. Elsevier Publishing Company, New York.

28. Cordfunke, E. H. P. 1970. Composition and structure of ammonium uranates. J. Inorg. Nucl. Chem. 32:3129.

29. Cordfunke, E. H. P., and A. A. VanDerGiessen. 1963. Pseudomorphic decomposition of uranium peroxide into UO_3. J. Inorg. Nucl. Chem. 25:553.

30. Cordfunke, E. H. P., and A. A. VanDerGiessen. 1965. Texture and reactivity of uranium oxides. Pages 456-466 in the Proceedings of the Fifth International Symposium on the Reactivity of Solids. Elsevier Publishing Company, London.

31. Cordfunke, E. H. P., and A. A. VanDerGiessen. 1967. Particle properties and sintering behavior of uranium dioxide. J. Nucl. Mat. 24:141.

32. Culbert, W. H. 1973. Densification of reactor fuels. Nuclear Safety 14(4):356.

33. Daubert, D. B. 1970. Forming fuel Westinghouse way. Ceramic Age 86(12):20-23.

34. DeHalas, D. R., and G. R. Horn. 1963. Evolution of uranium dioxide structure during irradiation of fuel rods. J. Nucl. Mat. 8(2):207.

35. Debets, P. C., and B. O. Loopstra. 1963. On the uranates of ammonia-II, X-ray investigation of the compounds in the system NH_3-UO_3-H_2). J. Inorg. Nucl. Chem. 25:945.

36. Delichatsios, M. A., and R. F. Probstein. 1975. Coagulation in turbulent flow: theory and experiment. J. Colloid Sci. 51:394-405.

37. Dembinski, W., A. Deptula, and S. Rykowski. 1966. The effect of precipitation conditions of ammonium polyuranate on sinterability of uranium dioxide. Nukleonika 11(7-8):93.

38. Deptula, A. 1962. A study of composition of ammonium uranates. Nukleonika 7:265-275.

39. Deptula, A., J. Rebandel, and W. Drozda. 1975. Studies on ammonium polyuranates obtained from UF_6. Nucleonika 20(11):1009.

40. Doi, H., and T. Ito. 1964. Significance of physical state of starting precipitate in growth of uranium dioxide particles. J. Nucl. Mat. 11(1):94-106.

41. Duncan, R. N., N. Fuhrman, and J. C. LaVake. 1975. Dimensional stability of water reactor fuel. Pages 2-55 to 2-73 in the Proceedings of Joint Topical Meeting on Commercial Nuclear Fuel Technology Today, April 28-30, 1975. ANS and CNA, Toronto, Canada.

42. Evans, E. A., and W. F. Sheely. 1972. Ceramic fuels. Chapter 9 in D. M. Elliott and L. E. Weaver, eds. Education and Research in the Nuclear Fuel Cycle. University of Oklahoma Press, Norman Oklahoma.

43. Ewing, R. A., S. J. Jr. Kiehl, and A. E. Bearse. 1956. Investigation of ammonium uranates. BMI-1115.

44. Fair, G. M., and R. S. Gemmell. 1963. A mathematical model of coagulation. J. Colloid Sci. 19:360-372.

45. Findlay, J. R. 1974. The composition and chemical state of irradiated oxide reactor fuel material. Pages 31-39 in the Proceedings of a Panel on the Behavior and Chemical State of Irradiated Ceramic Fuels. The International Atomic Energy Agency, Vienna.

46. Findlay, J. R. 1974. The migration of fission products through reactor fuel materials. Pages 211-220 in the Proceedings of a Panel on the Behavior and Chemical State of Irradiated Ceramic Fuels. The International Atomic Energy Agency, Vienna.

47. Freshley, M. D. 1972. A comparison of pellet and vipac nuclear fuels. Nuclear Engineering and Design 21:264.

48. Freshley, M. D., and T. B. Burley. 1969. Vibrationally compacted ceramic fuels. BNWL-SA-2412.

49. Freshley, M. D., P. E. Hart, J. L. Daniel, D. W. Brite, and T. D. Chikalla. 1975. The effect of pellet characteristics and irradiation conditions on UO_2 fuel densification. Pages 2-106 to 2-126 in the Proceedings of Joint Topical Meeting on Commerical Nuclear Fuel Technology Today, April 28-30, 1975. ANS and CNA, Toronto, Canada.

50. Frost, B. R. T. 1969. Studies of irradiation effects in ceramic fuels at Harwell. Pages 225-243 in O. L. Kruger, ed. Ceramic Nuclear Fuels. American Ceramic Society, Inc., Columbus, Ohio.

51. Galkin, H. P., B. N. Sudarikov, and others. 1966. Technology of uranium. AEC-TR-6638.

52. Gardner, N. R. 1962. Uranium dioxide and other ceramic fuels. Chapter 6 in A. R. Kaufmann, ed. Nuclear Reactor Fuel Elements. Interscience Publishers, New York.

53. Garner, E. V. 1961. X-ray diffraction studies on compounds related to uranium trioxide dihydrate. J. Inorg. Nucl. Chem. 21:380.

54. Garside, J., and S. J. Jančić. 1976. Prediction and measurement of crystal size distributions for size-dependent growth. Unpublished paper presented at the 69th AIChE Annual Meeting, Chicago, Illinois.

55. Gentile, P. S., and T. J. Collopy. 1956. Ammonia precipitation and filtration studies from uranyl nitrate solution. NLCO-645.

56. Goodarz-Nia, I. 1975. Floc simulation. Effect of particle size distribution. J. Colloid Sci. 52:29-40.

57. Hermans, M. E. A. 1958. The preparation of uranium dioxide fuel for a suspension reactor. Proceedings of the Second United Nations International Conference on the Peaceful Uses of Atomic Energy 6:39-44. United Nations, Geneva.

58. Hermans, M. E. A., and T. Markestein. 1963. Ammonium uranates and UO_3-hydrates-ammoniates. J. Inorg. Nucl. Chem. 25:461.

59. Hidy, G. M. 1965. On the theory of the coagulation of noninteracting particles in Brownian motion. J. Colloid Sci. 20:123-144.

60. Huang, Chao-Ming, M. Kerker, and E. Matijević. 1970. The effect of Brownian coagulation, gradient coagulation, turbulent coagulation, and wall losses upon the particle size distribution for an aerosol. J. Colloid Sci. 33:529-538.

61. Huntington, C. W., M. G. Mendel, K. J. Notz, and G. G. Briggs. 1958. Thermal decomposition, reduction, and hydrofluorination of ADU. Pages 61-68 in J. W. Simmons. Summary Technical Report. NLCO-775.

62. Janov, J., P. G. Alfredson, and V. K. Vilkaitis. 1971. The influence of precipitation conditions on the properties of ammonium diuranate and uranium dioxide powders. AAEC/E220.

63. Janov, J., P. G. Alfredson, and V. K. Vilkaitis. 1975. Pilot plant development of processes for the production of ammonium diuranate. AAEC/E333.

64. Kiessling, R., and U. Runfors. 1957. Sintering of uranium dioxide. Pages 402-413 in the Proceedings of the Symposium Technique sur les Elements de Combustible, CEA, Paris. A. B. Atomenergi, Stockholm, Sweden.

65. Kleykamp, H. 1974. Formation of phases and distribution of fission products in an oxide fuel. Pages 157-166 in the Proceedings of a Panel on the Behavior and Chemical State of Irradiated Ceramic Fuels. The International Atomic Energy Agency, Vienna.

66. Klima, J., M. Podéšť, and V. Vinš. 1974. Contribution to the studies of the fission gases released from irradiated uranium oxide pellets. Pages 221-224 in the Proceedings of a Panel on the Behavior and Chemical States of Irradiated Ceramic Fuels. The International Atomic Energy Agency, Vienna.

67. Kramer, F. W. 1975. PWR fuel performance - the Westinghouse view. Pages 1-50 to 1-65 in the Proceedings of Joint Topical Meeting on Commerical Nuclear Fuel Technology Today, April 28-30, 1975. ANS and CNA, Toronto, Canada.

68. Leitnaker, J. M., M. L. Smith, and C. M. Fitzpatrick. 1972. Conversion of uranium nitrate to ceramic-grade oxide for the light water breeder reactor: process development. Metals and Ceramics Division. ORNL-4755.

69. Lister, B. A. J., and G. M. Gillies. 1956. The conversion of uranyl nitrate to uranium dioxide and to uranium tetrafluoride. Process Chemistry 1:19-35.

70. Loudin, D. J. 1958. Semi-works ADU precipitate. Pages 51-61 in J. W. Simmons, ed. Summary Technical Report. NLCO-775.

71. Loudin, D. J. 1959. Engineering evaluation of semi-works ADU production. NLCO-786.

72. Loudin, D. J., and T. A. Hehemann. 1958. Pilot plant studies of precipitation. Pages 50-51 in J. W. Simmons, ed. Summary Technical Report. NLCO-775.

73. Lyons, M. F., R. F. Boyle, J. H. Davies, V. E. Hazel, and T. C. Rowland. 1972. UO_2 properties affecting performance. Nuclear Engineering and Design 21:167.

74. Markworth, Alan J. 1972. Size-distribution effects in the growth of precipitates from solution. J. Colloid Sci. 38:636-638.

75. Marlowe, M. O. 1973. In-reactor densification behavior of UO_2. NEDO-12440.

76. Matthews, B. A., and C. T. Rhodes. 1970. Some observations on the use of the Coulter counter model B in coagulations studies. J. Colloid Sci. 23:339-348.

77. Mohr, A. W. 1970. Pressing problems not unique. Ceramic Age 86(12):24.

78. Murray, P., and J. Williams. 1958. Ceramic and cermet fuels. Proceedings of the Second United Nations International Conference on the Peaceful Uses of Atomic Energy 6:538-550. United Nations, Geneva.

79. Nielsen, A. E. 1964. Kinetics of precipitation. The Macmillan Company, New York.

80. Notz, K. J., M. G. Mendel, C. W. Huntington, and T. J. Collopy. 1960. On the structure and thermal decomposition of "ammonium diuranate". TID-6228.

81. Orr, C., Jr. 1966. Particulate technology. The Macmillan Company, New York.

82. Palei, P. N. 1970. Analytical chemistry of uranium. Pages 24-27. Ann Arbor-Humphrey Science Publishers, Ann Arbor, London.

83. Pickman, D. O. 1972. Design of fuel elements. Nuclear Engineering and Design 21:303.

84. Proebstle, R. A., J. H. Davies, T. C. Rowland, D. R. Rutkin, and J. S. Armijo. 1975. The mechanism of defection of zircaloy-clad fuel rods by internal hydriding. Pages 2-15 to 2-34 in the Proceedings of Joint Topical Meeting on Commerical Nuclear Fuel Technology Today, April 28-30, 1975. ANS and CNA, Toronto, Canada.

85. Ramabhadran, T. E., T. W. Peterson, and J. H. Seinfeld. 1976. Dynamics of aerosol coagulation and condensation. J. AIChE 22:840-851.

86. Ramm, E. J., and S. T. Quaass. 1968. Preparation and evaluation of an ADU-derived ceramic grade UO_2 powder. Australian Atomic Energy Commission Research Establishment, Lucas Heights, Australia.

87. Randolph, A. D., and M. A. Larson. 1971. Theory of particulate processes. Academic Press, New York. 251 pp.

88. Reinhart, G. M. 1958. Continuous ammonia precipitation of uranium from pure uranyl nitrate solutions. NLCO-757.

89. Reinhart, G. M. 1958. Continuous precipitation of "ammonium diuranate" at low pH. Pages 49-51 in J. W. Simmons, ed. Summary Technical Report. NLCO-725.

90. Reinhart, G. M. 1958. ADU "ammonium diuranate" process development. Pages 49-50 in J. W. Simmons, ed. Summary Technical Report. NLCO-775.

91. Reinhart, G. M., C. W. Huntington. 1958. Pilot plant precipitation of "ammonium diuranate". Pages 63-67 in J. W. Simmons, ed. Summary Technical Report. NLCO-750.

92. Reinhart, G. M., and D. J. Loudin. 1959. The correlation of "ammonium diuranate" properties with precipitation variables. Pages 61-65 in J. W. Simmons, ed. Summary Technical Report. NLCO-800.

93. Reinhart, G. M., J. T. Collopy, and H. Brech. 1956. Summary Technical Report, p. 121. NLCO-650.

94. Robertson, J. A. L. 1975. Nuclear fuel failures, their causes and remedies. Pages 2-2 to 2-14 in the Proceedings of Joint Topical Meeting on Commercial Nuclear Fuel Technology Today, April 28-30, 1975. ANS and CNA, Toronto, Canada.

95. Runfors, Ulf, Nile Schonberg, and Roland Kiessling. 1958. The sintering of uranium dioxide. Proceedings of the Second United Nations International Conference on the Peaceful Uses of Atomic Energy 6:605-611. United Nations, Geneva.

96. Runnalls, O. J. C. 1959. Uranium dioxide fuel elements. Pages 228-266 in H. H. Hausner, ed. Nuclear Fuel Elements. Reinhold Publishing Corporation, New York.

97. Scott, R., and J. Williams. 1957. The warm-pressing of uranium dioxide and uranium dioxide-metal mixtures. AERE M/R-2396.

98. Stehle, H., and H. Assmann. 1976. In-reactor UO_2 densification. J. Nucl. Mat. 61:326.

99. Stehle, H., H. Assmann, and F. Wunderlich. 1975. Uranium dioxide properties for LWR fuel rods. Nuclear Engineering and Design 33:230.

100. Stevenson, D. G. 1964. Theoretical aspects of the design and operation of continuous chemical precipitators. Trans. Instn. Chemical Engrs. 42:T316-T342.

101. Stoll, W. 1975. Experience in operating a Pu-Fabrication facility. Pages 4-24 to 4-44 in the Proceedings of Joint Topical Meeting on Commercial Nuclear Fuel Technology Today, April 28-30, 1975. ANS and CNA, Toronto, Canada.

102. Stuart, W. T., and T. L. Whateley. 1969. Composition and structure of ammonium uranates. J. Inorg. Nucl. Chem. 31:1639.

103. Sutton, J. 1949. The hydrolysis of the uranyl ion, Part I. J. Chem. Soc., Suppl. Iss.:275-286.

104. Ukaji, R. 1959. On the reactivity of uranouranic oxide (I), the thermal decomposition of uranyl nitrate (UNH), ammonium diuranate (ADU), and uranium peroxide. AEC-TR-4939.

105. Walton, A. G. 1967. The formation and properties of precipitates. Interscience Publishers, New York.

106. Washburn, T. N. 1970. Porous UO_2 bodies produced by reduction of U_3O_8. Nuclear Applications and Technology 8:23.

107. Weber, C. E. 1972. Status and problems of fast reactor fuels. Chapter 3 in D. M. Elliott and L. E. Weaver, eds. Education and Research in the Nuclear Fuel Cycle. University of Oklahoma Press, Norman, Oklahoma.

108. Williamson, H. E., and R. A. Proebstle. 1975. Results with BWR fuel improvements. Pages 1-38 to 1-48 in the Proceedings of Joint Topical Meeting on Commercial Nuclear Fuel Technology Today, April 28-30, 1975. ANS and CNA, Toronto, Canada.

109. Woolfrey, J. L. 1968. The preparation and calcination of ammonium uranates - a literature survey. AAEC/TM-476.

110. Woolfrey, J. L. 1972. Effect of green density on the initial-stage sintering kinetics of UO_2. J. American Ceramic Society 55:383-389.

111. Woolfrey, J. L. 1974. Surface area changes during the calcination of ammonium uranate. AAEC/E329.

112. Woolfrey, J. L. 1976. Surface area changes during the thermal decomposition of ammonium uranate. J. Inorg. Nucl. Chem. 38:347-348.

113. Yatabe, E., and L. C. Watson. 1958. Preparation of UO_2 for use in ceramic fuels, part II, continuous precipitation of ammonium diuranate. CRCE-716, Part II.

ACKNOWLEDGEMENTS

The author wishes to express his gratitude to Dr. L. E. Burkhart for his helpful discussions, assistance, and patience in the course of this work.

Special appreciation is expressed to James Herriott for his many hours of help setting up equipment for the precipitation process, and especially his assistance during the operation of the process. Appreciation is also expressed to Timothy Oolman for his SEM analysis of the precipitate and to Harvey Jensen for his help in obtaining and setting up some of the equipment for the process.

The author is also especially grateful to his wife, Jean, for her understanding, patience and encouragement during the course of this work, and for her help in the preparation of this manuscript.